COMPOSITIONAL SENSITIVITY IN ADDITIVELY MANUFACTURED ALUMINUM ALLOY 2139

A thesis submitted in partial fulfilment of the

Requirements for the Degree of

Doctor of Philosophy in Mechanical Engineering

in the University of Canterbury

by Craig A. Brice

University of Canterbury

2018

TABLE OF CONTENTS

LIST OF FIGURES

LIST OF TABLES

1.0 ACKNOWLEDGEMENTS

First I would like to thank my advisory team at the University of Canterbury, Professors Milo Kral and Catherine Bishop. My unique circumstances made the logistics of this project extra challenging and I thank them both for their accommodation. This has been a tremendous learning experience for me and I appreciate their guidance and instruction. I would also like to thank Mike Flaws in the Mechanical Engineering department for his help with electron microscopy. Finally, I acknowledge the financial support of the Mechanical Engineering Department at the University of Canterbury.

At NASA Langley Research Center, Hampton, Virginia, USA, I would like to thank John "Andy" Newman, Wes Tayon, Jim Baughman, Clay Claytor, and Pete Messick. They were instrumental in helping to fabricate experimental alloy castings and prepare them for use in the experiment. They also allowed the use of their transmission electron microscope and provided analysis support for the differential scanning calorimetry experiments. This collaboration was made possible through a Lockheed Martin–NASA Space Act Agreement, SAA1-1376.

At Lockheed Martin I would like to thank Wes Martin and Mike Fitzpatrick for their help in conducting the deposition experiment. I would like to thank Terri Peters for her assistance with the optical microscopy and hardness measurements and Jane Bonvallet for her help with the scanning electron microscopy. I would like to thank Scott Cochran for his help with heat treatment. I also acknowledge the financial support of Lockheed Martin in conducting the research experiments.

At the Australian Nuclear Science and Technology Organisation I would like to thank Anna Sokolova, the instrument scientist on BILBY. She was very helpful and very patient as I knew virtually nothing about small-angle neutron scattering when I showed up for my

experiment. I acknowledge the support of the Australian Centre for Neutron Scattering, Australian Nuclear Science and Technology Organisation, in providing the neutron research facilities used in this work.

Last but not least, I would like to thank my family; my wife Amy and my children Carson and Anna. Their support during this project has been instrumental in getting me to the end. I could not have done it without their encouragement and support.

2.0 ABSTRACT

One of the biggest challenges when utilizing additive manufacturing (AM) for the fabrication of aluminium alloy structures is achieving wrought-equivalent properties. Wrought alloys that are precipitation strengthened typically require some form of mechanical processing (e.g., rolling or stretching) to achieve peak strength. The ability to produce net- or near-net-shape structures is a key benefit to AM; mechanical post-processing is therefore generally undesirable. There are few alloys that can be heat treated to wrought-equivalent strength without the need for a mechanical processing step. Aluminium 2139, an Al-Cu-Mn-Mg-Ag composition, is an alloy that can be strengthened through heat treatment alone, making it ideally suited for use in AM processes. The challenge with this alloy, however, is the high volatility of Mg compared with Al and the other alloying constituents. This volatility is particularly important in AM, in which preferential vaporization from the molten pool is known to occur. Although there is only a small amount of Mg in the alloy, its presence is critical for achieving peak strength in the heat-treated condition. Small variations in Mg concentration due to preferential vaporization can reduce the strength of the deposited alloy. Because AM is an incremental process, there is also the potential for chemical and property gradients within a single part caused by changes in the processing conditions as the AM build progresses. This project explores the relationship between process settings and vaporization loss in additively manufactured aluminium 2139. A correlation is developed between Mg concentration and precipitate size and distribution. These relationships are linked to vaporization theory, and a predictive model is developed that can predict vaporization loss as a function of molten pool temperature. The results provide a control strategy that can be used to ensure chemical consistency in additively manufactured aluminium alloy 2139.

3.0 LIST OF ACRONYMS

AM..... additive manufacturing

PBF.....powder bed fusion

DED.....directed energy deposition

EBDED..... electron beam directed energy deposition

WAAM..... wire arc additive manufacturing

CNC.....computer numerical control

ELI..... extra low interstitial

CT..... computed tomography

RSP..... rapid solidification process(ing)

CP ..... commercially pure

SSSS .....supersaturated solid solution

SFE .....stacking fault energy

APB .....anti-phase boundary

GP..... Guinier Preston

GPB .....Guinier Preston Bagaryatski

PALS .....positron annihilation lifetime spectroscopy

CBD..... coincidence Doppler broadening

1DAP .....one-dimensional atom probe

3DAP..... three-dimensional atom probe

POSAP.....position-sensitive atom probe

TEM.....transmission electron microscopy

VHN .....Vickers hardness number

NASA .....National Aeronautics and Space Administration

SDAS.....secondary dendrite arm spacing

SANS..... small angle neutron scattering

DSC .....differential scanning calorimetry

ASNTO..... Australian Nuclear Science and Technology Organisation

4.0 INTRODUCTION

4.1 Problem Statement

Additive manufacturing (AM) is an emerging technology with great potential to revolutionize the fabrication of complex metallic objects.[1] AM encompasses multiple process variants that all utilize a feedstock material along with an energy source driven by a multi-axis motion control system to create fully dense three-dimensional objects directly from a computer file. The majority of these processes are fusion-based and use a concentrated heat source to generate a local molten pool at the point where the feedstock is added. Additionally, a controlled atmosphere environment is often needed for protecting reactive alloys from contamination. The atmosphere can be inert (consisting of argon gas, for example) at a variety of pressures, or it can be a vacuum. A consequence of these processing conditions is that preferential vaporization from the molten pool can occur when the alloying constituents vary widely in vapour pressure.[2] Unfortunately, many existing alloy compositions contain solute additions that have significantly higher vapour pressures than the main alloy constituent at the alloy melting point (e.g., aluminium in titanium alloys and magnesium in aluminium alloys). Compounding this issue of preferential vaporization is the transient nature of the process conditions during deposition. Because residual heat accumulates in the previously deposited layers, the size and temperature of the molten pool can increase if the input energy is not reduced as the AM process proceeds. Such increases can create a transient variation in vaporization loss from the beginning of the deposit to the end. These two factors, preferential vaporization and transient thermal conditions, lead to variations in chemistry within the deposit and result in inconsistent mechanical properties.

4.2 Aims and Objectives

This project seeks to understand the relationship between processing conditions and vaporization loss within an additively manufactured magnesium-bearing aluminium alloy. The main objectives of this research are to (1) develop a thorough understanding of how AM process settings affect vaporization rates in additively manufactured Mg-bearing aluminium alloys, (2) correlate the microstructure and property effects of varied Mg content, and (3) apply relevant vaporization models to help predict and control Mg loss during deposition. The methodology developed will be applicable to a wide range of AM processes and a wide range of alloys with highly volatile solutes such as Al-Li, Ti-Al, and Mn-bearing steels.

4.3 Methodology

Although there are many additive manufacturing methods available, this project will focus on electron beam directed energy deposition (EBDED). This AM technique is capable of fabricating large structures (> 1 m) at high deposition rates (> 7.5 kg/hr).[3] The EBDED process is conducted in a vacuum, which is necessary to prevent attenuation of the electron beam by gas molecules. The vacuum environment is advantageous for limiting contamination in the deposited material because there is no gas that can react or become entrapped in the molten pool. The drawback of the vacuum environment is that it greatly amplifies the vaporization loss from the molten pool, which can lead to very large compositional changes in a deposited part.[4]

The alloy chosen for this project is aluminium alloy 2139, an Al-Cu-Mn-Mg-Ag alloy that is precipitation-hardenable to a high ultimate tensile strength (≈ 450 MPa) while maintaining adequate levels of ductility (6–10% elongation). Although only a small amount of magnesium is present (0.5 wt% nominal), it plays a major role in the precipitation behaviour of the alloy.[5] The magnesium and the silver work together to alter the manner in which the precipitates form, enabling peak aged strength without the need for mechanical work prior to

aging. Without an adequate level of Mg, this preferential precipitation mechanism breaks down, resulting in a lower peak aged strength and undesirable properties.

At atmospheric pressure, Mg is very near its boiling point when contained inside a molten pool of aluminium, assuming the molten pool is at 1000°C. The situation is even worse in a vacuum, the EBDED operating environment. In a vacuum environment, the Mg boiling point is reduced below the molten pool temperature, which allows a significant amount of Mg in the alloy to vaporize from the molten pool. The relationship between the Mg content in the deposited alloy and the mechanical properties is currently unknown.

Alloy 2139 allows a wide range of Mg content, from 0.2 wt% to 0.8 wt%.[6] In a cast or wrought product, the Mg content is set by the Mg content of the original melt. This is usually the composition midpoint (0.5 wt%), and current foundry practice allows accurate and repeatable fabrication at this concentration level. Because AM is an incremental process—that is, only a small piece of a given part is molten at any given time—the composition can vary based on process conditions. The molten pool size and temperature can vary from the first layer to the last as local thermal conditions change. Without controlling for these transient thermal conditions, the Mg vaporization rate will also vary within a given part. This will lead to unacceptable property variation throughout the part as the precipitation strengthening mechanism changes with changing Mg content.

This project examines the effect of Mg content and local thermal conditions on the resultant microstructure and properties in EBDED aluminium alloy 2139. Three experimental lots of material (both wire and baseplate) were created over the Mg compositional range of the alloy. These three alloys were deposited at three different substrate temperatures. This matrix of conditions provides insight into how both the concentration of Mg and the local temperature affect Mg loss in the EBDED process.

A variety of analysis and characterization tools were used to quantify the effects of vaporization loss within the deposited alloy material. For this particular alloy, the Mg content dictates the size, distribution, and crystallographic habit plane of the precipitate phase.[7] Comparative measurement of precipitate character using electron microscopy and small-angle neutron scattering determined qualitative differences in the alloy microstructure. These measurements were combined with chemical measurement of the deposited bead using plasma emission spectroscopy. Relative quantitative measurements of precipitate volume fraction were made using differential scanning calorimetry. Finally, various mechanical testing methods, such as hardness and tensile testing, were used to correlate mechanical properties to the various microstructures.

Using the kinetic theory of gases, the results from the chemical analysis were used to predict molten pool temperatures. The Hertz–Knudsen equation, which calculates vapour flux from a condensed phase, was adapted to the additive manufacturing environment to correlate vapour flux with temperature.[8] The predicted temperatures were then correlated with the deposited microstructures. The results show that by measuring the temperature of the molten pool as the AM process progresses, the vapour flux can be reliably predicted at any given point. Knowing the Mg vapour flux allows prediction of the microstructure of the material at any location within the part. Knowing the microstructure allows the prediction of the mechanical properties. This process-microstructure-property relationship provides a useful means for process control and can ensure that the deposited material has acceptable chemical uniformity from start to finish.

4.4 Contribution

Ensuring consistency and repeatability in additively manufactured materials is critical to gaining wide acceptance of AM as a legitimate fabrication method for production hardware. This is particularly important for alloys like aluminium 2139 that are very sensitive to small

compositional changes in highly volatile solute additions. Local variations in chemistry and microstructure can create uncertainty in the overall performance of AM structures. This project make a significant contribution to the understanding of vaporization loss in AM alloys. It also provides a predictive tool for minimizing vaporization loss, which ensures chemical consistency throughout a deposited structure. The methodology for correlating compositional control with molten pool temperature will be applicable to a wide range of AM processes and alloys.

References

1. Frazier, W. E., Metal additive manufacturing: a review. *Journal of Materials Engineering and Performance* **2014,** *23* (6), 1917-1928.

2. Brice, C. A.; Rosenberger, B. T.; Sankaran, S. N.; Taminger, K. M.; Woods, B.; Nasserrafi, R. In *Chemistry control in electron beam deposited titanium alloys*, Materials Science Forum, Trans Tech Publ: 2009; pp 155-158.

3. Stecker, S.; Lachenberg, K.; Wang, H.; Salo, R. In *Advanced electron beam free form fabrication methods & technology*, American Welding Society Conference, Missoula, MT, Nov, 2006; pp 35-46.

4. Brice, C.; Shenoy, R.; Kral, M.; Buchannan, K., Precipitation behavior of aluminum alloy 2139 fabricated using additive manufacturing. *Materials Science and Engineering: A* **2015,** *648*, 9-14.

5. Muddle, B. C.; Polmear, I., The precipitate Ω phase in Al-Cu-Mg-Ag alloys. *Acta Metallurgica* **1989,** *37* (3), 777-789.

6. SAE, AMS 4468 Aluminum Alloy, Plate 5.0Cu - 0.4Mn - 0.5Mg - 0.4Ag (2139-T84) Soution Heat Treated, Cold Worked, and Artificially Aged.

7. Ringer, S.; Hono, K.; Polmear, I.; Sakurai, T., Nucleation of precipitates in aged Al Cu Mg (Ag) alloys with high Cu: Mg ratios. *Acta Materialia* **1996,** *44* (5), 1883-1898.

8. Safarian, J.; Engh, T. A., Vacuum evaporation of pure metals. *Metallurgical and Materials Transactions A* **2013,** *44* (2), 747-753.

5.0 METAL ADDITIVE MANUFACTURING

5.1 History and Background

Creating three-dimensional shapes out of metal in an additive manner can be traced back to shortly after the development of arc welding methods. One of the earliest advances was made by Isaac Harter of Babcock & Wilcox who patented a "method of forming structures wholly of fusion deposited weld metal" in 1942.[1] Many fusion welding methods use a filler material to reinforce the joint. By eliminating the joint and stacking filler-metal weld beads together, one can create a three-dimensional object directly from the welding process itself. While Harter's method was an interesting concept, it was limited by the handheld, manual nature of early welding equipment. The advent of computer numerical control (CNC) and robotics for automated manipulation made the process of stacking weld beads to create a shape rigorous and repeatable.

The first true application of additive manufacturing (AM) as we know it today was made by the United Technologies Corporation (UTC) in 1982 when they patented a "method of fabricating articles by sequential layer deposition."[2] Their process included (1) a feedstock material, either powder or wire; (2) a high-energy heat source such as arc, laser, or electron beam; and (3) a CNC motion control system. While this patent was focused mainly on cladding, it still encompassed almost all aspects of the metal additive manufacturing methods used today.[3] The UTC patent is the precursor to the family of AM technologies that have become known as directed energy deposition (DED) processes. These processes use a directed energy source to form a molten pool on a substrate (or previously deposited layer). A feedstock material is injected into the molten pool.[4-6] As the control system moves the energy source and the material feed mechanism, a bead of deposited material is left behind. Sequential beads and layers

arranged in an overlapping manner result in a three-dimensional part made fully from solidified deposited beads.

In the mid-1990s, a new type of metal additive manufacturing process emerged known as powder bed fusion (PBF).[7-8] In PBF, a laser or electron beam is used to selectively melt metal powder that is spread out in a thin, uniform layer within a confined chamber. After the energy source melts and fuses a layer of powder, the deposition platform within the chamber lowers a distance equal to the thickness of one layer. A mechanical rake then spreads another thin layer of powder over the previously melted layer. The process repeats until the part is complete, resulting in a three-dimensional object that is composed of a series of two-dimensional layers fused together.

Arc-based heat sources can also be used in AM processes.[9] With an arc-based heat source, the most commonly used feedstock material is wire, though powder can be used as well. The feedstock can be delivered independent of the heat source (e.g., gas tungsten arc process) or it can be delivered as a consumable electrode (e.g., gas metal arc process). Similar to the other methods, the arc torch is carried robotically or with a multi-axis gantry, providing highly accurate material placement. Arc-based methods do not require a chamber and can easily be adapted from conventional robotic welding systems, making them much lower in cost compared with DED and PBF. Figure 5.1 shows schematic representations of the various fusion-based metal AM processes. Figure 5.2 shows example parts made using both the electron beam directed energy deposition process and the laser powder bed fusion process.

Directed energy deposition, powder bed fusion, and arc-based AM processes each have unique and often complementary advantages and disadvantages. The DED and arc processes are scalable and can be used to produce very large structures (> 1 m).[10] PBF is often confined to small parts (< 0.25 m), though the chamber size of the machines used for this process has rapidly increased in the past few years. The component size advantage in the DED and arc

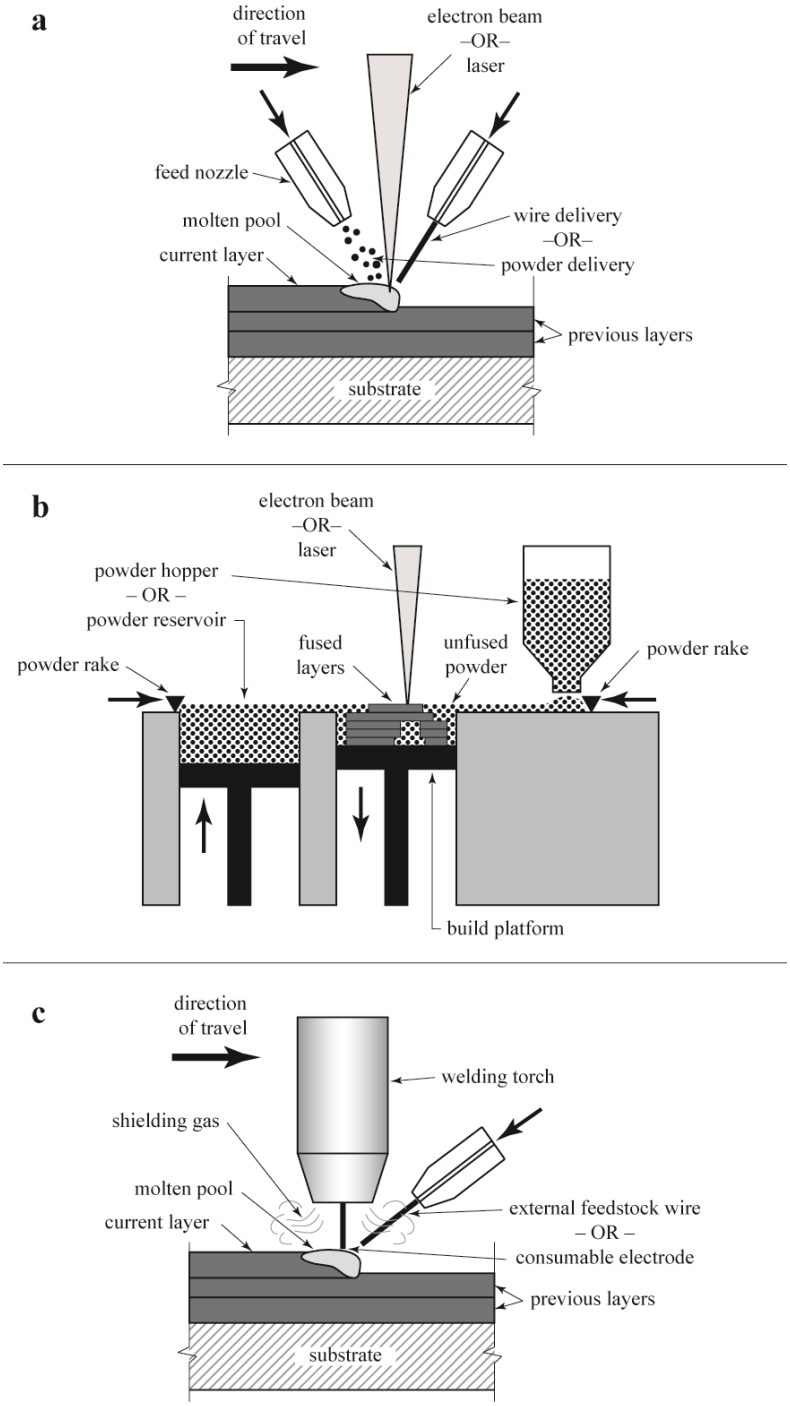

Figure 5.1: *Schematic of directed energy deposition process (a), powder bed fusion process (b), and wire arc process (c).*

approaches is usually offset by a lack of fidelity and resolution.[11-12] The very large additive parts made using DED or arc-based processes often require some level of machining or other post-processing to make them usable. For the PBF approach, very high resolution can be achieved in the as-deposited state (see Figure 5.2b). The fundamental trade-off between the two

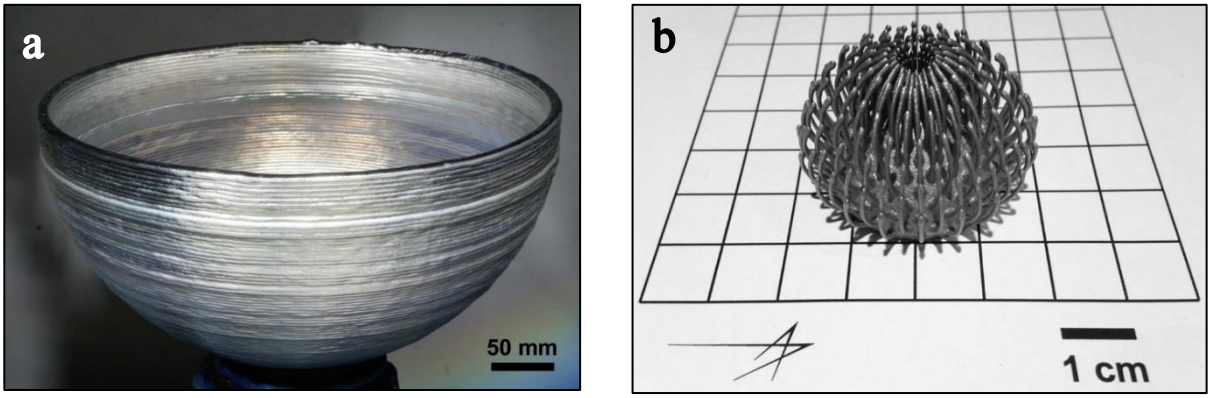

Figure 5.2: *Photographs of an additively manufactured part fabricated by electron beam directed energy deposition (a) and an additively manufactured part fabricated by laser powder bed fusion (b).*

process families is deposition rate versus resolution. For very large parts that require high deposition rates, low as-deposited part resolution is expected. Conversely, for very high resolution parts, the deposition rates are extremely low. The deposition rate used for the DED part in Figure 5.2a is greater than the rate used for the PBF part in Figure 5.2b by about a factor of fifty. This comparison in Figure 5.2 clearly shows the trade-off between deposition rate and part fidelity.

5.2 Applications

Applications of additive manufacturing have evolved over the years as the processes have matured and expanded into a wider range of materials and a wider range of process scales.[13] The focus in the early days of AM process development was on rapid prototyping, not on serial production. Only recently has AM become a truly credible approach for the fabrication of actual production hardware. Both performance and economic advantages have driven this shift.[14]

With the adoption of any new technology, the lowest-risk applications are often the first to market. For AM, producing tooling for other manufacturing processes is one of those low-risk applications.[15-16] Dies for injection moulding or die casting can be rapidly produced using AM. Additionally, the unique aspects of AM processes enable the fabrication of features that otherwise could not be incorporated, such as conformal cooling channels and embedded thermocouples for temperature measurement.[17] The advantages become more pronounced for

low production rates and for larger component sizes. This is an application area of AM that will continue to grow and expand as the technology for large-scale AM continues to mature.

One of the first structural applications of additive manufacturing was for spare parts in airframe structures.[10] AeroMet Corporation, established in 1997 as a subsidiary of MTS Systems Corporation, had a custom-built AM system that used a large, 19 kW CO_2 laser with powder feedstock to make large (> 1 m) structural parts using titanium and refractory alloys. Their first significant implementation was a wing pylon fitting replacement for the F-15 Strike Eagle. The original flight part was made from an aluminium alloy, but the AM replacement part was made with Ti-6Al-4V alloy. The much higher strength of the titanium AM part greatly increased the structural load margins, which helped reduce the overall implementation risk. A limited number of these replacement parts were fielded and put into service, resulting in a significant reduction in fabrication lead time and an increase in the expected component lifetime. Although they were successful, AeroMet eventually ceased operations in the mid-2000s because the market for large AM aerospace components was not mature enough at that time to sustain the business.

Shortly after the demise of AeroMet, Lockheed Martin Aeronautics Company began an implementation program for titanium alloy AM components on the F-35 program.[18] Electron beam directed energy deposition (EBDED) was the chosen AM method. The primary objective was cost reduction, and the approach was to develop a direct swap-out for existing die forgings and parts machined from thick plate. For a direct swap to occur, the mechanical properties of the AM material had to be equal to or better than the existing material properties. LM Aero conducted an extensive coupon testing program to evaluate the performance of EBDED Ti-6Al-4V extra-low interstitial grade (ELI) and to compare it to the baseline die-forged material. The static properties were slightly lower (≈ 5%), though the fatigue and fracture properties were comparable to the baseline. Because the durability requirements often dominate the design life

criteria for airframe parts, the material was determined to be acceptable for use on the program. Currently, specific structural components are being evaluated for pilot implementation on the F-35 platform using the EBDED additive manufacturing process.

Repair of existing components is an AM application area with high potential.[19-20] While not considered AM at the time, one the first true applications of the process was for repairing turbine blade tips in gas turbine engines.[21] Turbine blade tips wear due to the extreme environment in the hot section of a turbine engine. The efficiency of the engine can decrease as the tips wear away due to the increased flow of air between the blade tip and the turbine case. These blades are very expensive to produce, and repair is greatly preferred over replacement. In the early 1980s, the major gas turbine engine producers began exploring laser cladding as a method for adding material onto worn turbine blades. This application was very successful, and most gas turbine engines in operation today use repaired blades. The business case for repair is becoming even more compelling as engine companies are moving toward integrated disks/rotors and blades (e.g., bladed disks, or blisks). The value of these integrated systems is much higher and provides a very compelling argument for AM repair of worn or damaged components.

Reproducing existing parts, providing spares, and repairing damaged components are all very good applications for AM. The freeform nature of the processes, however, offers tremendous opportunity for creating novel structures that would be difficult, if not impossible, to produce otherwise. Component unitization is a good example of a key advantage provided by AM. By combining multiple individual parts into a single AM component, much of the manual labour involved in preparation and assembly can be removed from the manufacturing process. A perfect example of this concept is the fuel nozzle being developed by GE Aviation for use in their new LEAP gas turbine engine.[22] This part was originally an assembly of twenty separate parts. It is now a single component produced in a single AM process.

Topology optimization is another design concept enabled by the use of additive manufacturing.[23-27] In topology optimization, finite element modelling is used to determine the most effective use of material based on the given part constraints and loading conditions. The process constraints of traditional fabrication methods often influence the final design of a part. For example, a part made using three-axis milling cannot incorporate complex, out-of-plane features. With AM, these constraints are lifted and virtually any shape can be created. Topology optimization can help guide part design and determine exactly where material should and should not be to achieve the most efficient design. This concept was demonstrated for an Airbus A320 nacelle hinge bracket.[24] The original design was limited by the conventional milling process, which led to a design where the load was inefficiently distributed through the part. Converting the manufacturing process to AM greatly opened up the design space. Successive optimization cycles eventually led to an optimized design that met the original service load criteria while saving considerable weight. Through smart design, AM can create new opportunities for improved performance.

Additive manufacturing can also create opportunities for novel design using reverse engineering techniques. The biomedical community has successfully demonstrated this concept in the creation of custom implants.[28-29] By using computed tomography (CT) scans of a patient's own anatomy, a near-perfect replica can be created for implantation. The Brazilian Institute of Biofabrication in Campinas, São Paulo, Brazil, demonstrated the use of AM to fabricate a cranial replacement patch for a patient suffering from a severe head defect.[29] In addition to implants, there is a strong market for custom medical tooling for orthopaedic surgery. Surgical tools can be custom designed for each patient to aid in the placement of screws, fixtures, and other orthopaedic in vivo devices

Another useful design feature enabled through AM is the creation of random foamlike or periodic open lattice structures.[30] Computer-aided design can be used to create features that

mimic organic materials like bone and can lead to graded density structures that have graded properties such as stiffness. Open-cell lattice structures are being applied to orthopaedic implants because they provide excellent osteo-adhesion to existing bone and result in a superior mechanical interface between the implant and bone.[31]

Mass customization is an obvious benefit of additive manufacturing.[32] Because most AM processes require little or no tooling, the only fabrication constraint is the design itself. Similarly, AM makes on-demand fabrication possible, which has significant benefits for industries where production volumes are small.[33] This advantage is very important for spacecraft production. Satellite systems are often highly customized and have very low production rates. Planetary probes are often unique, one-of-a-kind vehicles. AM can play a very important role in this particular industry.

While the advantages of additive manufacturing are great, there are a number of challenges and limitations that need to be addressed. The powder bed fusion processes are limited in the part sizes they can produce. While the equipment manufacturers are constantly expanding their process envelopes, part size limitation is still an issue for large, highly complex structures. The directed energy deposition processes are much more scalable, though this feature comes at the expense of complexity and resolution. Residual stress and distortion are challenges for all processes, but they become much more severe as the scale of the process increases.[34-35] All AM processes suffer from surface finish issues.[36] For fatigue-limited structures, the as-deposited surface finish is rarely acceptable, and some level of post-processing is required. Another inherent challenge is controlling internal defects. The incremental nature of the process allows for a high level of control of the microstructure but also introduces opportunities for defects. The grain structure in the as-deposited structures can also create issues. Solidification is highly directional, which leads to oriented (i.e., columnar) grains that give rise to nonisotropic behaviour.[37] Inspection can also be a challenge with AM

parts.[38] The near-net shape aspect of the AM process makes conventional methods, like ultrasonic inspection, challenging or impossible. The geometric complexity enabled by AM also makes traditional radiography difficult. Consider the complex part shown in Figure 5.2b; a side-view 2D radiograph would be very difficult to interpret and identifying an individual pore would be extremely challenging. All of these processing and materials issues need to be addressed for AM to expand into critical hardware applications. Finally, the ability to design for additive manufacturing and adequately analyse the designs using existing finite element tools are limiting aspects of the current state of additive manufacturing.

5.3 Economics and Productivity

Additive manufacturing can have tremendous economic advantages for a wide variety of applications;[39-40] however, it is important to note that additive manufacturing is not universally applicable to all parts. The economics must be carefully considered for each part family. One of the key metrics used in the aerospace industry is the "buy-to-fly" ratio. This ratio compares the amount of material purchased to the amount of material that actually flies on the vehicle. For airframe structures produced via conventional methods (e.g., forging), the buy-to-fly ratio can be 10:1 and higher, resulting in a scrap rate well above 90%.[10] Some challenging structures can even exceed a 100:1 buy-to-fly ratio. These parts are ideal candidates for AM, assuming their geometries are suitable for fabrication by AM. Figure 5.3 shows a cost breakdown comparing a die forged titanium alloy component with the same component fabricated using electron beam directed energy deposition.[18] The cost values are given in relative units but demonstrate the tremendous cost savings potential through AM. In this specific case, the cost savings is realized through all three major cost categories: the part costs less to deposit versus forge, it costs less to machine since there is less material to machine away, and it costs less in raw material, which greatly lowers the buy-to-fly ratio. For the highest-value airframe

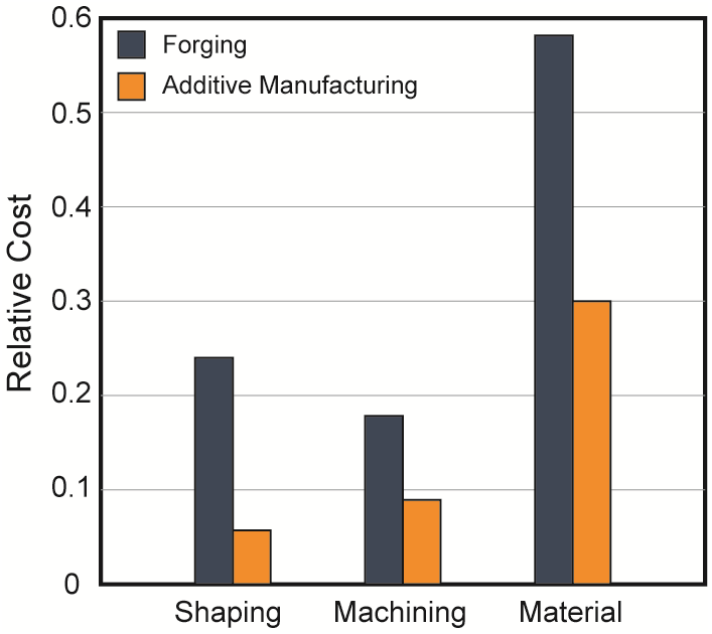

Figure 5.3: *Relative cost breakdown for a candidate additively manufactured large titanium aero structure part.The sum of the forging cost is normalized to one. Adapted from Brice.*[18]

components, which can cost more than $100,000 USD, the overall cost savings over the production run of the vehicle can be very high.

For very short production runs, which are typical of military aircraft, the cost to produce a part using AM can often be less than a conventional method. For small parts or parts with high production volumes, there is often a point in the production run where it becomes more cost effective to produce the part using the conventional approach. Any conventional method that requires tooling (e.g., die forging) has high per-part costs for low production runs. As production volume increases and the cost of the tooling is spread out over many more parts, the conventional fabrication approach can become more cost effective. It is important to know where the cost curves intersect to determine the overall lowest-cost method of production. An example provided by Atzeni and Salmi demonstrates this concept.[41] An aluminium landing gear component was evaluated for fabrication using laser PBF additive manufacturing and traditional die casting. All relevant production costs were considered between the two processes. At a production volume of one unit, the die casting process cost is over 21,000 €

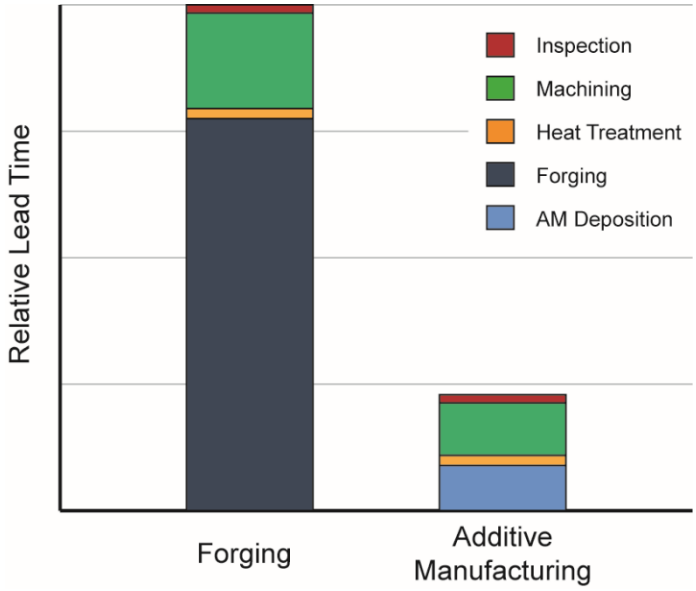

Figure 5.4: *Relative lead time breakdown for a candidate additively manufactured large titanium aero structure part. Adapted from Brice.*[18]

while the AM cost is just over 500 €. The AM production cost remains flat since there is no tooling to amortize. The die casting production costs quickly drop until the two methods reach parity at 42 production units. Each candidate part for AM fabrication must be weighed in a similar manner against conventional processing methods.

In addition to cost reduction, lead time reduction is another significant advantage of AM. The two examples discussed above also demonstrated a significant lead time reduction. The specific lead time breakdown for the die forged titanium aerospace component is shown in Figure 5.4. The forging lead time is very long due to die set(s) fabrication and forging press availability. The overall schedule reduction for using AM over die forging is approximately 75%. For schedule-driven vehicles, an advantage of this magnitude can tip the scale in favour of AM. Similarly for the die cast aluminium component, the estimated lead time for the AM part is 2.5 days compared to multiple weeks for the die cast part.

5.4 Materials

There is a wide range of commercially available alloys that can be used for additive manufacturing.[11] These materials are industry standard compositions that predate the

emergence of AM technology. Most, like AlSi10Mg and Ti-6Al-4V, were formulated many decades ago and were optimized for other processes such as casting or wrought processing. For wire-fed AM processes, welding wire feedstock is most often used because it is commonly available. Many welding filler compositions, however, were designed for joining and typically have trace modifications to their composition compared with the base alloy (e.g., Al 2319 with slightly elevated titanium content as a filler metal for Al 2219). The steep thermal gradients associated with welding lead to large grains, often with a columnar orientation.[42] Trace modifications to the filler wire are meant to minimize these solidification effects and give a higher-performance, crack-free joint. These modifications can also be beneficial to AM-processed filler wire, since the deposit is essentially stacked weld beads.

In addition to wire, powdered metal is used for a variety of AM processes, including both directed energy deposition and powder bed fusion processes. Metal powder for AM is generally made using atomization processes, which produce spherical powder with flow characteristics well-suited to AM processes. Inert gas atomization uses a high-velocity gas stream injected into a stream of molten metal to create an atomized mist of molten particles.[43] The atomized particles quickly solidify into spherical powder particles as they free-fall through the processing chamber before collecting at the bottom. Gas atomization creates very fine powder particles that, in an AM process, can create very high resolution parts with very smooth surface finishes. One of the two major problems encountered with gas atomization is that the gas can get trapped in the powder particles during solidification. This void can then be transferred to the part during AM processing.[44] The other problem with gas-atomized powder is the tendency for the powder to form satellites during solidification. Satellites form when smaller particles stick to larger particles and create a particle cluster. Satellites can affect the ability of the powder to flow, resulting in poor performance in AM processes.[37]

The rotating electrode method is another atomization process that is often used to make powder. In the rotating electrode method, a rod or wire of the base material is rotated around its major axis while one end of the rod or wire is melted using a heat source such as a plasma torch.[43] The molten ball that forms on the end of the rod or wire is ejected because of the rotational forces and is atomized into a fine mist. The mist quickly solidifies into spherical particles prior to the material contacting the chamber wall. The rotating electrode method generally produces highly spherical, satellite-free powder; however, the size distribution is often much larger. Using larger powder in an AM process results in a rougher surface finish and reduces the ability to produce fine details in complex parts.

Wire-based AM methods offer a few advantages over powder-based methods. In wire-based AM processes, the entire wire is consumed during processing, whereas in powder-based AM processes, only some of the powder is consumed.[3] In powder DED processes, overspray of the powder results in less than 100% yield. In PBF processes, only a fraction of the powder bed is melted during a build run. This excess powder can be recycled and reused, but not without challenges. First, highly reactive powders such as aluminium must be kept in an inert environment, making transport in and out of the AM system a challenge. Second, the powder must be sieved and classified to remove particles outside the required size distribution range. Finally, the powder can only be recycled a fixed number of times. Repeated use of the powder causes it to degrade over time, a phenomena that is still not well-understood. Eventually the reused powder will have to be scrapped. All of these factors affect the cost and complexity for a given AM process.

Currently a wide range of metal powders is available for use in both wire- and powder-based AM processes. The limiting factor is weldability—if an alloy can be fusion welded, then it can usually be satisfactorily processed using AM. Many alloys within the titanium, aluminium, nickel, and steel families are commercially available. Titanium is relatively

expensive to produce and process through conventional manufacturing methods, which makes it a good candidate for AM.[18] Conventional titanium alloys, in particular Ti-6Al-4V, have been studied extensively and have been shown to work well in AM processes. Nickel alloys have also been widely studied in AM processes, mainly the Inconel alloys 625 and 718.[45] These high-temperature alloys are used in turbine engines and rocket motors. Some nickel alloys can be more challenging than others to process with AM because of their marginal weldability (e.g., Waspaloy); however, these alloys have been successfully demonstrated.[46]

While there are many commercially available feedstock alloys for additive manufacturing, they were all originally designed for some other processing method such as casting. The thermal conditions in AM processes are considerably different than those in casting or wrought processes. Metal AM methods are most closely related to fusion welding processes, which are characterized by very steep thermal gradients, rapid cooling, directional solidification, vaporization losses, and high residual stress and distortion.[47] Alloys developed for casting or some other conventional fabrication approach are not ideally suited for welding-like processes with very different processing environments.

Metal additive manufacturing can be considered a rapid solidification process (RSP). Much work was done in the 1980s on rapidly solidified metals and alloys.[48-51] The focus at that time was on very high quench rate processes ($\approx 10^6$ K/s), such as gas atomization and splat quenching, that produced particulate materials. The particulates were then consolidated through various methods to achieve functional, solid parts. The main advantage of RSP was the ability to achieve nonequilibrium microstructures and novel mechanical and physical properties. The limitation of RSP was the need to post-process the particulate material into a usable shape, which usually resulted in the loss of some or all of the benefits gained through RSP. Aside from certain niche markets, early RSP work never transitioned into significant production applications.

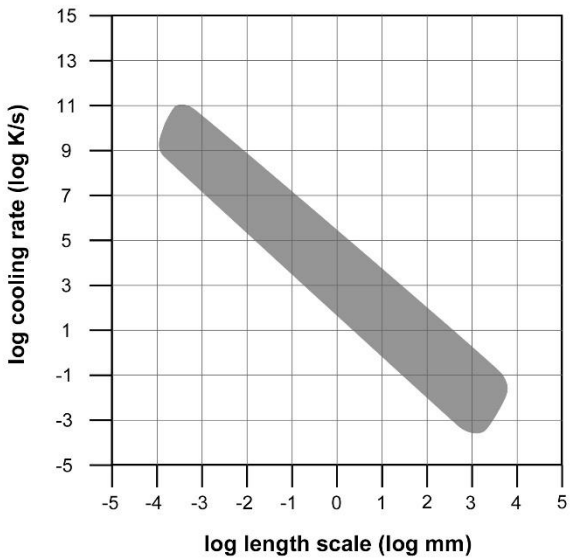

Figure 5.5: *Relationship between molten length scale dimension and cooling rate for a broad range of metallurgical processes. Adapted from Hofmeister.*[55]

The emergence of AM has provided renewed interest in RSP. Since there is no need for any post-processing that might destroy the nonequilibrium microstructures, AM parts can take full advantage of the rapid solidification benefits inherent to the process. The quench rates are not quite as high as seen in the original RSP work, though they are high enough to create nonequilibrium microstructures and properties.[52-54] Figure 5.5 shows a graph depicting the relationship between the size of a molten metal feature (e.g, solidifying ingot or weld metal bead) and the cooling rate experienced by that feature. The graph is adapted from Hofmeister and covers processes from very slow cooling casting all the way up to the highest RSP methods of laser pulse heating.[55] Various studies have estimated cooling rates for additive processes from 10^4 K/s for powder bed fusion[54], to 10^3–10^4 K/s for powder directed energy deposition[52], to 10^2 K/s for electron beam wire directed energy deposition.[56] These results correlate well with the historical trend provided in Figure 5.5 and demonstrate that the size of the molten pool in any AM process directly correlates to the cooling rate that can be achieved in the material. Clearly, to take full advantage of the RSP benefits of AM, the PBF methods with a very small molten pool are best. Even at the relatively slow cooling end of the spectrum as seen in EB

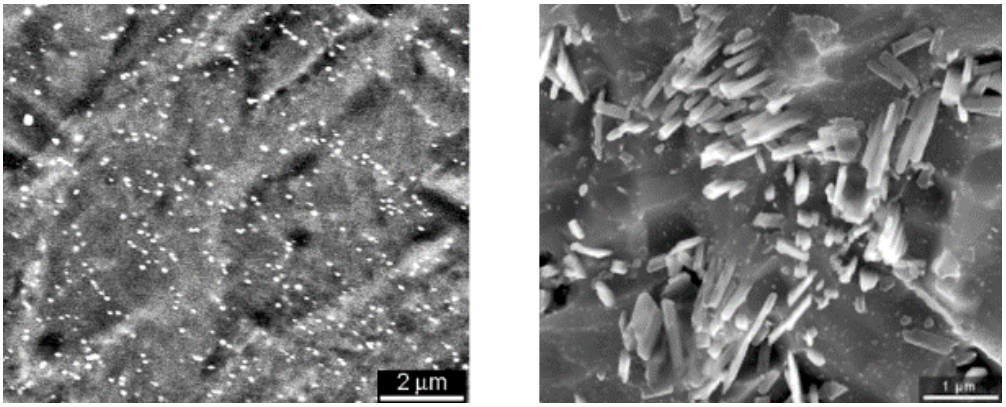

Figure 5.6: *Examples of composites formed by in situ reactions during the additive manufacturing process: Ti-8Al-1Er alloy with a fine Er_2O_3 dispersion (a), from Brice.[61], and Ti-1B alloy with TiB_2 rod-shaped precipitates (b), from Brice et al.[60]*

DED (10^2 K/s), there is still the potential for RSP benefits. Zakharov and Rostova showed an increase in solubility of scandium in aluminium of over 50% at a modest cooling rate of 50 K/s.[57] Additionally, Tomus et al. demonstrated, using electron beam remelting, that a hypereutectic Al-2Sc (wt%) could solidify without any primary Al_3Sc forming.[58] While not measured, the cooling rates in Tomus's experiment were within the range expected in AM processes. At this time, more research is needed regarding how to leverage the benefit of increased solubility through AM processes.

Another metallurgical advantage offered through additive manufacturing is the ability to create composite materials through in situ reactions. The rapid solidification ensures that any reaction product will be very small (submicron), and the incremental nature of the process ensures that the reaction product is homogeneously distributed. Two examples of this type of in situ reaction are shown in Figure 5.6. The first example is a titanium in situ composite created with the addition of the rare earth element erbium. Rare earth elements react strongly with interstitial oxygen in the titanium matrix and generally form incoherent sesquioxides (M_2O_3). Under slow solidification rates typical of a casting process, these oxide particles form large agglomerations that are detrimental to mechanical properties. Under rapid solidification, however, nanometre-sized particles form that are uniformly distributed within the matrix. This particle formation and distribution was demonstrated using the laser powder directed energy

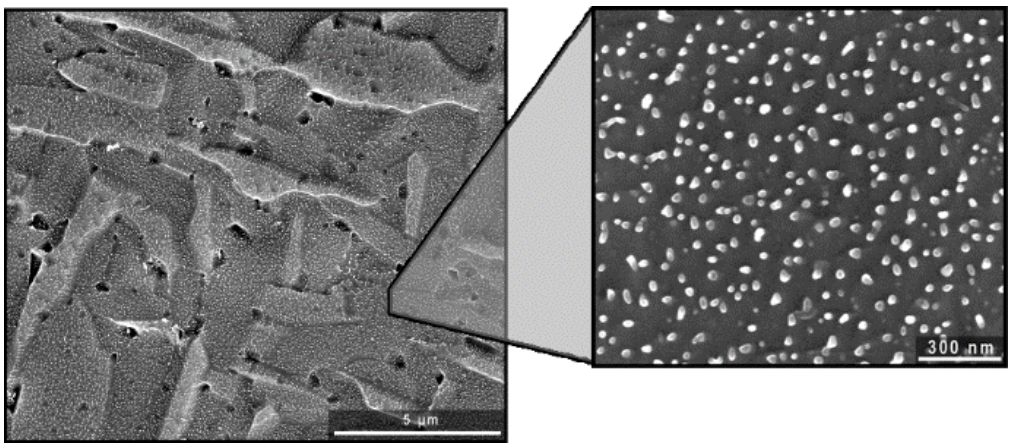

Figure 5.7: *Micrograph showing reactive gas alloying of titanium with nitrogen. Image on right shows close-up of nanoscale titanium nitride particles. From Brice.*[61]

deposition process and pre-alloyed Ti-8Al-1Er powder.[59] The initial deposition pass created a supersaturated solid solution with no evidence of a separate erbium-bearing phase in the material. Subsequent passes heated the material enough to precipitate out the erbium, forming a fine distribution of Er_2O_3 particles. This result is a good example of microstructure that can only be produced using a rapid solidification method such as AM.

The second example, shown on the right in Figure 5.6, is of an in situ reaction formed in a laser powder DED AM process using blended powders.[60] Commercially pure (CP) Grade 2 titanium powder was blended with elemental boron powder and deposited using a DED AM process. In the molten state, the titanium reacted with the boron to produce a homogeneous dispersion of nanoscale TiB_2 particles. The static mechanical properties in this alloy were significantly higher than the deposited Grade 2 titanium alone, with greater than 200% improvement in both 0.2% offset yield strength and ultimate tensile strength. Again, this is an example of an alloy that could not be created through conventional wrought processing, as it requires the rapid solidification rate inherent to the AM method.

In situ reactions can also be accomplished using reactive gas alloying. Under normal processing conditions, the AM method is conducted either in a vacuum or under inert gas such as argon. By introducing a reactive gas into the AM environment in a controlled manner, an in

situ reaction can take place that results in the formation of a second phase. Figure 5.7 shows an example of this technique in which CP Grade 2 titanium was deposited in the presence of a small, controlled amount of nitrogen gas.[61] The nitrogen gas reacted strongly with the molten titanium and formed nanoscale titanium nitride particles. The advantage of this method is that the alloying solute can be controlled and moderated throughout the deposition sequence. By turning the reactive gas on or off at select locations during the deposition process, a composite structure can be made with areas of high solute and areas of low or no solute. Automated control of the process can create unique structures with tailored properties.

Additive manufacturing enables the fabrication of functionally graded materials, something that is difficult to achieve using conventional processing methods. In addition to the reactive gas method described above, multiple feedstock materials can be introduced into the molten pool at the same time. By varying the different feedstock materials over space and time, a graded composition structure can be created that transitions from one alloy to another. This concept could greatly expand the design space for high-performance structures by allowing

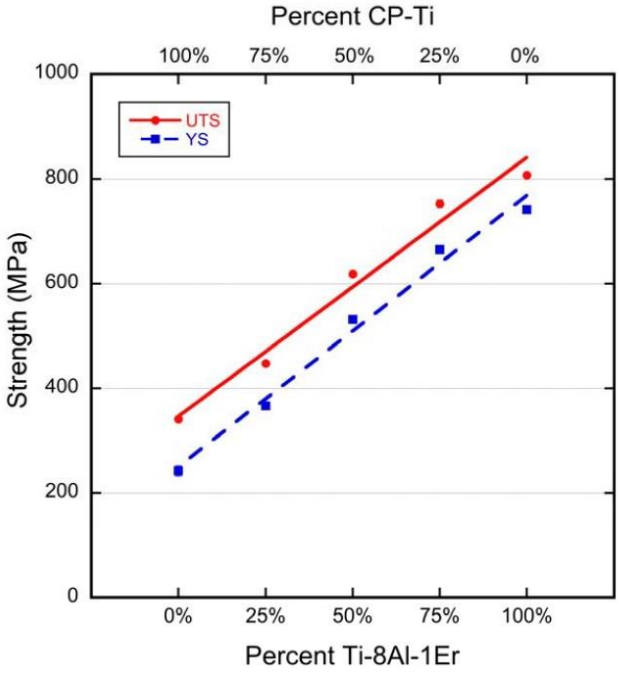

Figure 5.8: *Yield and tensile strength of alloy created by the mixture of two titanium alloys fabricated by electron beam directed energy deposition additive manufacturing. From Brice et al.*[62]

composition, not just geometry, to be optimized for a given load condition. Figure 5.8 shows an example that demonstrates the unique properties available in a functionally graded structure fabricated using electron beam DED.[62] In this example two different wire compositions were used simultaneously: Grade 2 CP-titanium and Ti-8Al-1Er. Deposits were fabricated at 100% of each composition and mixtures of 25%-75%, 50%-50%, and 75%-25%. The tensile properties are shown in Figure 5.8. There is a very clear linear correlation between the composition of mixed alloy and the yield and ultimate tensile strengths. The functionally graded alloy concept using AM has also been successfully demonstrated with other alloy systems.[63] There is a tremendous amount of potential in this area that has yet to be fully explored.

The material limitations are a function of the specific processing environment of each particular AM process and the specific chemical and physical characteristics of each alloy. Highly reflective alloys such as those in the copper and aluminium families are more challenging to fabricate with laser-based AM methods because of the high reflectance of those alloys. An additional complication of Cu and Al alloys is their high thermal conductivity, which makes it more difficult to sustain a stable molten pool.[64]

As mentioned before, the general weldability of a particular alloy or alloy family can determine whether that material can be additively manufactured. Aluminium alloys in the 7xxx series (Al-Zn) are difficult to weld using fusion methods and are therefore not well-suited to additive manufacturing. This is a significant limitation, since the highest strength aerospace-grade alloys are in the 7xxx family. Some alloys that are marginally weldable (e.g., γ-TiAl) can be additively manufactured but benefit when the substrate or the part (or both) are preheated during deposition.[65]

Vaporization loss is another limitation for additively manufactured materials. This is also an issue that has been recognized and studied in the fusion welding of many different alloys.[66-68] Multi-component alloys that contain elements with widely varying vapour pressures can be

difficult to weld reliably. The high-vapour-pressure elements preferentially evaporate from the molten pool and alter the final chemistry. Similar losses occur in additive manufacturing with alloys that are susceptible to preferential vaporization. For electron beam-based processes, the effect is amplified because of the vacuum environment. In addition to altering the chemistry, the vaporization of low-vapour-pressure species can create gas bubbles in the weld pool. In combination with the rapid solidification rate, these bubbles can lead to the entrapment of gas and can create porosity in the solidified metal. The current solution to this problem is to compensate for the vapour loss by adding extra solute into the feedstock material. At the expected vapour loss rates, the resulting deposited material yields the nominal solute concentration.[69] This solves the chemistry problem but may exacerbate the entrapped porosity problem. Ideally, specific alloys designed for AM will take vapour pressure differences into consideration.

Metal additive manufacturing has demonstrated its usefulness in many alloy systems for many structural applications. The commercially available aluminium alloys currently on the market are generally casting alloy compositions and are not considered for high-performance structural applications in the aerospace market. Adaptations of current alloy compositions can remedy this situation; however, there needs to be a thorough understanding of how the alloys respond to the additive manufacturing environment. Key issues are the solidification rate and the vaporization loss, which control how the alloy microstructure develops and what properties can ultimately be achieved. This project will explore these issues with the aim of understanding how to optimize and control AM processes in order to achieve robust and repeatable deposition of aluminium alloys.

References

1. Harter, I. Method of forming structures wholly of fusion deposited weld metal. U.S. Patent 2,299,747, Oct. 27, 1942.

2. Brown, C. O.; Breinan, E. M.; Kear, B. H. Method for fabricating articles by sequential layer deposition. U.S. Patent 4,323,756, Apr. 6, 1982.

3. Gibson, I.; Rosen, D. W.; Stucker, B., *Additive Manufacturing Technologies*. Springer: 2010; Vol. 238.

4. Keicher, D. M.; Smugeresky, J. E., The laser forming of metallic components using particulate materials. *JOM* **1997,** *49* (5), 51-54.

5. Baufeld, B.; Brandl, E.; Van der Biest, O., Wire based additive layer manufacturing: comparison of microstructure and mechanical properties of Ti–6Al–4V components fabricated by laser-beam deposition and shaped metal deposition. *Journal of Materials Processing Technology* **2011,** *211* (6), 1146-1158.

6. Taminger, K.; Hafley, R. A. In *Electron beam freeform fabrication: a rapid metal deposition process*, 3rd Annual Automotive Composites Conference, Troy, MI, 2003; pp 9-10.

7. Murr, L. E.; Gaytan, S. M.; Ramirez, D. A.; Martinez, E.; Hernandez, J.; Amato, K. N.; Shindo, P. W.; Medina, F. R.; Wicker, R. B., Metal fabrication by additive manufacturing using laser and electron beam melting technologies. *Journal of Materials Science & Technology* **2012,** *28* (1), 1-14.

8. Santos, E. C.; Shiomi, M.; Osakada, K.; Laoui, T., Rapid manufacturing of metal components by laser forming. *International Journal of Machine Tools and Manufacture* **2006,** *46* (12), 1459-1468.

9. Ding, D.; Pan, Z.; Cuiuri, D.; Li, H., Wire-feed additive manufacturing of metal components: technologies, developments and future interests. *The International Journal of Advanced Manufacturing Technology* **2015,** *81* (1-4), 465-481.

10. Kobryn, P.; Ontko, N.; Perkins, L.; Tiley, J. In *Additive manufacturing of aerospace alloys for aircraft structures*, Cost Effective Manufacture via Net-Shape Processing, Neuilly-sur-Seine, France, DTIC Document: 2006; pp 3.1-3.14.

11. Frazier, W. E., Metal additive manufacturing: a review. *Journal of Materials Engineering and Performance* **2014,** *23* (6), 1917-1928.

12. Brajlih, T.; Valentan, B.; Balic, J.; Drstvensek, I., Speed and accuracy evaluation of additive manufacturing machines. *Rapid Prototyping Journal* **2011,** *17* (1), 64-75.

13. Horn, T. J.; Harrysson, O. L., Overview of current additive manufacturing technologies and selected applications. *Science Progress* **2012,** *95* (3), 255-282.

14. Beyer, C., Strategic implications of current trends in additive manufacturing. *Journal of Manufacturing Science and Engineering* **2014,** *136* (6), 064701.

15. Paul, B.; Baskaran, S., Issues in fabricating manufacturing tooling using powder-based additive freeform fabrication. *Journal of Materials Processing Technology* **1996,** *61* (1), 168-172.

16. Morrow, W.; Qi, H.; Kim, I.; Mazumder, J.; Skerlos, S., Environmental aspects of laser-based and conventional tool and die manufacturing. *Journal of Cleaner Production* **2007,** *15* (10), 932-943.

17. Rännar, L.-E.; Glad, A.; Gustafson, C.-G., Efficient cooling with tool inserts manufactured by electron beam melting. *Rapid Prototyping Journal* **2007,** *13* (3), 128-135.

18. Brice, C. A. In *Net shape processing of titanium alloys for enhanced performance and improved affordability*, 12 th World Conference on Titanium, Beijing China, L. Zhou, H. C., Y. Lu and D. Xu, Ed. The Nonferrous Metals Society of China: 2011; pp 1697-1703.

19. Mudge, R. P.; Wald, N. R., Laser engineered net shaping advances additive manufacturing and repair. *Welding Journal* **2007,** *86* (1), 44s.

20. Jones, J. B.; McNutt, P.; Tosi, R.; Perry, C.; Wimpenny, D. I. In *Remanufacture of turbine blades by laser cladding, machining and in-process scanning in a single machine*, Solid Freeform Fabrication Symposium, Austin, TX, 2012.

21. Sexton, L. In *Laser cladding: repairing and manufacturing metal parts and tools*, Opto-Ireland 2002: Optics and Photonics Technologies and Applications, Galway, Ireland, March 17, 2003; International Society for Optics and Photonics: 2003; pp 462-469.

22. Zaleski, A. GE's first 3D-printed parts take flight. (accessed October 19, 2015).

23. Vayre, B.; Vignat, F.; Villeneuve, F., Designing for additive manufacturing. *Procedia CIRP* **2012,** *3*, 632-637.

24. Tomlin, M.; Meyer, J. In *Topology optimization of an additive layer manufactured (ALM) aerospace part*, 7th Altair CAE Technology Conference, Warwickshire, UK, 2011; pp 1-9.

25. Emmelmann, C.; Sander, P.; Kranz, J.; Wycisk, E., Laser additive manufacturing and bionics: redefining lightweight design. *Physics Procedia* **2011,** *12*, 364-368.

26. Brackett, D.; Ashcroft, I.; Hague, R. In *Topology optimization for additive manufacturing*, Solid Freeform Fabrication Symposium, Austin, TX, 2011; pp 348-362.

27. Doubrovski, Z.; Verlinden, J. C.; Geraedts, J. M. In *Optimal design for additive manufacturing: opportunities and challenges*, ASME 2011 International Design Engineering Technical Conferences and Computers and Information in Engineering Conference, American Society of Mechanical Engineers: 2011; pp 635-646.

28. Murr, L. E.; Gaytan, S. M.; Martinez, E.; Medina, F.; Wicker, R. B., Next generation orthopaedic implants by additive manufacturing using electron beam melting. *International Journal of Biomaterials* **2012,** *2012*.

29. Jardini, A. L.; Larosa, M. A.; Maciel Filho, R.; de Carvalho Zavaglia, C. A.; Bernardes, L. F.; Lambert, C. S.; Calderoni, D. R.; Kharmandayan, P., Cranial reconstruction: 3D biomodel and custom-built implant created using additive manufacturing. *Journal of Cranio-Maxillofacial Surgery* **2014,** *42* (8), 1877-1884.

30. Murr, L.; Gaytan, S.; Medina, F.; Martinez, E.; Martinez, J.; Hernandez, D.; Machado, B.; Ramirez, D.; Wicker, R., Characterization of Ti–6Al–4V open cellular foams fabricated by additive manufacturing using electron beam melting. *Materials Science and Engineering: A* **2010,** *527* (7), 1861-1868.

31. Heinl, P.; Müller, L.; Körner, C.; Singer, R. F.; Müller, F. A., Cellular Ti–6Al–4V structures with interconnected macro porosity for bone implants fabricated by selective electron beam melting. *Acta Biomaterialia* **2008,** *4* (5), 1536-1544.

32. Diegel, O.; Singamneni, S.; Reay, S.; Withell, A., Tools for sustainable product design: additive manufacturing. *Journal of Sustainable Development* **2010,** *3* (3), 68.

33. Rawal, S.; Brantley, J.; Karabudak, N. In *Additive manufacturing of Ti-6Al-4V alloy components for spacecraft applications*, 6th International Conference on Recent Advances in Space Technologies (RAST), Istanbul, Turkey, IEEE: 2013; pp 5-11.

34. Ding, J.; Colegrove, P.; Mehnen, J.; Ganguly, S.; Almeida, P. S.; Wang, F.; Williams, S., Thermo-mechanical analysis of wire and arc additive layer manufacturing process on large multi-layer parts. *Computational Materials Science* **2011,** *50* (12), 3315-3322.

35. Brice, C. A.; Hofmeister, W. H., Determination of bulk residual stresses in electron beam additive-manufactured aluminum. *Metallurgical and Materials Transactions A* **2013,** *44* (11), 5147-5153.

36. Lanzetta, M.; Sachs, E., Improved surface finish in 3D printing using bimodal powder distribution. *Rapid Prototyping Journal* **2003,** *9* (3), 157-166.

37. Murr, L. E.; Martinez, E.; Amato, K. N.; Gaytan, S. M.; Hernandez, J.; Ramirez, D. A.; Shindo, P. W.; Medina, F.; Wicker, R. B., Fabrication of metal and alloy components by additive manufacturing: examples of 3D materials science. *Journal of Materials Research and Technology* **2012,** *1* (1), 42-54.

38. Waller, J. M., Parker, B. H., Hodges, K. L., Burke, E. R., Walker, J. L., & Generazio, E. R., Nondestructive evaluation of additive manufacturing. NASA/TM-2014-218560, 2014.

39. Huang, S. H.; Liu, P.; Mokasdar, A.; Hou, L., Additive manufacturing and its societal impact: a literature review. *The International Journal of Advanced Manufacturing Technology* **2013,** *67* (5-8), 1191-1203.

40. Huang, R.; Riddle, M.; Graziano, D.; Warren, J.; Das, S.; Nimbalkar, S.; Cresko, J.; Masanet, E., Energy and emissions saving potential of additive manufacturing: the case of lightweight aircraft components. *Journal of Cleaner Production* **2015**.

41. Atzeni, E.; Salmi, A., Economics of additive manufacturing for end-usable metal parts. *The International Journal of Advanced Manufacturing Technology* **2012,** *62* (9-12), 1147-1155.

42. Kou, S.; Le, Y., Nucleation mechanism and grain refining of weld metal. *Welding Journal* **1986,** *65* (4), 65-70.

43. German, R. M., *Powder Metallurgy and Particulate Materials Processing: The Processes, Materials, Products, Properties, and Applications*. Metal Powder Industries Federation Princeton, NJ, 2005.

44. Susan, D.; Puskar, J.; Brooks, J.; Robino, C. V., Quantitative characterization of porosity in stainless steel LENS powders and deposits. *Materials Characterization* **2006,** *57* (1), 36-43.

45. Clark, D.; Bache, M.; Whittaker, M., Shaped metal deposition of a nickel alloy for aero engine applications. *Journal of Materials Processing Technology* **2008,** *203* (1), 439-448.

46. Hussein, N.; Pashby, I.; McCartney, D., Laser and arc weld methods for direct metal deposition of Waspaloy. *International Journal of Manufacturing Technology and Management* **2009,** *17* (4), 419-425.

47. Messler Jr, R. W., *Principles of Welding: Processes, Physics, Chemistry, and Metallurgy*. John Wiley & Sons, Inc.: 2008.

48. Das, S.; Davis, L., High performance aerospace alloys via rapid solidification processing. *Materials Science and Engineering* **1988,** *98*, 1-12.

49. Froes, F.; Kim, Y.-W.; Krishnamurthy, S., Rapid solidification of lightweight metal alloys. *Materials Science and Engineering: A* **1989,** *117*, 19-32.

50. Jones, H., The status of rapid solidification of alloys in research and application. *Journal of Materials Science* **1984,** *19* (4), 1043-1076.

51. Grant, N. J., Rapid solidification of metallic particulates. *JOM* **1983,** *35* (1), 20-27.

52. Zheng, B.; Zhou, Y.; Smugeresky, J.; Schoenung, J.; Lavernia, E., Thermal behavior and microstructural evolution during laser deposition with laser-engineered net shaping: Part I. Numerical calculations. *Metallurgical and Materials Transactions A* **2008,** *39* (9), 2228-2236.

53. Zheng, B.; Zhou, Y.; Smugeresky, J.; Schoenung, J.; Lavernia, E., Thermal behavior and microstructure evolution during laser deposition with laser-engineered net shaping: part II. Experimental investigation and discussion. *Metallurgical and Materials Transactions A* **2008,** *39* (9), 2237-2245.

54. Vilaro, T.; Colin, C.; Bartout, J.-D., As-fabricated and heat-treated microstructures of the Ti-6Al-4V alloy processed by selective laser melting. *Metallurgical and Materials Transactions A* **2011,** *42* (10), 3190-3199.

55. Hofmeister, W.; Griffith, M., Solidification in direct metal deposition by LENS processing. *JOM* **2001,** *53* (9), 30-34.

56. Brice, C. A.; Dennis, N., Cooling rate determination in additively manufactured aluminum alloy 2219. *Metallurgical and Materials Transactions A* **2015,** *46* (5), 2304-2308.

57. Zakharov, V.; Rostova, T., Effect of scandium, transition metals, and admixtures on strengthening of aluminum alloys due to decomposition of the solid solution. *Metal Science and Heat Treatment* **2007,** *49* (9-10), 435-442.

58. Tomus, D.; Qian, M.; Brice, C. A.; Muddle, B. C., Electron beam processing of Al–2Sc alloy for enhanced precipitation hardening. *Scripta Materialia* **2010,** *63* (2), 151-154.

59. Brice, C.; Fraser, H., Characterization of Ti-Al-Er alloy produced via direct laser deposition. *Journal of Materials Science* **2003,** *38* (7), 1517-1521.

60. Brice, C. A., Hafley, R. A., Taminger, K. M., & Wallace, T. A., Laser deposition of boron-modified titanium alloys. Presented at 2005 AeroMat Conference & Exposition, Orlando, FL.

61. Brice, C. A. In *Nitride strengthened titanium via deposition processing*, 11th World Conference on Titanium, Kyoto, Japan, 2007.

62. Brice, C. A., Newman, J. A., Bird, R. K., Shenoy, R. N. Baughman, J. M., & Gupta, V. K., Electron beam freeform fabrication of titanium alloy gradient structures. NASA/TM-2014-218508, 2014.

63. Hofmann, D. C.; Roberts, S.; Otis, R.; Kolodziejska, J.; Dillon, R. P.; Suh, J.-o.; Shapiro, A. A.; Liu, Z.-K.; Borgonia, J.-P., Developing gradient metal alloys through radial deposition additive manufacturing. *Scientific Reports* **2014,** *4*.

64. Buchbinder, D.; Schleifenbaum, H.; Heidrich, S.; Meiners, W.; Bültmann, J., High power selective laser melting (HP SLM) of aluminum parts. *Physics Procedia* **2011,** *12*, 271-278.

65. Murr, L. E.; Gaytan, S.; Ceylan, A.; Martinez, E.; Martinez, J.; Hernandez, D.; Machado, B.; Ramirez, D.; Medina, F.; Collins, S., Characterization of titanium aluminide alloy components fabricated by additive manufacturing using electron beam melting. *Acta Materialia* **2010,** *58* (5), 1887-1894.

66. Block-Bolten, A.; Eagar, T., Metal vaporization from weld pools. *Metallurgical Transactions B* **1984,** *15* (3), 461-469.

67. Pastor, M.; Zhao, H.; Martukanitz, R.; DebRoy, T., Porosity, underfill and magnesium lose during continuous wave Nd: YAG laser welding of thin plates of aluminum alloys 5182 and 5754. *Welding Journal* **1999,** *78*, 207-s.

68. Zhao, H.; DebRoy, T., Weld metal composition change during conduction mode laser welding of aluminum alloy 5182. *Metallurgical and Materials Transactions B* **2001,** *32* (1), 163-172.

69. Brice, C. A.; Rosenberger, B. T.; Sankaran, S. N.; Taminger, K. M.; Woods, B.; Nasserrafi, R. In *Chemistry control in electron beam deposited titanium alloys*, Materials Science Forum, Trans Tech Publ: 2009; pp 155-158.

6.0 ALUMINIUM ALLOYS

6.1 History and Background

Over the past 200 years, aluminium has gone from discovery to high-performance structural material.[1-2] In 1808 Sir Humphrey Davy speculated on the existence of aluminium based on his work reducing other similar elements using electrolysis; however, he was never able to produce a pure sample.[3] Almost 20 years later in 1825, Hans Christian Ørsted produced the first metallic sample reduced from aluminium chloride using potassium. Friedrich Wöhler improved upon this process and was able to produce larger samples. In 1854, Henri Étienne Sainte-Claire Deville further improved upon this process by substituting sodium for potassium. While he was able to produce small bars of material, the process was still cost-prohibitive, and aluminium was considered a precious metal and was rarely used. A process more efficient than chemical displacement was needed before aluminium could become a commodity metal.

Finally, in 1886, Charles Hall of Oberlin College demonstrated the electrolytic reduction of aluminium using molten cryolite (Na_3AlF_6) and aluminium fluoride (AlF_3). At almost exactly the same time, Paul Héroult, a French engineer, independently developed an identical process. Hall beat Héroult to the U.S. Patent and Trademark Office by a few weeks and was granted Patent 400,664 in 1889. Hall opened the Pittsburgh Reduction Company in 1888 to begin producing industrial quantities of aluminium. In 1907 this company became the Aluminum Company of America (Alcoa), which is still in existence today and still uses the Hall–Héroult process for reducing aluminium ore into metal.

Arguably the most important development after the establishment of the Hall–Héroult reduction process was the discovery of precipitation (or age) hardening in aluminium alloys. In the early 1900s, Alfred Wilm of the Neubabelsberg Scientific and Technical Analysis Centre

in Berlin, Germany, began exploring strengthening mechanisms in Al-Cu alloys.[4] Initially Wilm was trying to achieve transformation hardening through quenching—similar to how iron-based alloys were strengthened. Finally, in 1906, while experimenting with an Al-Cu-Mn-Mg alloy, Wilm had a breakthrough. After quenching the alloy from the solution treatment temperature, he measured the hardness and then left the sample for a few days before once again measuring the hardness. Surprisingly, the alloy had increased in hardness due to what we know now as natural room-temperature aging. Wilm repeated the experiment and documented a significant strengthening over time due to room-temperature precipitation.[5] This alloy was patented and licensed to Durener Metalwerke in Duren, Germany, with the trade name Duralumin.[6] Duralumin was initially used in Zeppelin airships and in one of the first commercial aircraft, the Junkers F-13.[7] Alcoa eventually obtained patent rights and commercialized their own version of the alloy under the name 17S.[8] This alloy is still available today under the designation Al 2017.

In the absence of high-resolution analytical techniques, it took many years to determine the exact fundamental mechanisms behind precipitation hardening in aluminium alloys. The presence of the precipitate θ (Al_2Cu) was predicted long before it could be experimentally confirmed. In the 1930s, X-ray diffraction work conducted in Germany confirmed that the precipitation process actually involved stages where the composition of the precipitate phase was the same, but the crystallography was different. This early-stage precipitate phase was labelled θ′. Later that decade, both André Guinier[9] and George Preston[10] independently characterized pre-precipitation clusters, now known as "GP zones," that are the first step in the precipitation sequence in Al-Cu alloys. Many independent studies over many decades have established the current sequence of precipitation in these alloys:

$$\text{Supersaturated Solid Solution (SSSS)} \rightarrow \text{GP zones} \rightarrow \theta'' \rightarrow \theta' \rightarrow \theta$$

This general sequence is also applicable to other aluminium alloy families with a varying number of pre-equilibrium phases.[11] In Al-Zn alloys, the sequence is similar with the η phase ($MgZn_2$).

6.2 Aluminium Alloy Classifications

Aluminium alloys are classified as wrought or cast alloys. The wrought alloys are further divided into heat-treatable (i.e., precipitation-hardenable) and non-heat-treatable compositions. Table 6.1 lists the wrought alloy designations along with their principle alloying constituent(s) and a few of their most important characteristics.[12] A similar scheme exists for cast alloys but is not listed here, since the focus of this project is on wrought-equivalent alloys for additive manufacturing.

Table 6.1: *Wrought aluminium alloy designations.*

Alloy Series	Major Alloying Addition	Heat Treatable	Characteristics
1xxx	Unalloyed: > 99% Al	No	– High corrosion resistance – High electrical and thermal conductivity – 40–150 MPa tensile strength
2xxx	Copper: 1.9%–6.8%	Yes	– High strength – High toughness – 175–425 MPa tensile strength
3xxx	Manganese: 1.3%–6.5%	No	– Moderate strength – Good formability – 100–250 MPa tensile strength
4xxx	Silicon: 3.6%–13.5%	Yes/No	– Highly weldable – 175–375 MPa tensile strength
5xxx	Magnesium: 0.5%–5.5%	No	– Moderate strength – Good corrosion resistance – Weldable – 125–350 MPa tensile strength
6xxx	Magnesium: 0.5%–1.5% Silicon: 0.2%–1.7%	Yes	– Moderate strength – Good formability and machinability – 200–350 MPa tensile strength
7xxx	Zinc: 1.0%–8.2%	Yes	– Very high strength – Prone to stress corrosion – 500–600 MPa tensile strength
8xxx	Other (e.g., Lithium)		

In addition to the alloy designation scheme, there is also a designation scheme for the temper condition of the alloy.[13] Rarely are wrought aluminium alloys used without some form of temper, be it strain hardening for non-heat-treatable alloys or a solution treatment and age heat treatment for heat-treatable alloys. Table 6.2 lists the most common aluminium alloy temper designations. There are additional complexities to the temper designation system for more complex treatments. For example, the temper designation T_51 is for plate that is stress-relieved through stretching. These special tempers are developed for very specific alloys with very special property requirements.

The complex nature of structural aluminium alloys makes choosing the proper alloy for additive manufacturing (AM) difficult. As mentioned in Chapter 5, the casting alloy AlSi10Mg

Table 6.2: *Aluminium alloy temper designations.*

Condition		Meaning
F		As fabricated
O		Annealed
W		Solution heat treated
H		Strain hardened
	H1	Strain hardened only
	H2	Strain hardened and partially annealed
	H3	Strain hardened and stabilized
	The second digit signifies level of strain hardening	
	H_2 = ¼ hard; **H_4** = ½ hard; **H_6** = ¾ hard; **H_8** = full hard; **H_9** = extra hard	
T		Thermally treated to produced tempers other than F or O
	T1	Cooled from an elevated temperature shaping process and naturally aged to a stable condition
	T2	Cooled from an elevated temperature shaping process, cold worked, and naturally aged to a stable condition
	T3	Solution heat treated, cold worked, and naturally aged to a stable condition
	T4	Solution heat treated and naturally aged to a stable condition
	T5	Cooled from an elevated temperature shaping process and artificially aged
	T6	Solution heat treated and artificially aged
	T7	Solution heat treated and stabilized
	T8	Solution heat treated, cold worked, and artificially aged
	T9	Solution heat treated, artificially aged, and cold worked
	T10	Cooled from an elevated shaping process, cold worked, and artificially aged

is the only commercially available alloy for additive manufacturing, except for welding filler wire compositions that can be used in wire-fed directed energy additive processes. There are two major factors influencing aluminium alloy selection for AM: mechanical performance and weldability.

Cast aluminium alloys are generally similar in composition to the alloy classes listed in Table 6.1, with the exception that cast aluminium alloys have overall higher levels of silicon. Silicon forms a eutectic with aluminium at 11.7 wt% Si and improves castability by increasing molten fluidity and reducing the tendency for hot tearing. The trade-off is that the Si phase is hard and reduces the ductility and overall toughness of cast alloys.[14] This reduction in toughness limits the usefulness of cast aluminium alloys in structural aerospace applications. The commercially available alloy AlSi10Mg falls into this category; the poor toughness of the alloy prohibits its use in critical aerospace structural applications. Although there are certainly many opportunities to use this alloy as secondary structure in high-performance systems, it will never be appropriate for use in primary, load-bearing structure.

Weldability is the other major issue with aluminium alloys for additive manufacturing. While weldability encompasses many factors such as reflectance (for laser welding) and vaporization loss, of particular interest here is hot cracking during solidification. Many aluminium alloys are susceptible to hot cracking because of their solidification path.[15-16] This path involves the initial formation of a primary phase, usually through dendritic solidification. The interdendritic liquid flows and redistributes between the dendrites as solidification progresses. As solidification finishes, the last bit of liquid that forms a film around the dendrite structures can separate, often by eutectic reaction (e.g., Al-Cu, Al-Si). In welding and in additive manufacturing, the mechanical strain induced by clamping or fixturing the part amplifies the effect and can lead to significant hot cracking. The tendency to hot crack is a critical factor in deciding which alloys can be used in AM processes. Hot cracking can be

minimized through proper selection of thermal and mechanical conditions; however, the better approach is to select alloy compositions that are ideally suited to minimize or eliminate hot cracking during processing.

6.3 Strengthening Mechanisms

As mentioned in Section 6.2, aluminium alloys can be broadly classified as heat-treatable or non-heat-treatable. The non-heat-treatable alloys can be strengthened using solid solution effects, a distributed second phase, dispersoid particles, strain hardening, and grain refinement.[17]

Solid solution strengthening is achieved by adding soluble elements to the alloy. The solute element has a different atomic radius compared with the solvent element, and this atomic size difference creates localized strain fields around the solute atoms. This size misfit strain is usually associated with substitutional solid solutions where the solute atom displaces an atom from its regular lattice position. Interstitial solid solutions contain solute atoms in the interstices between regular lattice positions and can introduce a shear strain component. Regardless of type, dislocations interact with the strain fields created by the solute atoms and reduce the overall mobility of the dislocations. The result is an increase in the critical resolved shear stress, which leads to higher overall yield strength.

A distributed second phase can form upon cooling though a variety of phase change reactions, such as the eutectic reaction. The second phase will have a different crystal structure and preferred dislocation slip system(s) relative to the parent phase. Dislocation propagation across the phase boundary is difficult because of the crystallographic mismatch. The result is an increase in alloy strength.

Dispersoid particles are formed upon solidification and can interact with dislocations in a manner similar to a distributed phase when the dispersoid particles are shearable. In instances where the distributed phase is not shearable, there is a different interaction mechanism

responsible for the strengthening. This mechanism was first proposed by Orowan in 1948.[18] Over the years, numerous modifications have been made to refine Orowan's original concept. The modified Orowan equation is generally represented by

$$\tau = 0.81 \frac{\mu b}{2\pi\lambda(1-\nu)^{1/2}} ln\left(\frac{R}{r_0}\right) \quad 6.1$$

where μ is the shear modulus, b is the Burger's vector, λ is the mean particle spacing, ν is Poisson's ratio, and R and r_0 are the outer and inner cutoff distances of the dislocation, respectively. The constant 0.81 accounts for randomness in the particle distribution. Strain hardening is due to dislocation interactions with other dislocations and defects within the crystal structure. Strain hardening is most often accomplished through cold working the material. During cold working, dislocations interact with other dislocations, hindering their ability to move. Pinned dislocations can multiply by forming loops, which can greatly increase the volumetric density of dislocations within the material. This multiplication, along with continued entanglement and interaction with other crystal features, such as second phases and grain boundaries, leads to an increase in critical resolved shear stress, which makes it more difficult for dislocations to travel through the material.

For heat-treatable alloys, all the above strengthening mechanisms can also be active, though the primary strengthening comes from a different contribution—precipitation hardening. As briefly described in the beginning of the chapter, precipitation hardening was discovered accidently by Alfred Wilm in the early 1900s. Over the past century, much has been learned about the specific mechanism involved in precipitation processes and how they contribute to the overall strength of the material. Precipitation-hardened alloys are designed to have a primary alloying solute or solutes exceed the room temperature equilibrium solubility limit of the aluminium matrix. Prior to use, the alloys are heat treated to a very high temperature ≈ 90% of the absolute melting temperature (T_m) to dissolve some or all of the alloying solute(s) into solid solution. Rapid quenching retains the solid solution in a supersaturated metastable

condition. A low-temperature aging heat treatment (30–50% T_m) is then performed to precipitate out the supersaturated solute in a controlled manner. Precipitation by this method often leads to a very small (1–100 nm), very finely distributed second phase that can interact with dislocations in a variety of ways, leading to a significant strengthening increment.

The way in which a precipitate interacts with dislocations depends on how the precipitate is crystallographically related to the matrix and whether or not the dislocation can cut through the precipitate as it moves through the crystal. These effects can often be determined by the size of the precipitate as it nucleates and grows during the aging process.

The early stages of precipitation begin with the formation of solute clusters. The clusters are aided by quenched-in vacancies in the lattice formed during the solution heat treatment step. The clusters are usually crystallographically indistinct and are not considered a precipitate, though they provide the nucleation site for the second phase as aging progresses. Solute clusters can provide a strengthening increment due largely to modulus strengthening. Modulus strengthening arises from the fact that the energy of a dislocation (E_d) is directly related to the shear modulus (μ) of the material[17]

$$E_d \propto \mu b^2 \tag{6.2}$$

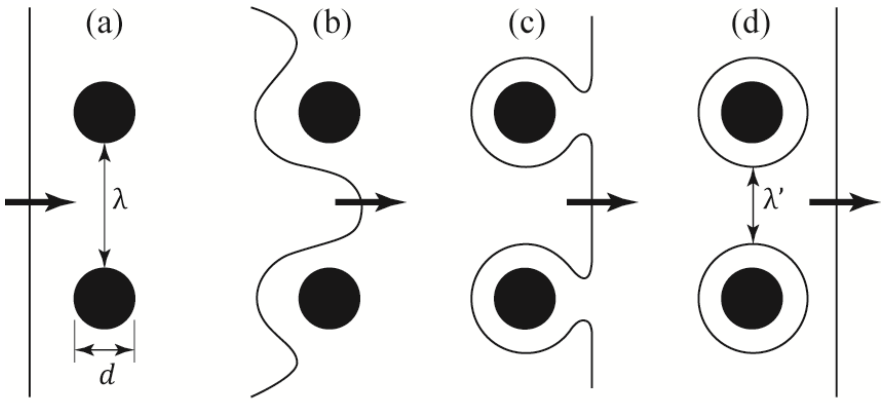

Figure 6.1: *Schematic of Orowan strengthening mechanism. A dislocation approaches non-shearable particles of diameter d with interparticle spacing λ (a); the dislocation bows between the particles (b); loops are formed around the particles (c); and, finally, the dislocation passes, leaving behind dislocation loops around the particles (d), reducing the effective interparticle spacing to λ'.*

note, however, that the actual energy is dependent on whether the dislocation is an edge or screw type. The formation of solute clusters creates local areas in the crystal where the shear modulus is different. Dislocations residing are areas with different shear modulus have a different internal energy. The difference in internal energy creates and interaction force as the dislocation moves through areas with a different shear modulus. Moving from a low modulus area to a high modulus area (e.g. cluster or particle) requires an increase in energy. This effect is negligible at the cluster stage, because the clusters soon disappear to form a distinct second phase upon continued aging. However, modulus strengthening continues to act as the precipitate particles mature into more stable phases.

As the aging heat treatment progresses, the pre-precipitate clusters begin to form distinct second-phase particles. These particles are referred to as Guinier–Preston zones (or, more commonly, GP zones) for the researchers who independently discovered them as discussed earlier in the chapter. GP zones bring about an additional strengthening component referred to as coherency strengthening. Early in the development of the precipitate phase, the bonding between the matrix and precipitate is coherent. The interatomic spacing of the particle usually differs from that of the matrix. This difference in lattice spacing leads to a strain field around the particles, which interacts with dislocations to provide a strengthening increment. Gladman quantified this strengthening increment as

$$\tau = 4.1\mu\varepsilon^{3/2} f^{1/2} \left(\frac{r}{b}\right)^{1/2} \qquad 6.3$$

where ε is the misfit strain, f is the volume fraction of precipitates, and r is the precipitate radius.[19] Eventually the particles lose coherency with the matrix on at least one interface. At this stage, particles can be sheared by dislocations as the dislocations pass through the material. Particle shearing can lead to additional strengthening mechanisms, one of which is chemical, or interfacial, strengthening. When a dislocation shears a particle, a step is left behind in its wake that creates additional particle/matrix interface. The creation of additional particle/matrix

interface is energetically unfavourable and leads to a resisting force for dislocation movement. This strengthening increment has been quantified by Martin as

$$\tau = 2\left(\frac{3}{\pi}\right)^{1/2}\mu\left(\frac{\gamma}{\mu b}\right)^{3/2}\left(\frac{b}{r}\right)f^{1/2} \qquad 6.4$$

where γ is the particle/matrix interface energy.

Stacking fault strengthening can also be important for sheared particles. Dislocations will often dissociate into two partial dislocations in close-packed lattices, such as face-centred cubic in aluminium. The area between the partial dislocations is a stacking fault in the crystalline structure. Alloys with high stacking fault energy (SFE) attempt to minimize the separation between the partial dislocations. For particles that have low SFE compared with the matrix, the partial dislocations will separate more in the particle than in the matrix, reducing overall energy. In this scenario, the dislocations are attracted to the particles, because the lower SFE in the particles is energetically favourable; however, there is then increased resistance to the dislocation leaving the particle, which adds to the strengthening increment. Martin quantified this increment as

$$\tau \propto \left(\left|\gamma_{sfm} - \gamma_{sfp}\right|\right)^{3/2} b^{-1/2}(rf)^{1/2} \qquad 6.5$$

where γ_{sfm} is the stacking fault energy of the matrix and γ_{sfp} is the stacking fault energy of the precipitate.

The final strengthening mechanism for shearable particles is order strengthening. For particles with an ordered structure, such as θ′, the passage of a dislocation creates an anti-phase boundary (APB) where the ordered structure is disrupted. This is energetically unfavourable and leads to an increased resistance for dislocations to pass through an ordered particle. Martin quantifies this as

$$\tau = \frac{\gamma_{APB}}{2b^2}\left(\left(\frac{3\pi^2\gamma_{APB}fr}{32T}\right)^{1/2} - f\right) \qquad 6.6$$

Eventually, the particles will become too large to be sheared by dislocations and the particle-looping Orowan mechanism will take over (eq 6.1, Figure 6.1). Generally at this point, the solute volume fraction remains constant while the particles start to coarsen in order to minimize the total interfacial energy. This is known as Ostwald ripening after Wilhelm Ostwald, who first qualitatively described the process.[20] Wagner,[21] along with Lifshitz and Slyozov,[22] quantitatively described the coarsening process based on the Gibbs–Thompson effect. The relationship is

$$\bar{r}^3 - r_{t=0}^3 = kt \qquad 3.7$$

where

$$k \propto D\gamma X_e \qquad 3.8$$

$\bar{r}$ is the mean radius and $r_{t=0}$ is the mean radius at time $t = 0$, D is the diffusion coefficient of the solute in the matrix, and X_e is the equilibrium solubility of the solute in the matrix at equilibrium with the second phase.. As a result, small particles will be consumed by larger particles resulting in larger particle diameter (d) and larger interparticle spacing (λ). Coarsening diminishes the strengthening effect and the alloy begins to soften.

During the aging process, these various strengthening mechanisms can individually dominate, become insignificant, or add together.[23-24] This combined effect is shown in Figure 6.2 for an Al-Cu alloy where the precipitation sequence is

$$\text{SSSS} \rightarrow \text{GP zones} \rightarrow \theta'' \rightarrow \theta' \rightarrow \theta$$

The metastable Al_2Cu phases (θ'' and θ') are chemically invariant but have a distinct crystal structure from the equilibrium θ phase. The solid dark curve represents the combined strengthening effects at each stage in the aging process, and the dashed curves represent the individual strengthening mechanisms responsible for the strength increment.

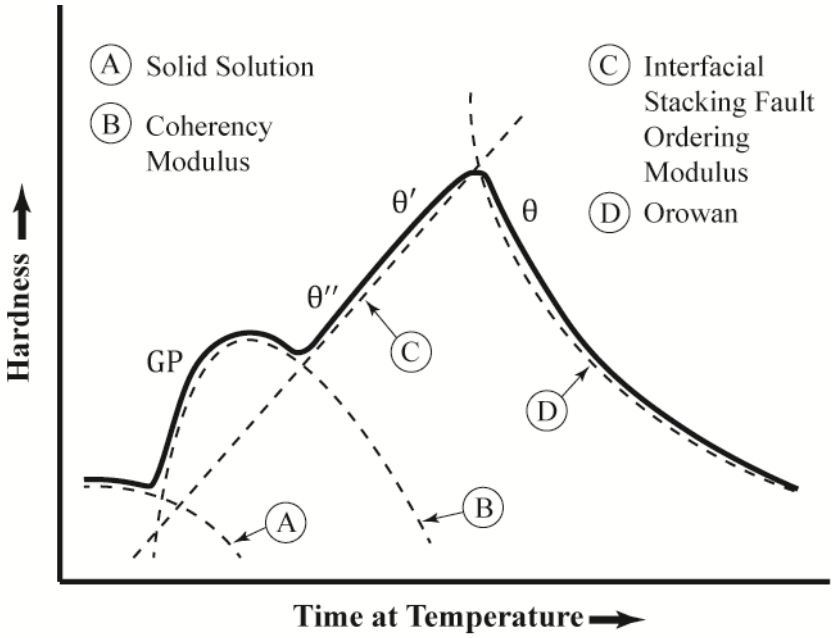

Figure 6.2: *Schematic aging curve showing the various strengthening mechanisms, where they dominate, and where they become insignificant.*

6.4 Aluminium Copper Alloys

In the more than 100 years since the discovery of precipitation hardening in an Al-Cu composition (Duralumin), alloys based on the Al-Cu system have found widespread use in many industries. These alloys continue to evolve as new compositions are formulated, though the underlying primary strengthening mechanism due to Al_2Cu formation remains the same.

The aluminium-copper phase diagram is shown in Figure 6.3. The dilute end of the Al-Cu phase diagram is dominated by a eutectic reaction occurring at 33 wt% Cu at a temperature of 550 °C.[25-26] The reaction products are α_{Al} (fcc) and Al_2Cu (Pearson symbol tI12). The maximum solid solubility of Cu in α_{Al} is approximately 5.7 wt% at 550 °C. Precipitation-strengthened Al-Cu alloys are designed based on these characteristics of the equilibrium phase diagram. The alloys generally have 4–7 wt% Cu, and they are solution heat treated at the temperature corresponding to the maximum solid solubility limit. This dissolves all or most of the Cu into solid solution. The alloy is then quenched to create a supersaturated solid solution (SSSS). Aging of the SSSS can occur at room temperature, bringing about a noticeable

strengthening increment. A more pronounced strengthening effect can be obtained if the alloy is artificially aged at an elevated temperature.[27] The aging heat treatment decreases the amount of time needed to achieve the peak level of hardness compared to natural aging—usually to the point just before the equilibrium θ phase begins to appear (see Figure 6.2).

Most work done to date in additively manufactured Al-Cu alloys has focused on the alloy 2219 (or 2319, the welding wire composition of 2219, which has slightly elevated titanium content for grain refinement).[28-31] Alloy 2319 is nominally 6.3 wt% copper with small additions of manganese (0.20 wt%), titanium (0.15 wt%), vanadium (0.10 wt%), and zirconium (0.175 wt%), principally for grain refinement. This alloy has medium-high strength in the peak aged condition (≈ 400 MPa) and is very weldable, making it a good candidate for AM.

The Cu content in alloy 2319 exceeds the maximum solid solubility; thus, not all of the Cu can be dissolved into solution upon heat treatment. This excess Cu exists as large, distributed equilibrium θ phase in the alloy. The dissolved Cu begins clustering immediately upon

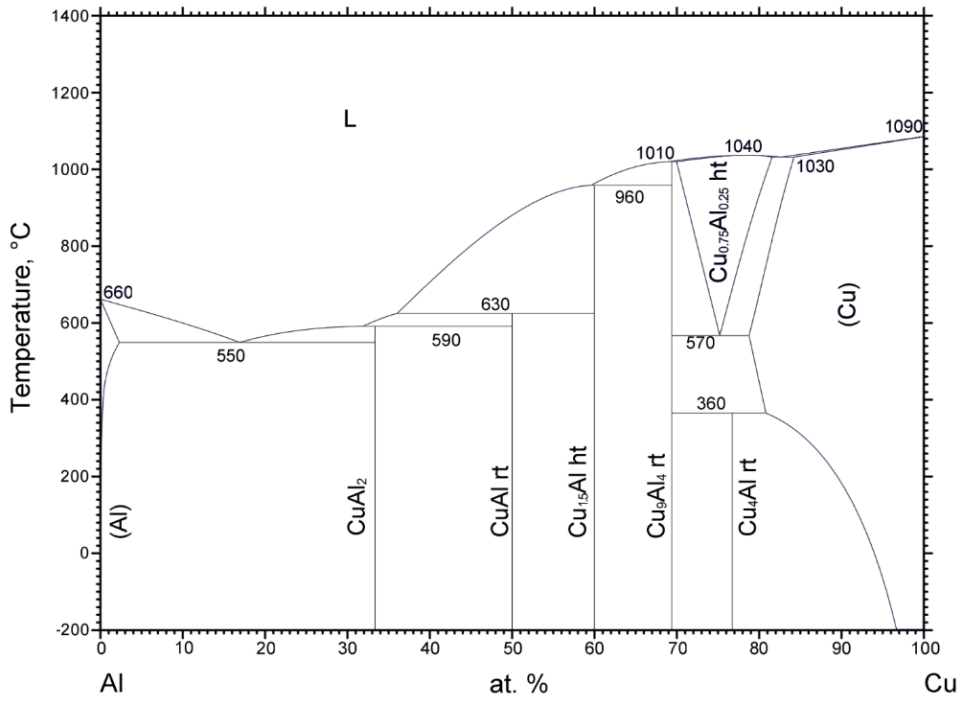

Figure 6.3: *Aluminium-copper phase diagram. From ASM Handbook Volume 3; Alloy Phase Diagrams[27] Reprinted with permission of ASM International. All rights reserved. www.asminternational.org.*

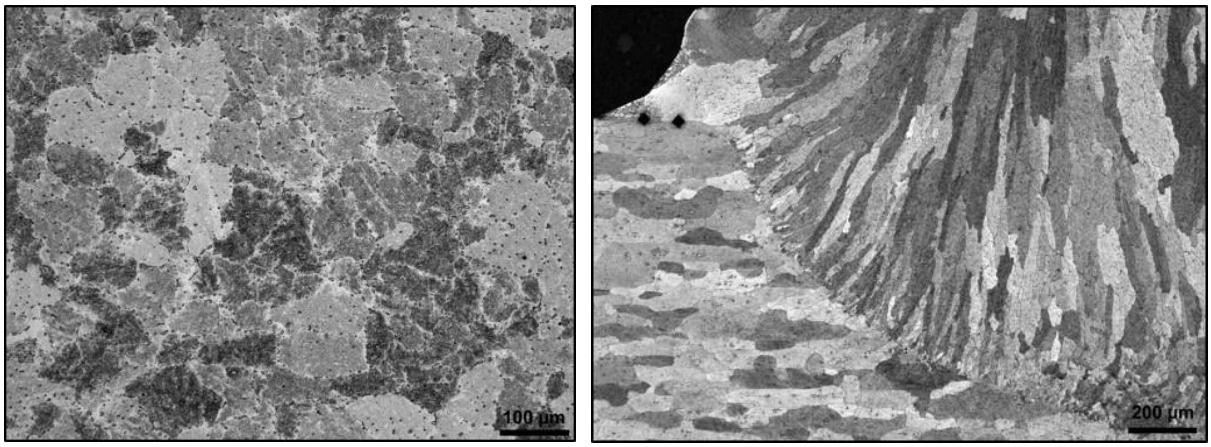

Figure 6.4: *Optical micrographs of electron beam directed energy deposited aluminium alloy 2319. From Brice et al.*[31] *Image credit: NASA.*

quenching from the solution heat treatment process, beginning the precipitation sequence described above. In this alloy, the precipitates form as disc-shaped particles with a habit plane of type $\{100\}_\alpha$. The strengthening of the alloy occurs mainly through artificial aging, bringing about the formation of θ'' and then θ'.

Figure 6.4 shows optical micrographs of additively manufactured 2319.[30] This material was deposited using the wire-fed electron beam directed energy deposition process. The micrograph on the left shows the as-deposited grain structure of the alloy. The equilibrium θ phase (small black spots) is apparent. The micrograph on the right shows the interface of the baseplate and deposit. The as-deposited material solidifies in a columnar nature with the grains oriented in the +z direction (normal to, and growing through the layers). This material has been tensile tested in the as-deposited and aged (T6) conditions. The results are shown in Figure 6.5.[31] In the as-deposited condition, the tensile strength falls between that of the O-temper condition and the T6 peak aged condition in wrought plate material. This tensile strength range is to be expected since the as-deposited material has not been solution treated and aged. Once the T6 condition is applied to the deposited material, the tensile strength values are equivalent to the wrought T6 material.

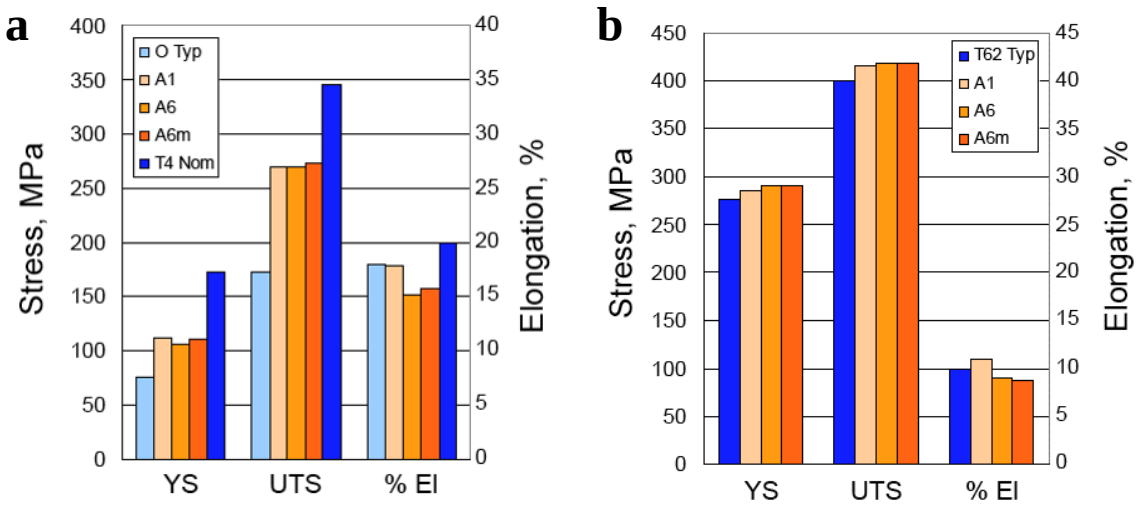

Figure 6.5: *Mechanical properties of as-deposited alloy 2319 (a) and heat treated 2319 (b). From Brice et al.*[32] *Image credit: NASA.*

Alloy 2319, along with many other precipitation-strengthened aluminium alloys, can benefit from a T8 temper condition (solution heat treatment + cold work + artificial age).[32] The addition of the cold working step between the solution heat treatment and the aging heat treatment assists in the precipitation process. Homogeneous nucleation in this alloy is difficult, so it is challenging to get a uniform, widely distributed precipitation of Al_2Cu upon heat treatment. Mechanical working increases the dislocation density of the alloy and provides for precipitate nucleation sites. As a result, the uniformity and density of precipitates increase, which increases the overall strength.

The T8 temper (or the T3 temper, the naturally aged equivalent of T8) is useful and practical for wrought alloys that are easily cold worked. For additively manufactured structures, mechanically working the parts after deposition is contrary to the net (or near-net) shape nature of AM processes. This limits the ability to achieve peak hardness in AM-deposited wrought alloys. A composition that does not require the mechanical working step in order to achieve peak strength is desired for AM processes.

Aluminium alloy 2139 (not to be confused with 2319) is also an Al-Cu composition that is primarily strengthened by the phase Al_2Cu; Table 6.3 shows the chemical composition.[33]

Table 6.3: *Alloy 2139 chemical specification (weight percent).*

Cu	Mg	Ag	Mn	Al
4.5–5.5	0.2–0.8	0.15–0.6	0.2–0.6	balance

This alloy is often specified in the T8 temper condition, though it is much easier to homogeneously nucleate the precipitate phase in this alloy than in other Al-Cu alloys. While the Al_2Cu phase in 2139 is chemically identical to the θ phase in other Al-Cu alloys, its habit plane is the $\{111\}_\alpha$ type, which alters the overall precipitation behaviour. To make a clear distinction, this phase is referred to as the Ω phase in alloy 2139.

The key feature of alloy 2139 that drives the precipitation of Ω over θ is the combined effect of small additions (< 1 wt%) of both magnesium and silver.[27, 34-48] Magnesium was a major component in the very first commercially produced precipitation-hardened aluminium alloys. This alloy combination is still widely used today in alloys such as 2024. In the combined aluminium–copper–magnesium system, the primary strengthening phase is Al_2CuMg, which is known as the S phase.[49] The phase equilibria are dependent on the concentrations of Cu and Mg and can include the θ phase and the T phase (Al_6CuMg_4).[50] Figure 6.6 shows a schematic representation of the 190 °C isothermal section through the ternary Al-Cu-Mg phase diagram. For low Cu to Mg mass ratios (< 7 to 1), the S phase dominates. The precipitation sequence for the S phase closely follows that for the θ phase

$$SSSS \rightarrow \text{GPB zones} \rightarrow S'' \rightarrow S' \rightarrow S$$

where GPB zones are Guinier–Preston–Bagaryatski zones. Bagaryatski is credited for conducting additional X-ray diffraction work on the phase development in these compositions and distinguishing it as a zone containing magnesium and copper. This sequence was recently contradicted by Starink and Wang, who used more conclusive techniques such as atom probe tomography to determine that GPB zones are actually Cu-Mg co-clusters.[51] This clustering effect, prevalent in many dilute Al alloys, has become an important mechanism in the pre-

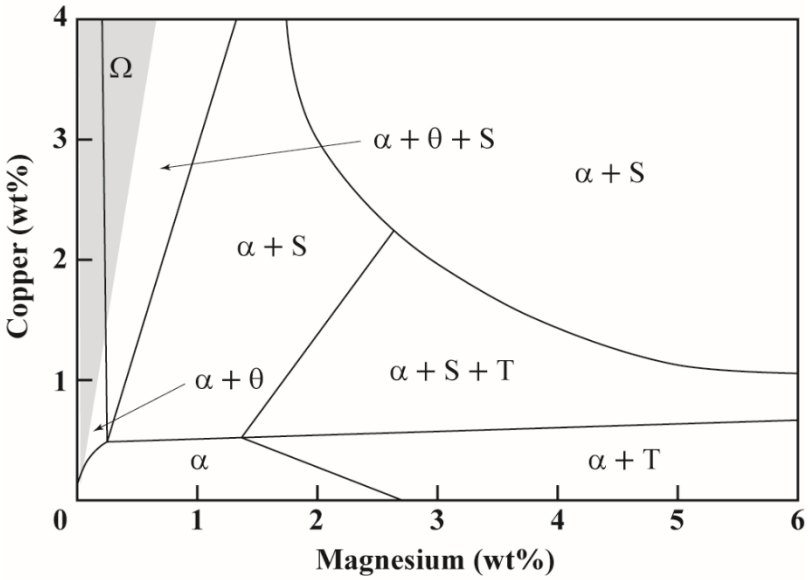

Figure 6.6: *Schematic representation of the 190 °C isothermal section of the Al-Cu-Mg phase diagram showing phase equilibria between α, θ, S, and T. The gray shaded area is where Ω is likely to form (with adequate Mg and Ag additions). Adapted from Ringer and Hono.*[79]

precipitation behaviour of Al-Cu alloys. As the Cu to Mg ratio increases, the θ phase begins to dominate. For the Ω phase to become more thermodynamically favourable than θ, trace addition of Ag is required.

Polmear was the first to document the effect that small silver additions had on the phase development in Al-Cu-Mg alloys.[52] Dilute additions of Ag to Al-Cu-Mg alloys altered the precipitation behaviour and favoured the formation of Ω over θ.[53-59] Importantly, Ag has no effect when added to binary Al-Cu alloys; it is only effective in combination with Mg. The opposite, however, is not true; the Ω phase can develop in Al-Cu-Mg alloys without Ag (contrary to Figure 6.6, which lacks any Ω phase field), though it is usually found in very minor amounts compared to θ and S.

The decomposition of the supersaturated solid solution begins immediately upon quenching. Quenched-in vacancies play a significant role in determining how solute species move throughout the lattice and how initial solute clusters form—a precursor to the formation of distinguishable second-phase structures. Determining vacancy content and vacancy-solute

interactions is difficult, though great progress has been made using positron annihilation spectroscopy.

Positron annihilation spectroscopy is useful in quantifying the void and defect content in metal alloys.[60] Positrons are the antimatter equivalent of the electron. They are generated through nuclear interactions and in spectroscopy, most often by the β^+ decay of ^{22}Na. Positrons are short lived, as they are quickly annihilated by their counterpart, the electron. This annihilation creates energy corresponding to $E = mc^2$, and two-photon emission is the most likely product in metal. The two photons are emitted in opposite directions, though due to the inherent momentum of the positron/electron pair, the photons are not exactly anti-parallel. This feature allows for the determination of the energy shift between the photons using the Doppler Effect, which is useful in characterizing particular solute species that are bound to vacancies.

Positron annihilation lifetime spectroscopy (PALS) is the specific technique used to quantify vacancy and defect content. Positrons are implanted into the alloy and very quickly reach thermal equilibrium, usually within a few picoseconds. Once the positrons are in thermal equilibrium, they diffuse through the material until they are annihilated by electrons. Open volume defects such as vacancies provide traps where the positrons find a local potential energy minimum and can survive longer before being annihilated; thus, by measuring the time between implantation and annihilation, a quantification of the open volume defect density can be determined. The defect structures that affect positron lifetime are (1) vacancies (both bulk and trapped inside solute clusters), (2) solute aggregates, (3) dislocations, (4) incoherent interfaces between the matrix and precipitate, and (5) grain boundaries.

The PALS technique is not effective at determining the chemical composition around vacancies and other defect structures. For chemical identification, coincidence Doppler broadening (CDB) spectroscopy can be used.[61] Certain solute atoms can have a higher affinity for positrons than others, which can alter the shape of the collected Doppler broadening curve.

Typically, pure samples are tested and a Doppler broadening "fingerprint" is determined for that element. When an alloy sample is then tested, the presence of peaks corresponding to the "fingerprint" of a particular element can be used to show that that element is bound to the vacancy in the alloy. This works very well for Cu, which has a well-defined peak at ± 2.1 a.u.; magnesium, however, does not have a strong fingerprint, and thus the presence of Mg at vacancies in Al-Cu alloys must be indirectly determined.

Numerous studies have been done using PALS and CDB on Al-Cu-(Mg-Ag) alloys.[62-68] In Al-Cu-Mg alloys, the general conclusion is that Mg has a much stronger tendency to bind with quenched-in vacancies than Cu. This limits the ability of Cu to diffuse through the matrix and begin the SSSS decomposition process of GP zone formation. The vacancy-Mg complexes that form immediately after quenching begin to migrate to vacancy sinks (e.g., dislocations) in the very early stages of aging. Copper also migrates to the vacancy-Mg complexes forming vacancy-Mg-Cu complexes. These initial complexes act as embryos for further aggregation of Cu. Somoza et al. determined that the bound Cu content at vacancies immediately after quenching is 16% but climbs to approximately 70% after aging. This is in contrast with binary Al-Cu where the Cu from the initial vacancy-Cu pair is gradually released upon aging, allowing for the formation of GP zones.

The addition of silver to Al-Cu-Mg seems to further enhance the vacancy trapping effect. The initial cluster is a vacancy-Mg-Ag complex that also quickly forms upon quenching to room temperature. These solute clusters seem to be preferred nucleation sites for the Ω phase, which only appears to be stabilized through microalloying with both Mg and Ag. Silver alone does not have the same effect. The strong cluster interaction of Ag to Mg is what enables these vacancy-Mg-Ag complexes to form and create nucleation sites for the Ω phase.

Positron annihilation spectroscopy is a useful technique for quantifying open volume defects, but it cannot provide information on the chemical structure of clusters once they begin

to form. Atom probe techniques are particularly useful for determining early structure configurations in precipitation-hardened alloys.[69-70] The atom probe method requires a very sharp needle-shaped sample that is usually either electropolished or ion milled from a larger sample. A voltage is applied to the sample, and atoms are evaporated from the tip by the field evaporation phenomenon. Time-of-flight measurements are used to determine the evaporating species. In one-dimensional atom probe (1DAP), the evaporated species is recorded as the sample tip is progressively evaporated away. This gives a one-dimensional view of the composition of the sample, usually represented by the integrated concentration versus depth into the sample. In this data presentation, a steeper slope of the curve indicates a higher concentration of that particular element at that given position.

A more advanced version of the atom probe technique is the three-dimensional atom probe (3DAP). In this method, a position-sensitive detector maps each evaporating atom in two-dimensional space normal to the depth direction. This added feature allows the full three-dimensional reconstruction of the sample using tomographic methods and clearly shows positional relationships between individual solute species. Three-dimensional atom probe tomography has proven very useful in determining exactly how solute clusters form in Al-Cu-Mg-Ag alloys and how they relate to the eventual precipitation of strengthening phases such as θ' and Ω.[71-78]

Grovenor et al. conducted some of the earliest work in atom probe analysis of Al-Cu-Mg-Ag alloys using position-sensitive atom probe (POSAP), a precursor to 3DAP tomography.[71] In this early study, it was determined that both θ' and Ω were present in the alloy; θ' was very close to the expected Al_2Cu composition, while Ω had less Cu but more Ag and Mg. No evidence was found for the segregation of Mg or Ag to the α/θ' or α/Ω interface.

Subsequent studies have contradicted this last claim that there is not segregation of Ag and Mg to the precipitate interfaces. Sano et al. used time-of-flight 1DAP to determine that Ag

and Mg are found in the Ω phase and also segregated to the α/Ω interface.[72] No Mg or Ag was found in the θ′ phase or at the precipitate interface. The composition of Ω was determined to be 25–35 at% Cu, 1.0–5.0 at% Ag, and 1.2–6.4 at% Mg.

Hono et al. reinforced the conclusion that Ag and Mg both segregate to the Ω particle interfaces.[73] They also corroborated the Ω phase composition with 1–5 at% Ag and 1–6 at% Mg. Contradicting other work using positron annihilation spectroscopy, they concluded that there was no evidence of Ag/Mg clustering in the early stages of aging. The proposed aging sequence of both Ω and θ′ is

$$\alpha \rightarrow \text{GP zones} \rightarrow \theta'' \rightarrow \theta' \text{ (on } \{100\}_\alpha \text{ planes)}$$

$$\rightarrow \Omega \text{ (on } \{111\}_\alpha \text{ planes)}$$

Finally, they concluded that there is no precursor phase upon which the Ω phase nucleates (e.g., Mg_3Ag). This had been suggested by Taylor et al.[79] and Auld,[45] but Hono[70] finds no evidence of such a precursor phase.

Hono, along with Reich and Murayama, has provided the most compelling 3DAP results that clearly show the relationship of Ag and Mg and the precipitate phases Ω and θ′. Hono shows a 3DAP dataset that includes both a Ω precipitate and a θ′ precipitate, as determined by the habit plane on which the precipitates reside ($\{111\}_\alpha$ for Ω and $\{100\}_\alpha$ for θ′).[73] The data clearly show that Mg and Ag segregate to the α/Ω precipitate boundary, while there is no Ag and Mg at the α/θ′ precipitate boundary. The α/Ω interface consists of a monolayer of Mg and Ag with no evidence of either in the bulk of the precipitate. They conclude that the driving force for the formation of Ω on $\{111\}_\alpha$ as opposed to θ′ on $\{100\}_\alpha$ is the reduction of coherency misfit strain on the $\{111\}_\alpha$ planes. Magnesium has a larger atomic radius than Al, and Ag has a larger atomic radius than Cu; thus, by substituting Mg for Al and Ag for Cu, the lattice

expands at the interface, which helps reduce both the overall misfit strain and the barrier for precipitate nucleation.

The crystalline structure of the precipitates cannot be determined by atom probe techniques. Transmission electron microscopy (TEM) is much better suited for crystal structure analysis and for determining orientation relationships between the precipitate and the matrix. A number of attempts have been made to determine the exact crystal structure of the Ω phase and its orientation relationship with the α matrix. The results have often been conflicting, but as TEM techniques have advanced over the years, a consensus regarding the structure has been established.

Auld first established the Ω structure to be hexagonal with lattice parameters a = 0.496 nm and c/a = 1.414.[45] Soon after, Scott et al. determined the structure to be hexagonal in morphology and the particles tend to form very thin hexagonal discs on the $\{111\}_\alpha$ planes.[41] The orientation relationship was established as $\langle 10\bar{1}0\rangle_{ppt} \parallel \langle 110\rangle_\alpha$ and $\langle 0001\rangle_{ppt} \parallel \langle 111\rangle_\alpha$. Later, Knowles and Stobbs and Muddle and Polmear independently determined the structure to be orthorhombic with an orientation relationship of $(001)_\Omega \parallel (111)_\alpha$ and $[010]_\Omega \parallel [10\bar{1}]_\alpha$.[35] Garg and Howe then determined the structure to be tetragonal with the orientation relationship of $(\bar{1}10)_\Omega \parallel (111)_\alpha$ and $[110]_\Omega \parallel [\bar{1}10]_\alpha$.[47] Though there has been much debate, the most accepted view is that Ω is orthorhombic in structure, belonging to the space group Fmmm, and having lattice parameters of a = 0.496 nm, b = 0.859 nm, and c = 8.48 nm. This structure can be regarded as a slightly distorted version of the tetragonal equilibrium θ phase.

The development of the Ω phase over the equilibrium θ phase is dependent on additions of both Mg and Ag. Neither element works on its own to stimulate Ω; both are necessary at specific concentration levels. In Al-Cu-Mg alloys, the equilibrium phases are θ (Al_2Cu) and S (Al_2CuMg) depending on where the concentration lies within the ternary phase diagram (see

Figure 6.6). The simultaneous addition of Ag along with Mg changes the precipitation mechanism and favours the formation of Ω over θ. While it has been well established that Ag is required, the effect at various concentration levels has been up for debate. Gable et al. along with Chester and Polmear determined that beyond about 0.3–0.4 wt%, there was no additional benefit with regard to Ω formation.[46, 52] Zhou et al., however, determined that variations in concentration from 0.14 wt% to 0.57 wt% had a significant effect on age hardening response,[53] though this effect was largely a shift in the peak of the age hardening curve of the high Ag alloy to shorter times. Bai et al. also found a significant difference between an alloy with 0.46 wt% Ag and one with 0.88 wt%.[57] In this study, the number density of Ω precipitates was higher for the 0.88 wt% alloy, which corresponded to a measurable increase in tensile strength.

Magnesium content also plays a critical role in the development of the Ω precipitate. The concentration of Mg must be kept below a certain minimum concentration to inhibit the formation of the S phase. The Cu:Mg ratio of about > 6:1 by weight is the threshold for favouring the precipitation of Ω over θ. Bai examined the effect of three different Mg levels in an alloy containing approximately 4.9 wt% Cu: 0.39 wt% Mg (12.7 Cu:Mg ratio), 0.81 wt% Mg (6.0 Cu:Mg ratio), and 1.18 wt% Mg (4.13 Cu:Mg ratio). The 0.81 wt% alloy had the highest strengthening response compared to the other two alloys. In this alloy, Mg-Ag co-clusters dominate at the early stages of aging. In the low-Mg alloy, GP zones and θ′ needles dominated, while in the high-Mg alloy, GPB zones, Mg-Ag co-clusters, and Mg-Cu co-clusters dominated. This study clearly demonstrates the importance of the Cu:Mg ratio: a low Cu:Mg ratio favours GP zones and θ′, while a high Cu:Mg ratio favours GPB zones and S′. These results are very important for understanding the challenges inherent in the current project. The Mg in the alloy is critical to achieving peak aged strength, but it is also the most volatile element in the alloy and will be subjected to some level of vaporization loss. Controlling the process to limit the Mg vaporization will be key.

A final consideration that has been debated in the technical literature is the existence of a separate phase that acts as a nucleation aid for Ω. Mukhopadhyay has conducted a number of studies that have explored this phenomenon.[37-39] In one study, he found that Ω could nucleate on the γ′ phase (Ag_2Al) in silver-bearing Al-Cu-Mg alloys. The aging heat treatment was conducted at 250 °C, much higher than the normal aging treatment (< 200 °C). The second study showed that Ω could nucleate at manganese-bearing dispersoids (the commercial alloy 2139 has a nominal concentration of 0.4 wt% Mn). The alloy in the second study, however, had a Mn concentration of 1.45 wt%, greatly exceeding the maximum allowed Mn content in alloy 2139 (0.6 wt%). Mukhopadhyay's two studies show that changes in the standard 2139 chemistry or the accepted heat treatment can have significant effects on how the precipitate phase(s) develop. The vast majority of the studies reported in the technical literature conclude that Ω first forms on Mg-Ag(-Cu) clusters that were created at quenched-in vacancy locations. These clusters are homogeneously distributed throughout the matrix. The Mg-Ag reduces the misfit strain energy between the α/Ω interface, creating a coherent interface with very low misfit strain. This favours Ω growth in the $\{111\}_\alpha$ habit plane. In mechanically worked material (T8 temper condition), there is still a preference for the nucleation of Ω on the homogenously distributed cluster locations as opposed to on dislocation sites.

Previous work has been done on electron beam directed energy deposition of aluminium alloy 2139.[80] This work was performed using wire feedstock that was drawn from plate material with a composition within the alloy specification range. The deposition was performed at NASA Langley Research Center in Hampton, Virginia, USA, using a Sciaky Inc. electron beam additive manufacturing system. This system operates under vacuum, which can compound the preferential vaporization problem. The initial deposit made for evaluation was five beads wide by five layers tall. Figure 6.7 shows results from an aging study performed using sample material from the deposited block. Two conditions were evaluated; the unmodified baseplate

and the deposited material. Both samples showed peak hardness at approximately the same time: 18 hours at 160 °C. The deposited material, however, peaks at 131 HV versus 152 HV for the parent material. Evaluation of the deposited material chemistry showed much lower Mg content compared with the starting wire feedstock. The wire had 0.52 wt% Mg, while the bottom of the deposit had 0.19 wt% Mg and the top had 0.11 wt% Mg. Clearly, there is significant Mg vaporization in alloy 2139 in a vacuum-based electron beam directed energy additive manufacturing system.

The next step in the study was to fabricate custom wire with elevated Mg content. The target concentration was 1.6 wt% Mg. The analysed actual concentration was 1.69 wt%. A sample deposit was made using this wire, and further testing was performed to characterize the results. The analysed composition for the modified wire deposit was 0.52 wt% Mg, which was right in the middle of the specification limits. Transmission electron microscopy (TEM) showed

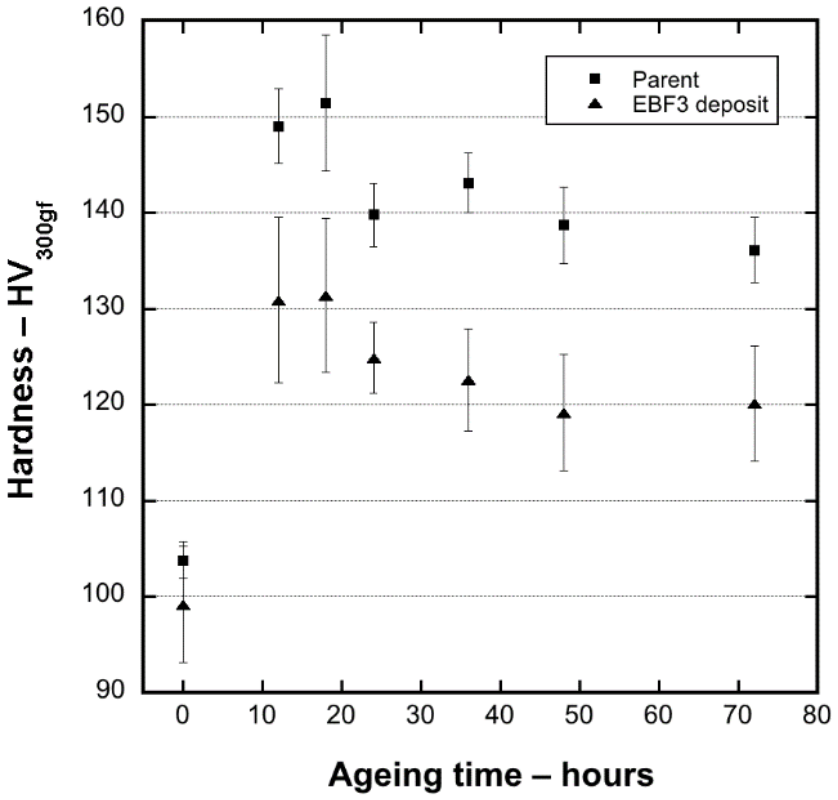

Figure 6.7: *Aging study comparing the parent Al 2139 alloy and the additively manufactured 2139 alloy (marked EBF[3] deposit) From Brice et al.[81] (used with permission).*

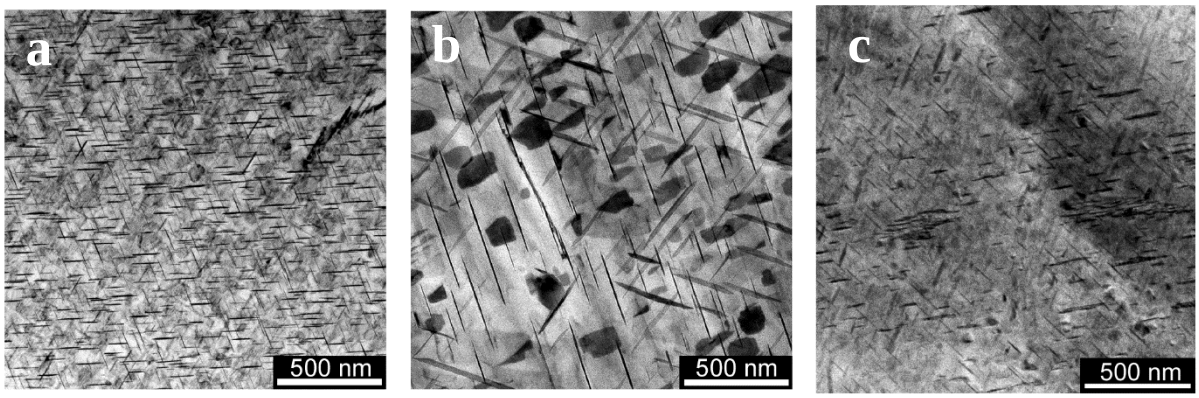

Figure 6.8: *Transmission electron micrographs of the 2139 alloy baseplate (a), deposit with standard chemistry wire (b), and deposit with elevated Mg content wire (c). All images taken near the ⟨011⟩$_\alpha$ zone axis. From Brice et al.*[81] *(used with permission).*

the effectiveness of the Mg modification to the wire. Figure 6.8a–c shows the TEM microstructure of the baseplate, the deposit made with the standard chemistry wire, and the deposit made with the elevated Mg content wire. These micrographs were taken near the ⟨011⟩$_\alpha$ zone axis such that the Ω particles are viewed edge-on. There is a clear difference between the number density and size of the precipitates in the standard chemistry wire deposit. There is also evidence of θ′ precipitates (large dark patches) that are viewed obliquely from the ⟨011⟩$_\alpha$ zone axis. Adding extra Mg back into the feedstock wire resulted in a microstructure similar to the baseplate. Microhardness testing of the modified wire deposit in the peak aged condition showed that it did not suffer any hardness debit and was equivalent to the baseplate material.

Alloy 2139 is a good candidate for additive manufacturing. The small amount of Mg in the alloy, along with small amounts of Ag, is necessary to bring about the preferred homogeneous nucleation of the Ω phase on the {111}$_\alpha$ planes, which allows peak strength to be achieved without mechanically working the material. The sensitivity of the microstructure to the Mg content presents a challenge for AM processing of alloy 2139, particularly in a vacuum environment. Careful control of the processing conditions will be necessary in the current study to tightly control the Mg concentration in the deposit and prevent widely varying properties within a given structure.

References

1. History of Aluminum. http://www.aluminum.org/aluminum-advantage/history-aluminum (accessed September 15, 2016).

2. The History of Aluminum Industry. http://www.aluminiumleader.com/history/industry_history/ (accessed September 15, 2016).

3. Hall Process: Production and Commercialization of Aluminum. https://www.acs.org/content/acs/en/education/whatischemistry/landmarks/aluminumprocess.html (accessed December 3, 2015).

4. Polmear, I., Aluminium alloys – a century of age hardening. *Materials Forum* **2004,** *28*, 1-14.

5. Wilm, A., Physical metallurgical experiments on aluminium alloys containing magnesium. *Metallurgie* **1911,** *8*, 223.

6. Wilm, A. Aluminum Alloy. U.S. Patent 1,130,785, March 9, 1915.

7. Polmear, I., Recent developments in light alloys. *Materials Transactions, JIM* **1996,** *37* (1), 12-31.

8. Sanders Jr, R. E., Technology innovation in aluminum products. *JOM* **2001,** *53* (2), 21-25.

9. Guinier, A., Structure of age-hardened aluminium-copper alloys. *Nature* **1938,** *142* (3595), 569-570.

10. Preston, G., The diffraction of x-rays by age-hardening aluminium copper alloys. *Proceedings of the Royal Society of London. Series A, Mathematical and Physical Sciences* **1938**, 526-538.

11. Hatch, J. E., *Aluminum: Properties And Physical Metallurgy*. ASM International: Metals Park, OH, 1984.

12. Davis, J. R.; Davis, J. R., *Aluminum And Aluminum Alloys*. ASM international: Metals Park, OH, 1993.

13. Benedyk, J. C., International temper designation systems for wrought aluminum alloys. *Light Metal Age* **2010**, 16.

14. Dash, M.; Makhlouf, M., Effect of key alloying elements on the feeding characteristics of aluminum–silicon casting alloys. *Journal of Light Metals* **2001,** *1* (4), 251-265.

15. Yang, Y.; Dong, P.; Zhang, J.; Tian, X., A hot-cracking mitigation technique for welding high-strength aluminum alloy. *Welding Journal* **2000,** *79* (1), 9-s.

16. Kou, S., Solidification and liquation cracking issues in welding. *JOM* **2003,** *55* (6), 37-42.

17. Totten, G. E.; MacKenzie, D. S., *Handbook of Aluminum: Vol. 1: Physical Metallurgy and Processes*. CRC Press: 2003; Vol. 1.

18. Orowan, W., Fracture and strength of solids. *Reports on Progress in Physics* **1949,** *12* (1), 185.

19. Gladman, T., Precipitation hardening in metals. *Materials Science and Technology* **1999,** *15* (1), 30-36.

20. Ostwald, W., *Analytische Chemie*. Engelmann: Leipzig, 1901.

21. Wagner, C., Theory of precipitate change by redissolution. *Z. Elektrochem* **1961,** *65* (7/8), 581-591.

22. Lifshitz, I. M.; Slyozov, V. V., The kinetics of precipitation from supersaturated solid solutions. *Journal of Physics and Chemistry of Solids* **1961,** *19* (1-2), 35-50.

23. Nie, J.; Muddle, B., Microstructural design of high-strength aluminum alloys. *Journal of Phase Equilibria* **1998,** *19* (6), 543-551.

24. Guo, Z.; Sha, W., Quantification of precipitation hardening and evolution of precipitates. *Materials Transactions* **2002,** *43* (6), 1273-1282.

25. Massalski, T., The Al− Cu (Aluminum-Copper) system. *Journal of Phase Equilibria* **1980,** *1* (1), 27-33.

26. Davis, J., ASM Handbook Volume 3–Alloy phase diagrams. *ASM International* **1992**.

27. Ringer, S. P., K. Hono, and I.J. Polmear In *Precipitate nucleation in alloys based on the Al-Cu system*, 4th International Conference on Aluminum Alloys (ICAA4), 2004; pp 574-581.

28. Taminger, K. M.; Hafley, R. A.; Domack, M. S. In *Evolution and control of 2219 aluminium microstructural features through electron beam freeform fabrication*, Materials Science Forum, Trans Tech Publ: 2006; pp 1297-1302.

29. Domack, M. S.; Taminger, K. M.; Begley, M. In *Metallurgical mechanisms controlling mechanical properties of aluminium alloy 2219 produced by electron beam freeform fabrication*, Materials Science Forum, Trans Tech Publ: 2006; pp 1291-1296.

30. Brice, C. A., Hafley, Robert A., Taminger, Karen M., Waid, Michael C., Gonzales, D., Fabrication and certification of EBF^3 aluminum components for international space station support. Presented at Materials Science & Technology 2011 Conference & Exhibition, Columbus, OH, October 18, 2011.

31. Brice, C. A., Manufacturing research at NASA for improved performance and reduced cost. Presented at New Production Technologies in the Aerospace Industry: 5th Machining Innovations Conference, Hannover, Germany, November 20, 2014.

32. Papazian, J. M., A calorimetric study of precipitation in aluminum alloy 2219. *Metallurgical Transactions A* **1981,** *12* (2), 269-280.

33. SAE, AMS 4468 Aluminum Alloy, Plate 5.0Cu - 0.4Mn - 0.5Mg - 0.4Ag (2139-T84) Soution Heat Treated, Cold Worked, and Artificially Aged.

34. Garg, A.; Chang, Y.; Howe, J., Precipitation of the Ω phase in an Al-4.0 Cu-0.5 Mg alloy. *Scripta Metallurgica et Materialia* **1990,** *24* (4), 677-680.

35. Muddle, B. C.; Polmear, I., The precipitate Ω phase in Al-Cu-Mg-Ag alloys. *Acta Metallurgica* **1989,** *37* (3), 777-789.

36. Chang, Y.; Howe, J., Composition and stability of Ω phase in an Al-Cu-Mg-Ag alloy. *Metallurgical Transactions A* **1993,** *24* (7), 1461-1470.

37. Mukhopadhyay, A.; Eggeler, G.; Skrotzki, B., Nucleation of Ω phase in an Al-Cu-Mg-Mn-Ag alloy aged at temperatures below 200° C. *Scripta Materialia* **2001,** *44* (4), 545-551.

38. Mukhopadhyay, A., Coprecipitation of Ω and σ phases in Al-Cu-Mg-Mn alloys containing Ag and Si. *Metallurgical and Materials Transactions A* **2002,** *33* (12), 3635-3648.

39. Mukhopadhyay, A., Nucleation of Ω phase in an Al–Cu–Mg alloy containing small additions of Ag. *Materials Transactions, JIM* **1997,** *38* (5), 478-482.

40. Kang, S. J.; Kim, Y.-W.; Kim, M.; Zuo, J.-M., Determination of interfacial atomic structure, misfits and energetics of Ω phase in Al–Cu–Mg–Ag alloy. *Acta Materialia* **2014,** *81*, 501-511.

41. Scott, V.; Kerry, S.; Trumper, R., Nucleation and growth of precipitates in Al–Cu–Mg–Ag alloys. *Materials Science and Technology* **1987,** *3* (10), 827-835.

42. Howe, J.; Benson, W.; Garg, A.; Chang, Y. In *In situ hot-stage high-resolution transmission electron microscopy of interface dynamics during growth and dissolution of (111) α ɵ-Al_2Cu plates in an Al-Cu-Mg-Ag alloy*, Materials Science Forum, Trans Tech Publ: 1995; pp 255-260.

43. Teleshov, V.; Kaputkin, E. Y.; Golovleva, A.; Kosmacheva, N., Temperature ranges of phase transformations and mechanical properties of alloys of the Al-Cu-Mg-Ag system with various Cu/Mg ratios. *Metal Science and Heat Treatment* **2005,** *47* (3-4), 139-144.

44. Ber, L.; Teleshov, V.; Ukolova, O., Phase composition and mechanical properties of wrought aluminum alloys of the system Al-Cu-Mg-Ag-X i. *Metal Science and Heat Treatment* **2008,** *50* (5), 220-227.

45. Auld, J., Structure of metastable precipitate in some Al–Cu–Mg–Ag alloys. *Materials Science and Technology* **1986,** *2* (8), 784-787.

46. Gable, B. M.; Shiflet, G.; Starke Jr, E., Alloy development for the enhanced stability of Ω precipitates in Al-Cu-Mg-Ag alloys. *Metallurgical and Materials Transactions A* **2006,** *37* (4), 1091-1105.

47. Garg, A.; Howe, J., Nucleation and growth of Ω phase in Al-4.0 Cu-0.5 Mg-0.5 Ag alloy—An in situ hot-stage TEM study. *Acta Metallurgica et Materialia* **1991,** *39* (8), 1925-1937.

48. Shollock, B.; Grovenor, C.; Knowlcs, K., Compositional studies of Ω and θ′ precipitates in an Al-Cu-Mg-Ag alloy. *Scripta Metallurgica et Materialia* **1990,** *24* (7), 1239-1244.

49. Wang, S.; Starink, M., Two types of S phase precipitates in Al–Cu–Mg alloys. *Acta Materialia* **2007,** *55* (3), 933-941.

50. Gouma, P.; Lloyd, D.; Mills, M., Precipitation processes in Al–Mg–Cu alloys. *Materials Science and Engineering: A* **2001,** *319*, 439-442.

51. Starink, M.; Wang, S., The thermodynamics of and strengthening due to co-clusters: general theory and application to the case of Al–Cu–Mg alloys. *Acta Materialia* **2009,** *57* (8), 2376-2389.

52. Polmear, I.; Chester, R., Abnormal age hardening in an Al-Cu-Mg alloy containing silver and lithium. *Scripta Metallurgica* **1989,** *23* (7), 1213-1217.

53. Zhou, X.; Liu, Z.; Bai, S.; Liu, M.; Ying, P., The influence of various Ag additions on the nucleation and thermal stability of Ω phase in Al–Cu–Mg alloys. *Materials Science and Engineering: A* **2013,** *564*, 186-191.

54. Bakavos, D.; Prangnell, P.; Bes, B.; Eberl, F., The effect of silver on microstructural evolution in two 2xxx series Al-alloys with a high Cu: Mg ratio during ageing to a T8 temper. *Materials Science and Engineering: A* **2008,** *491* (1), 214-223.

55. Bai, S.; Liu, Z.; Zhou, X.; Xia, P.; Liu, M., Stress-induced thickening of Ω phase in Al–Cu–Mg alloys containing various Ag additions. *Materials Science and Engineering: A* **2014,** *589*, 89-96.

56. Chang, C.-H.; Lee, S.-L.; Lin, J.-C.; Jeng, R.-R., The effect of silver content on the precipitation of the Al-4.6 Cu-0.3 Mg alloy. *Materials Transactions* **2005,** *46* (2), 236-240.

57. Bai, S.; Zhou, X.; Liu, Z.; Xia, P.; Liu, M.; Zeng, S., Effects of Ag variations on the microstructures and mechanical properties of Al–Cu–Mg alloys at elevated temperatures. *Materials Science and Engineering: A* **2014,** *611*, 69-76.

58. Min, S.; Chen, K.-H.; Huang, L.-P., Effects of Ag addition on mechanical properties and microstructures of Al-8Cu-0.5 Mg alloy. *Transactions of Nonferrous Metals Society of China* **2006,** *16* (4), 766-771.

59. Rosalie, J. M.; Bourgeois, L., Silver segregation to θ′(Al_2Cu)–Al interfaces in Al–Cu–Ag alloys. *Acta Materialia* **2012,** *60* (17), 6033-6041.

60. Dupasquier, A.; Kögel, G.; Somoza, A., Studies of light alloys by positron annihilation techniques. *Acta Materialia* **2004,** *52* (16), 4707-4726.

61. Honma, T.; Yanagita, S.; Hono, K.; Nagai, Y.; Hasegawa, M., Coincidence Doppler broadening and 3DAP study of the pre-precipitation stage of an Al–Li–Cu–Mg–Ag alloy. *Acta Materialia* **2004,** *52* (7), 1997-2003.

62. Somoza, A.; Dupasquier, A.; Polmear, I.; Folegati, P.; Ferragut, R., Positron-annihilation study of the aging kinetics of AlCu-based alloys. I. Al-Cu-Mg. *Physical Review B* **2000,** *61* (21), 14454.

63. Somoza, A.; Dupasquier, A.; Polmear, I.; Folegati, P.; Ferragut, R., Positron-annihilation study of the aging kinetics of AlCu-based alloys. II. Ag microalloying. *Physical Review B* **2000,** *61* (21), 14464.

64. Somoza, A.; Petkov, M.; Lynn, K.; Dupasquier, A., Stability of vacancies during solute clustering in Al-Cu-based alloys. *Physical Review B* **2002,** *65* (9), 094107.

65. Nagai, Y.; Murayama, M.; Tang, Z.; Nonaka, T.; Hono, K.; Hasegawa, M., Role of vacancy–solute complex in the initial rapid age hardening in an Al–Cu–Mg alloy. *Acta Materialia* **2001,** *49* (5), 913-920.

66. Zou, B.; Chen, Z.; Liu, C.; Chen, J., Vacancy–Mg complexes and their evolution in early stages of aging of Al–Mg based alloys. *Applied Surface Science* **2014,** *298*, 50-55.

67. Marceau, R.; Sha, G.; Ferragut, R.; Dupasquier, A.; Ringer, S., Solute clustering in Al–Cu–Mg alloys during the early stages of elevated temperature ageing. *Acta Materialia* **2010,** *58* (15), 4923-4939.

68. Ferragut, R.; Dupasquier, A.; Macchi, C.; Somoza, A.; Lumley, R.; Polmear, I., Vacancy–solute interactions during multiple-step ageing of an Al–Cu–Mg–Ag alloy. *Scripta Materialia* **2009,** *60* (3), 137-140.

69. Ringer, S. P. In *Advanced nanostructural analysis of aluminium alloys using atom probe tomography*, Materials Science Forum, Trans Tech Publ: 2006; pp 25-34.

70. Hono, K., Atom probe microanalysis and nanoscale microstructures in metallic materials. *Acta Materialia* **1999,** *47* (11), 3127-3145.

71. Grovenor, C.; Shollock, B.; Knowles, K., Position sensitive atom probe studies of the composition of Ω and θ'precipitates in Al-Cu-Mg-Ag alloys. *Le Journal de Physique Colloques* **1989,** *50* (C8), C8-377-C8-380.

72. Sano, N.; Hono, K.; Sakurai, T.; Hirano, K., Atom-probe analysis of Ω and θ′ phases in an Al-Cu-Mg-Ag alloy. *Scripta Metallurgica et Materialia* **1991,** *25* (2), 491-496.

73. Hono, K.; Sano, N.; Babu, S.; Okano, R.; Sakurai, T., Atom probe study of the precipitation process in Al-Cu-Mg-Ag alloys. *Acta Metallurgica et Materialia* **1993,** *41* (3), 829-838.

74. Reich, L.; Murayama, M.; Hono, K., Evolution of Ω phase in an Al–Cu–Mg–Ag alloy—a three-dimensional atom probe study. *Acta Materialia* **1998,** *46* (17), 6053-6062.

75. Reich, L.; Murayama, M.; Hono, K., 3DAP study of the effect of Mg and Ag additions on precipitation in Al-Cu (-Li) alloys. *National Research Institute for Metals* **1996,** *305*, 147-163.

76. Murayama, M.; Hono, K., Three dimensional atom probe analysis of pre-precipitate clustering in an Al-Cu-Mg-Ag alloy. *Scripta Materialia* **1998,** *38* (8), 1315-1319.

77. Rainforth, W.; Rylands, L.; Jones, H., Nano-beam analysis of Ω precipitates in a Al-Cu-Mg-Ag alloy. *Scripta Materialia* **1996,** *35* (2), 261-265.

78. Ringer, S.; Hono, K., Microstructural evolution and age hardening in aluminium alloys: atom probe field-ion microscopy and transmission electron microscopy studies. *Materials Characterization* **2000,** *44* (1), 101-131.

79. Taylor, J.; Parker, B.; Polmear, I., Precipitation in Al-Cu-Mg-Ag casting alloy. *Metal Science* **2013**.

80. Brice, C.; Shenoy, R.; Kral, M.; Buchannan, K., Precipitation behavior of aluminum alloy 2139 fabricated using additive manufacturing. *Materials Science and Engineering: A* **2015,** *648*, 9-14.

7.0 EVAPORATION, CONVECTION, AND CONDUCTION IN THE MOLTEN POOL

7.1 Molten Pool Evaporation

Evaporative loss is a fundamental aspect of most fusion-based metal additive manufacturing processes.[1] These processes are closely related to traditional fusion welding technologies, in which vapour loss has been studied for many years.[2-5] For AM, the influencing factors are the choice of heat source (in terms of power density), the processing environment (gas or vacuum), and the molten pool size and dynamics. Controlling the vapour loss in AM is important for controlling the final part properties. If the vapour loss changes throughout the build process, then the chemical composition will vary spatially within a given part. Chemical variability within a given AM part will result in inconsistent properties and limit the use of AM parts in highly critical structures.

The titanium alloy Ti-6Al-4V is subject to preferential vaporization during AM processing because Ti and Al have vastly different vapour pressures (2.46 Pa and 1,250 Pa, respectively, at 1800 °C).[6] When this alloy is processed in an electron beam directed energy deposition AM process in a vacuum environment, it has been shown that between 12 and 15% of the starting Al content is lost to vaporization.[7] Increasing the starting concentration of Al in the wire feedstock compensates for this loss such that the deposited structure has the nominal 6% Al concentration. In this particular alloy, the Al acts as a solid solution strengthener; variations of ± 0.25 wt% have some effect on properties, but the effect is tolerable.[8]

In aluminium alloy 2139, the Mg component is also subject to preferential vaporization, as its vapour pressure is significantly higher than that of Al (see Figure 7.1).[9] The vapour pressure differential is five to eight orders of magnitude in the Al-Mg system compared to two to three in the Ti-Al system; thus, the Mg loss in Al-Mg alloys should be expected to be much

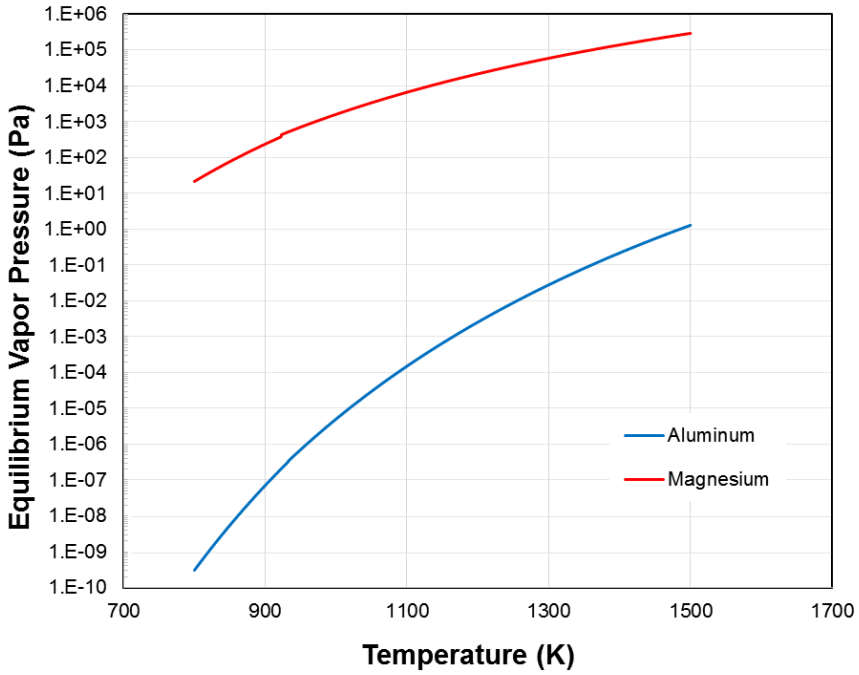

Figure 7.1: *Equilibrium vapour pressure of aluminium and magnesium over the expected temperature ranges experienced during additive manufacturing. Data from TU Wein Institute of Applied Physics.*[9]

higher than the 15% Al loss seen in the alloy Ti-6Al-4V. In addition, the strengthening contribution of Mg in Al 2139 is not strictly a solid solution mechanism. As discussed in Chapter 6, the Mg acts as a nucleating agent for the strengthening Ω phase. A critical amount of Mg is necessary to ensure the nucleation of Ω over the nucleation of precursor θ phases (i.e., GP zones, θ″). Furthermore, a variation in the Mg content, even within the allowable compositional range as dictated in the industry specification (0.2 to 0.8 wt%), will likely result in variations in mechanical properties. Bai et al. demonstrated this effect in an Al-Cu-Mg-Ag alloy by showing a peak microhardness difference of 21 VHN between a composition with 0.39 wt% Mg and one with 0.81 wt% Mg.[10] From this work it is clear that much tighter control is necessary for Al-Mg alloys processed by AM than for other alloys containing elements with differing vapour pressures.

7.2 Vapour Pressure Fundamentals

The fundamental aspects of evaporation in a vacuum environment have been well studied. The standard equation governing molar vaporization flux rate (J_i) is the Hertz–Knudsen equation given by

$$J_i = \frac{P_i^0 - P}{\sqrt{2\pi M_i RT}} \quad 7.1$$

where P_i^0 is the standard vapour pressure of the evaporating substance, P is the pressure above the condensed phase, M_i is the molecular weight, R is the universal gas constant, and T is the absolute temperature.[11] This is often termed "Langmuir vaporization" when the vaporization is occurring from a free surface. The standard vapour pressure is itself a function of temperature and can be calculated using the empirical relationship

$$log\, P_i^0 = \frac{A}{T} + B\, log\, T + CT + D \quad 7.2$$

where A, B, C, and D are experimentally determined constants. Equation 7.1 is an idealized version of the equation; it assumes the gas atoms do not interact and have a certain velocity distribution. There is significant deviation from these assumed equilibrium conditions at the immediate interface between the condensed phase and the vapour phase. This is known as the Knudsen layer and is generally considered a few atomic mean free paths in thickness.[12] In this layer, atomic collisions result in the condensation of some of the vapour atoms back into the molten pool. Safarian and Engh conducted a thorough study of the evaporation of various metals from a molten surface in a vacuum environment.[13] They concluded that an estimated 85% of the vapour atoms escape to the atmosphere and 15% are condensed back into the liquid. Separate studies by Anisimov came to similar conclusions (18 to 20% of vapour re-condenses).[14-15] Because this experiment explores AM in a vacuum environment, a modified version of eq 7.1 will be used that will account for condensation back onto the liquid surface during evaporation and assumes the pressure above the condensed phase (P) is zero:

$$J_i = \frac{\alpha_e P_i^0}{\sqrt{2\pi M_i RT}} \quad 7.3$$

The coefficient of evaporation (α_e) is the fraction of vaporizing atoms that actually escape to the vapour phase and do not re-condense back into the molten pool. The value of α_e is nominally 0.85 based on the prior work cited above.

7.3 Molten Pool Evaporation

Research into molten pool physics in the welding community has established some key concepts. The high energy density necessary to create and stabilize a molten pool can heat the material, or certain solute species within the material, beyond the boiling point.[16-18] The evaporating material induces a recoil pressure on the molten pool, creating a concave depression.[19] As the energy density increases, the recoil pressure increases to a point at which a vapour cavity is sustained inside the molten pool. This is termed "keyhole mode" (see Figure 7.2). In keyhole mode welding, the vaporized material acts to stabilize the walls of the keyhole and enables high-aspect-ratio weld joints. In AM, keyhole mode is undesirable because it has a much higher chance of creating defects, such as trapped gas porosity, due to instability in the keyhole. Conduction mode, in which the molten pool is a low-aspect-ratio hemispherical shape, is much preferred in AM, as it is less prone to defects and easier to stack in three dimensions.

The shape of the molten pool (keyhole, conduction, or in between) might have some effect on the overall vaporization rate. The Hertz Knudsen equation assumes a planar surface between the liquid and gas phases. In the case of welding or additive manufacturing, the surface has a curvature to it. Furthermore, there is a vapour plasma present and concentrated just above the impingement point where the beam hits the molten pool. This plasma plume creates a localized atmosphere and likely reduces the vaporization rate at this location. At the edges of the molten pool in conduction mode, the plasma plume is reduced (or absent) and thus the flux more closely matches the Hertz Knudsen conditions. In keyhole mode, the plasma plume interacts with more

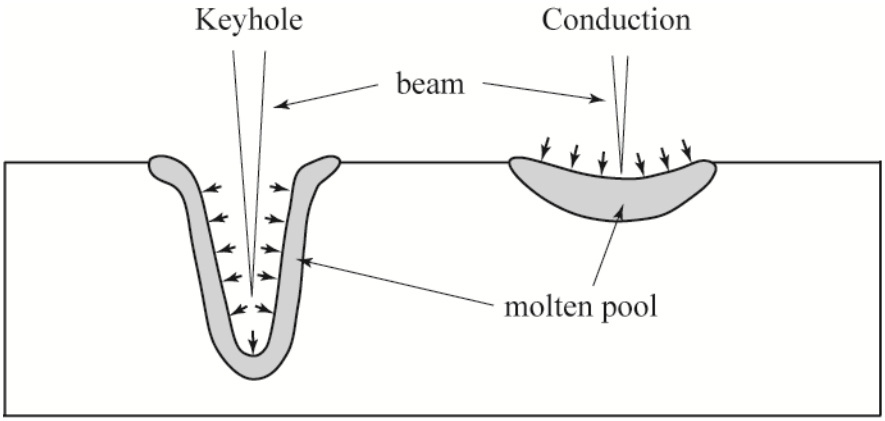

Figure 7.2: *Schematic cross section through molten pool showing the difference between keyhole mode and conduction mode. Small arrows indicate recoil pressure on the molten pool from vaporization.*

molten pool surface area and could reduce the overall vaporization rate compared to conduction mode. However, the risk of collapsed keyhole defects makes operating AM processes in pure keyhole mode undesirable. Perhaps some mode in between pure conduction and pure keyhole would provide the most advantage with regard to minimizing both vaporization loss and collapsed keyhole defects.

Schauer et al. used an infrared pyrometer to examine the temperature of the molten pool during autogenous electron beam welding.[20] This work carefully directed a spot beam infrared pyrometer into the molten pool depression cavity during welding. Measurements made on a variety of aluminium alloys showed that the molten pool temperature varies greatly from alloy to alloy. This was attributed to the evaporative cooling effect on alloys with higher content of volatile alloying elements such as magnesium. For example, the peak measured temperature in alloy 2024 (1.5 wt% Mg) was 1700 ± 100 °C, while the peak temperature in alloy 5083 (4.5 wt% Mg) was only 1250 ± 100 °C. They further demonstrated that multiple weld passes over the same region increased the molten pool temperature because volatile elements continued to evaporate with each pass. From this work it is clear that evaporative loss of volatile elements not only affects the as-deposited material composition but also affects the stability of the process. A stable molten pool could quickly become unstable because of chemically-induced

variation in vapour pressure above the pool. An unstable molten pool has a much higher probability of producing solidification defects (e.g., collapsing keyhole porosity). For additive manufacturing, process controls must be used to account for chemical variation such that the final part will have compositional consistency while also minimizing defects.

Additional work by Wei and Chow[21] using an Al-Zn alloy and by Block-Bolten and Eagar[2] and Zacharia et al.[22] using stainless steel alloys supports the conclusions by Schauer et al. in their work using stainless steel alloys. Block-Bolten and Eager also concluded that evaporative power loss effectively sets an upper limit on the molten pool temperature. Furthermore, they hypothesized that the molten pool surface temperature varies, with a maximum at the centre and a minimum at the edges. Work by Zhao and DebRoy[5], He et al.,[23] and Mundra and DebRoy[24] also calculated a strong surface temperature gradient in weld molten pools. This can cause atoms to evaporate in the centre and subsequently re-condense back into the molten pool at the edges. Because of this variation in molten pool temperature, it is difficult to determine exactly how much of the incident energy is lost to evaporative effects. Block-Bolten and Eager concluded that the energy loss is somewhere between 1 and 10%. A 10% energy loss due to evaporative cooling could very well lead to defects in the AM process because there is the possibility of having insufficient energy to fully melt the feedstock and keep the molten pool stable.

A final consideration for the vaporization of volatile elements from the molten pool is the effect of contaminants on the pool surface. Collur et al. demonstrated this effect in a study using a molten copper droplet.[3] They found that partial coverage of the surface of the drop by sulphur and oxygen contributed to a reduction in the overall vapour flux from the molten surface. The surface coverage with non-volatile species prevents the volatile species from evaporating. Contaminants in the feedstock or in the atmosphere could result in reduced vaporization loss during AM processing.

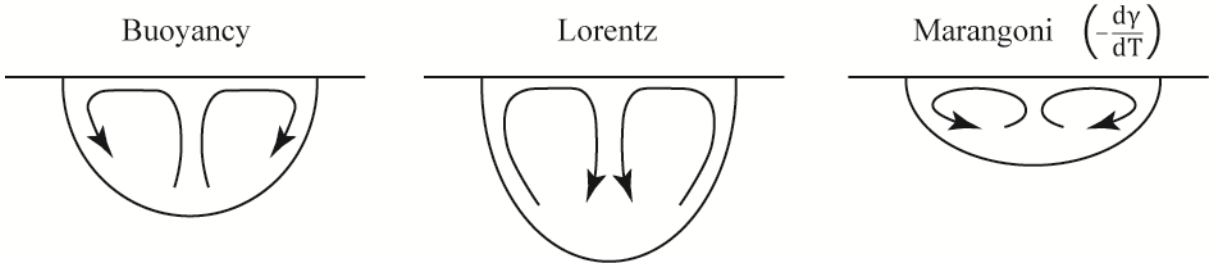

Figure 7.3: *Schematic showing convection mechanisms and the effect on fluid flow in the cross section of a molten pool. The Marangoni effect shown is for materials that show a decrease in surface tension (γ) with increasing temperature, typical for most metals.*

7.4 Molten Pool Convection

Convection in the molten pool is also a critical factor to consider in additive manufacturing processes. As with evaporation described above, there is a significant amount of relevant literature from the welding community that can be applied to AM problems. Generally, there are three main forces driving convection within a molten pool: (1) buoyancy, (2) electromagnetic (or Lorentz), and (3) surface tension (or Marangoni).[25] Figure 7.3 shows cross-sectional schematic representations of how these convective mechanisms operate in a typical molten pool. Note that the Lorentz force is only applicable for electrically-driven heat sources (e.g., arc, electron beam).

The buoyancy force is due to temperature gradients within the volume of the molten pool. The density of the liquid increases with temperature; thus, cooler areas of the molten pool sink because of gravity and establish convection currents in the pool. Generally, a heat source with a Gaussian distribution will create a molten pool that is hottest in the centre and coolest at the edges. The cooler material at the edges of the molten pool will sink, and the hotter material in the centre will rise, setting up a convective flow as shown in Figure 7.3.

Lorentz forces are due to the movement of current through the molten pool and the interaction with the induced magnetic fields. This force acts inward toward the centreline of the molten pool.[26] The current entering the part is usually highly focused, which is necessary to create and sustain a molten pool. Once the current enters the part, it quickly spreads into the

underlying material. This diverging current drives the inward force in a downward direction, setting up the current flow shown in Figure 7.3. As depicted in the graphic, the Lorentz force tends to create a deeper but more narrow molten pool, as the hottest material directly under the heat source is convectively driven downward.

Marangoni forces are due to temperature-driven differences in surface tension in the molten pool.[27] Most metals exhibit decreasing surface tension with increasing temperature. Again, as the material in the centre of the weld pool directly under the heat source is the hottest, the surface tension as that location is the lowest. The cooler material at the molten pool edges has a higher surface tension. The material with higher surface tension induces a pulling force on the material with lower surface tension (the Marangoni effect) and creates a convective flow as shown in Figure 7.3. This flow draws heat from the centre of the molten pool to the edges, resulting in a wider, shallower molten pool. Certain alloy additives or impurities can alter the surface tension and create a positive surface tension gradient, $\frac{d\gamma}{dT}$. In this case the convective flow is reversed with respect to Figure 7.3, and the molten pool becomes narrower and deeper, similar to the Lorentz effect.[28]

Various studies of the convective effects in molten pools are available in the welding literature. Choo and Szekely modelled fluid flows in arc-welded stainless steel alloy 304.[16] They showed that the flow was dominated by Marangoni convection with a peak velocity of 69.1 cm/s, compared to 6.9 cm/s for Lorentz and 0.4 cm/s for buoyancy. Similar results were documented by He et al.,[29] who showed a maximum combined flow of 76 cm/s; Oreper et al.[28] showed 60–120 cm/s; DebRoy et al.[18] showed 60 cm/s; and Kou and Wang[25] showed upwards of 300 cm/s. In these studies, the dominant convective mechanism is Marangoni flow. Given the typical molten pool dimensions in EBDED (< 1 cm) and molten dwell times (1 s), it can be estimated that the molten pool is being fully mixed 50 times or more before the material solidifies. This is a very important consideration regarding evaporative loss from the molten

pool, as it can be assumed that surface evaporation is not diffusion-limited in the liquid, and any elemental losses incurred will be evenly distributed throughout the molten pool. This assumption will be tested as part of this study.

As mentioned in Section 7.3, Langmuir vaporization acts to moderate the surface temperature of the molten pool through evaporative cooling. Similar surface cooling happens as a result of convective flows as described in the preceding paragraph. Convection draws heat away from the surface and redistributes it within the molten pool. Choo and Szekely modelled a drop in surface temperature from 2900 K to 2400 K when a combined convective flow of 60 cm/s is present.[16] The combined effects of Langmuir vaporization and convective fluid flow must be considered in modelling the peak temperature of the molten pool surface.

DebRoy and David provide one of the most comprehensive investigations of vaporization and fluid flow in welding processes.[30] They conclude that there is a great deal of complexity with competing factors that dictate evaporative loss and convection in the molten pool. Fuerschbach et al. conducted a careful experimental procedure where vapour material was captured and analysed and compared to the modelled results.[4] The agreement was very good for measuring various aspects of the molten pool in spot welds of stainless steel 304. They concluded that convection and evaporation both affect the temperature of the molten pool and that there are significant temperature gradients on the surface of the molten pool.

7.5 Thermal Conduction

Thermal conduction is a particularly important factor to consider in additive manufacturing processes. The thermal boundary conditions change constantly during an AM build. Initial layers are typically deposited onto a substrate at near-ambient temperature. This provides a good heat conduction path that is essentially three-dimensional. As additional layers are added, residual heat begins to accumulate in the substrate and the previous layers. This causes a reduction in the thermal gradient and slows the cooling rate in the molten pool. In

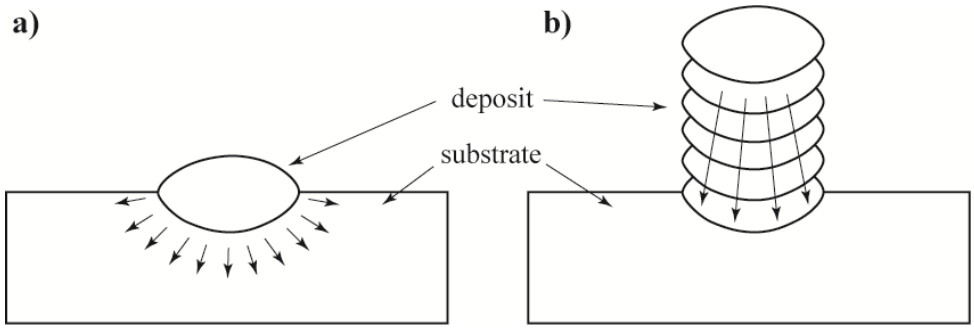

Figure 7.4: *Schematic showing cross section through deposit highlighting difference in heat flow in (a) single bead and (b) multiple stacked beads. Arrows indicate thermal path showing primarily 3D heat flow in the single bead and 2D in the multi-bead wall.*

addition, the geometry of the AM part can further reduce the thermal gradient by limiting the heat conduction path within the part to two dimensions. Figure 7.4 shows a schematic representation of this effect.

Manvatkar et al. demonstrated the effects thermal convection has on microstructure using laser-powder-deposited 316 stainless steel.[31] This experiment compared the microstructural features of each layer in a three-layer deposit. Peak temperature was highest in the third layer (2035 K), which was 89 K higher than in the first layer. This is attributable to the thermal path effects described above. Cooling rates were estimated using thermal models and predicted to be 6550 K/s in the first layer and 2780 K/s in the third. This significant difference is reflected in the measured microstructural cell spacing (31% increase from layer 1 to layer 3) and the microhardness (9% decrease from layer 1 to layer 3). The large variance across three layers is disconcerting, as most AM builds contain tens to hundreds of layers. Maintaining microstructural consistency throughout a very large AM build is challenging and requires a thorough understanding of both the transient thermal conditions and the influence these conditions have on the resulting microstructure.

Similar results were attained by the author in an electron beam wire deposition process using 2319 aluminium alloy.[32] In this study, cooling rates were estimated using an empirical relationship between the secondary dendrite arm spacing (SDAS) and the cooling rate of the

alloy. In a twenty-layer sample, the cooling rate varied from about 250 K/s at the bottom to 150 K/s at the top. Again, this shows that the microstructure in AM-deposited materials critically depends on the heat input and the thermal conduction path in the part.

7.6 Molten Pool Dynamics in Aluminium Alloys

The weldability of specific aluminium alloys is often dependent on the composition and, in particular, on the presence of highly volatile alloying elements. Woods conducted a study that used high-speed video to classify the molten metal transfer of various aluminium alloys during arc welding.[33] A clear correlation was drawn between alloys with highly volatile solute elements (e.g., Zn, Mg) and turbulence in the molten metal transfer. The higher the concentration of volatile elements, the greater the tendency for excessive spatter in the weld. Spatter is certainly undesirable in AM processes because it can lead to defects in the deposited part.

Blake and Mazumder demonstrated that vaporization in aluminium alloy 5083 (4.45 wt% Mg nominal) could be supressed using a high-pressure plasma.[34] The plasma was created with a complex shielding gas arrangement and designed to prevent vapour loss from the molten pool by reducing the pressure differential between the evaporating species and the atmosphere above the pool. This technique could provide a useful method for reducing the overall vaporization rate in AM processes, provided the process environment allows for it. In the EBDED process, which is conducted in a vacuum, this technique is not viable.

An induced plasma above the molten pool can help with vaporization loss but can also attenuate the beam, as it must propagate through the plasma. Huntington and Eagar[35] showed that this effect holds for lasers but is not significant for electron beam, the difference being the beam energy, which is approximately 0.1 eV for photons versus 100,000 eV for electrons. Little if any attenuation of the beam is expected in the EBDED AM process.

Wei and Chow demonstrated that the evaporation pressure on the molten pool due to a highly volatile element (Zn) can have a pronounced effect on the molten pool shape.[21] The evaporative cooling effect lowers the keyhole cavity surface temperature by as much as 300 K and consequently changes the depth and width of the keyhole. These effects hold for very low solute concentrations (0.1 wt% Zn). Having a highly volatile alloying component such as Zn can alter the shape of the molten pool and encourage keyhole mode. Keyhole mode is undesirable in AM because it can lead to defects. Careful attention must be paid to process settings when depositing aluminium alloys with highly volatile solutes to avoid keyhole mode.

7.7 Molten Pool Dynamics in Additive Manufacturing

Few studies have looked specifically at the molten pool dynamics in additive manufacturing processes. As described above, however, AM is very closely related to conduction-mode welding, and the modelling work from the welding community can be adapted to AM processes. Klassen et al. examined molten pool dynamics in electron beam powder bed fusion AM using titanium alloys.[36] The peak temperature of the molten pool (3225 K) comes very close to the boiling point of Ti-6Al-4V (3315 K). The convective flow velocities vary but peak at 140 cm/s. The mass loss due to vaporization is strongly a function of beam power, with higher beam power producing higher vaporization loss. These results are all in very good agreement with prior work done using welding processes and show the similarity between the two processes.

Mukherjee et al. also studied the molten pool dynamic effects in additive manufacturing.[1] They proposed a relationship between composition change (ΔX_i) due to evaporative loss and the process conditions in additive manufacturing:

$$\Delta X_i = \frac{LA_s J_i}{v} \qquad 7.4$$

In this equation, L is the bead length, A_s is the surface area of the molten pool, J_i is the flux of the evaporating species from the molten pool, and v is the process travel speed. Rearrangement in terms of flux gives

$$J_i = \frac{\Delta X_i v}{L A_s} \tag{7.5}$$

This equation gives mass flux as a function of the process parameters, the bead geometry, and the measured vaporization loss. These equations will be useful in determining Mg flux from the aluminium alloy 2139, the focus of this study.

7.8 Concluding Remarks

Extensive research has been conducted into the molten pool dynamics for a variety of alloys and a variety of welding processes. This research shows that evaporation is a significant process factor that changes the chemical composition of the alloy and produces a recoil pressure on the molten pool. Peak temperatures can approach or potentially exceed the boiling point of the alloy, driving evaporative losses higher; however, there is an evaporative cooling effect along with convective fluid flow that helps to limit the peak temperature at the molten pool surface. The convective flow, dominated by the Marangoni or surface tension gradient, is typically in the tens-of-centimetres-per-second range, ensuring that the molten pool is very thoroughly mixed. These concepts can be directly applied to AM processes that operate in the same power and mass flow regimes as their related welding processes. The layered nature of AM parts introduces a complexity not seen in most welds, namely the changing thermal conduction path and boundary thermal conditions as the deposition process progresses. These factors can have a significant impact on microstructure and properties in the as-deposited material. All of these factors must be considered to ensure that an AM-deposited structure has uniform chemistry, microstructure, and properties.

References

1. Mukherjee, T.; Zuback, J.; De, A.; DebRoy, T., Printability of alloys for additive manufacturing. *Scientific reports* **2016,** *6*.

2. Block-Bolten, A.; Eagar, T., Metal vaporization from weld pools. *Metallurgical Transactions B* **1984,** *15* (3), 461-469.

3. Collur, M.; Paul, A.; DebRoy, T., Mechanism of alloying element vaporization during laser welding. *Metallurgical Transactions B* **1987,** *18* (4), 733-740.

4. Fuerschbach, P. W.; Norris, J. T.; He, X.; DebRoy, T., Understanding Metal Vaporization from Laser Welding. Sandia National Laboratory: Albuquerque, NM, 2003.

5. Zhao, H.; DebRoy, T., Weld metal composition change during conduction mode laser welding of aluminum alloy 5182. *Metallurgical and Materials Transactions B* **2001,** *32* (1), 163-172.

6. Alcock, C.; Itkin, V.; Horrigan, M., Vapour pressure equations for the metallic elements: 298–2500K. *Canadian Metallurgical Quarterly* **1984,** *23* (3), 309-313.

7. Brice, C. A.; Rosenberger, B. T.; Sankaran, S. N.; Taminger, K. M.; Woods, B.; Nasserrafi, R. In *Chemistry control in electron beam deposited titanium alloys*, Materials Science Forum, Trans Tech Publ: 2009; pp 155-158.

8. Welsch, G.; Boyer, R.; Collings, E., *Materials properties handbook: titanium alloys*. ASM international: 1993.

9. Vapor Pressure Calculator. https://www.iap.tuwien.ac.at/www/surface/vapor_pressure (accessed July 17, 2017).

10. Bai, S.; Liu, Z.; Zhou, X.; Xia, P.; Zeng, S., Mg-controlled formation of Mg–Ag co-clusters in initial aged Al–Cu–Mg–Ag alloys. *Journal of Alloys and Compounds* **2014,** *602*, 193-198.

11. Dushman, S.; Lafferty, J. M., *Scientific foundations of vacuum technique*. 2nd ed.; Wiley: New York, 1962.

12. Kelly, R.; Dreyfus, R., On the effect of Knudsen-layer formation on studies of vaporization, sputtering, and desorption. *Surface Science* **1988,** *198* (1), 263-276.

13. Safarian, J.; Engh, T. A., Vacuum evaporation of pure metals. *Metallurgical and Materials Transactions A* **2013,** *44* (2), 747-753.

14. Anisimov, S., Vaporization of metal absorbing laser radiation. *Soviet Journal of Experimental and Theoretical Physics* **1968,** *27*, 182.

15. Anisimov, S.; Rakhmatulina, A. K., The dynamics of the expansion of a vapor when evaporated into a vacuum. *Soviet Journal of Experimental and Theoretical Physics* **1973,** *37*, 441.

16. Choo, R.; Szekely, J., Vaporization kinetics and surface temperature in a mutually coupled spot gas tungsten arc weld and weld pool. *Welding Journal* **1992,** *71* (3), 77s-93s.

17. Khan, P.; DebRoy, T., Alloying element vaporization and weld pool temperature during laser welding of AlSl 202 stainless steel. *Metallurgical Transactions B* **1984,** *15* (4), 641-644.

18. DebRoy, T.; Basu, S.; Mundra, K., Probing laser induced metal vaporization by gas dynamics and liquid pool transport phenomena. *Journal of Applied Physics* **1991,** *70* (3), 1313-1319.

19. Metzbower, E., Keyhole formation. *Metallurgical Transactions B* **1993,** *24* (5), 875-880.

20. Schauer, D.; Giedt, W.; Shintaku, S., Electron beam welding cavity temperature distributions in pure metals and alloys. *Welding Journal* **1978,** *57* (5), 127s-133s.

21. Wei, P.; Chow, Y., Beam focusing characteristics and alloying element effects on high-intensity electron beam welding. *Metallurgical Transactions B* **1992,** *23* (1), 81-90.

22. Zacharia, T.; David, S.; Vitek, J., Effect of evaporation and temperature-dependent material properties on weld pool development. *Metallurgical Transactions B* **1991,** *22* (2), 233-241.

23. He, X.; DebRoy, T.; Fuerschbach, P., Probing temperature during laser spot welding from vapor composition and modeling. *Journal of Applied Physics* **2003,** *94* (10), 6949-6958.

24. Mundra, K.; DebRoy, T., Calculation of weld metal composition change in high-power conduction mode carbon dioxide laser-welded stainless steels. *Metallurgical Transactions B* **1993,** *24* (1), 145-155.

25. Kou, S.; Wang, Y., Weld pool convection and its effect. *Welding Journal* **1986,** *65* (3), 63s-70s.

26. Nemchinsky, V. A., The distribution of the electromagnetic force in a welding pool. *Journal of Physics D: Applied Physics* **1996,** *29* (10), 2659.

27. Mills, K.; Keene, B.; Brooks, R.; Shirali, A., Marangoni effects in welding. *Philosophical Transactions-Royal Society of London Series A Mathematical Physical and Engineering Sciences* **1998**, 911-926.

28. Oreper, G.; Eagar, T.; Szekely, J., Convection in arc weld pools. *Welding Journal* **1983,** *62* (11), 307s-312s.

29. He, X.; DebRoy, T.; Fuerschbach, P., Alloying element vaporization during laser spot welding of stainless steel. *Journal of Physics D: Applied Physics* **2003,** *36* (23), 3079.

30. DebRoy, T.; David, S., Physical processes in fusion welding. *Reviews of Modern Physics* **1995,** *67* (1), 85.

31. Manvatkar, V.; De, A.; DebRoy, T., Heat transfer and material flow during laser assisted multi-layer additive manufacturing. *Journal of Applied Physics* **2014,** *116* (12), 124905.

32. Brice, C. A.; Dennis, N., Cooling rate determination in additively manufactured aluminum alloy 2219. *Metallurgical and Materials Transactions A* **2015,** *46* (5), 2304-2308.

33. Woods, R., Metal transfer in aluminum alloys. *Welding Journal* **1980,** *59* (2), 59s-66s.

34. Blake, A.; Mazumder, J., Control of magnesium loss during laser welding of Al-5083 using a plasma suppression technique. *Journal of engineering for industry* **1985,** *107* (3), 275-280.

35. Huntington, C.; Eagar, T., Laser welding of aluminum and aluminum alloys. *Welding Journal* **1983,** *62* (4), 105s-107s.

36. Klassen, A.; Scharowsky, T.; Körner, C., Evaporation model for beam based additive manufacturing using free surface lattice Boltzmann methods. *Journal of Physics D: Applied Physics* **2014,** *47* (27), 275303.

8.0 MOLTEN POOL MIXING

8.1 Background

The initial experiment in this study is designed to test the hypothesis that there is no magnesium concentration gradient in the deposited bead and the make sure that the equation to calculate the vaporisation flux (Chapter 10) is based on a correct assumption. Vaporization flux occurs only at the molten pool surface, and the flux rate could be limited by the ability of the vaporizing species to diffuse through the liquid to the surface. This experiment is critical for determining how to handle the vaporization flux calculations in Chapter 10. If a concentration gradient exists, it will have to be factored into the equation that calculates the vaporization flux from the molten pool. If there is no concentration gradient, then it can be assumed that liquid phase diffusion of the evaporating species does not limit the vaporization flux from the surface of the molten pool.

Numerous scientific studies in the field of welding have shown that convective flows within the molten pool are very high—on the order of 50 to 100 cm/s.[1-4] The specific flow path in the molten pool is dependent on the convection mechanisms present (see Chapter 7, Section 7.4). The fluid flow path is unimportant; only the magnitude of the flow velocity needs to be measured. If velocities reported in the welding literature are accurate, then it can be assumed that there is complete and uniform mixing in the molten pool. For example, imagine a molten pool on the order of 1.0 cm in diameter and 0.5 cm deep with a molten dwell time of approximately one second. These are reasonable approximations for the current experiment. In this scenario, a convective flow of between 50 and 100 cm/s will recirculate the molten material 30 to 60 times before it is fully solidified (assuming flow patterns as shown in Figure 7.3). With

this high degree of convection, it can be assumed that the liquid is fully mixed and diffusion in the liquid is not a limiting factor with regard to vaporization loss of solute atoms.

This experiment deposited a single bead of Al 5356 wire with 5.0 wt% nominal Mg onto an Al 1100 baseplate with no Mg. Electron microprobe analysis was used to quantify the local Mg concentration on multiple cross-sectional planes and determine if there was any Mg concentration gradients. The wire had high Mg content and the baseplate had no Mg content; if there was no discernible concentration gradient within the molten pool, then it can be assumed that the mixing was uniform and complete.

8.2 Experimental Method and Materials

A single-bead deposit was analysed to determine if there were any magnesium concentration gradients within the deposited bead. Aluminium alloy 5356 wire was used for the single-bead trial, as it has a high nominal Mg concentration (5.0 wt%) and provides a larger compositional range for analysis. The wire was standard weld filler wire manufactured by Hobart Brothers Company, Troy, Ohio, USA, with a diameter of 0.16 cm and a measured Mg

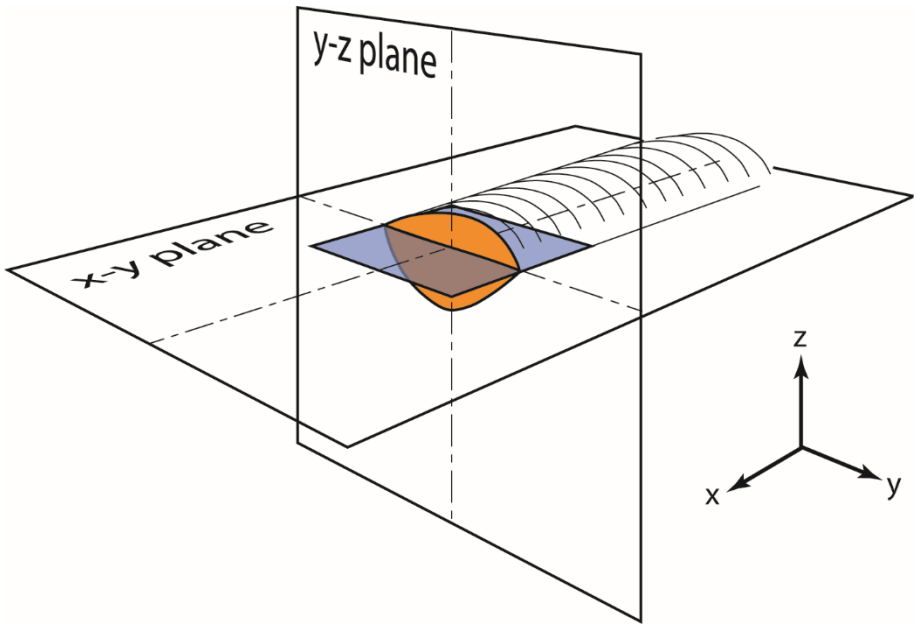

Figure 8.1: *Schematic showing x-y and y-z plane sections though a single-bead deposit for measuring magnesium concentration in the molten pool.*

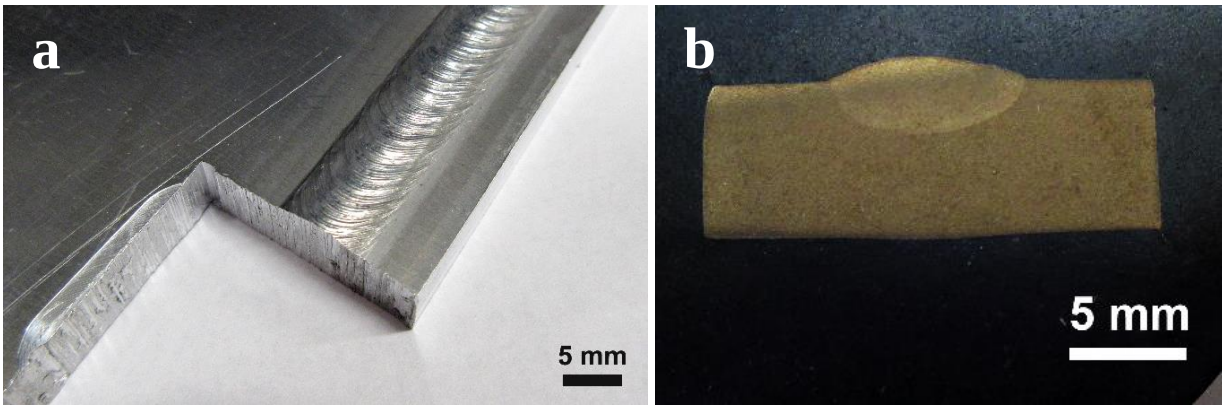

Figure 8.2: *Cross section through single-bead deposit (a) and mounted, polished, and etched sample (b) showing molten pool boundary.*

composition of 5.15 wt%. The deposit was made on an aluminium alloy 1100 plate sourced from McMaster Carr, Atlanta, Georgia, USA, with dimensions 30.5 cm × 30.5 cm × 0.64 cm. The single-bead deposit was sectioned on two planes, as shown in Figure 8.1. The Y-Z plane represents the cross section normal to the direction of travel, and the X-Y plane represents the cross section parallel to the deposited layer. A photograph of the single-bead deposit is shown in Figure 8.2a along with a mounted cross section (Y-Z plane) showing the transverse bead profile in Figure 8.2b.

The deposited bead was sent to McCrone Associates, Inc., Westmont, Illinois, USA, for wavelength dispersive spectroscopic analysis using a JEOL 8200 electron probe microanalyzer. Suitable reference materials were used to calibrate the system both before and after the experimental samples were analysed. Two linear traces were made in the Y-Z plane specimen about 1.5 mm apart. The spacing between measurements was about 0.090 mm such that 35 individual measurements were made. For the X-Y specimen, the linear traces were about 5.0 mm apart. The spacing between measurements was 0.180 mm such that 45 individual measurements were made. Each scan was done using 20 keV accelerating voltage, 50 nA probe current, and 10 μm beam diameter.

8.3 Results and Discussion

Electron microprobe analysis results are shown in Figure 8.3 for the X-Y plane and Figure 8.4 for the Y-Z plane. There is considerable scatter in the data but no definite concentration gradient. The average concentration is about 0.3 wt% Mg with an experimental error of less than 2% of the measured value. Measuring the cross-sectional area of the deposited bead crown (material above the baseplate surface) and comparing it as a fraction of the entire molten pool allows calculation of relative fractions of melted wire and melted baseplate. Using the macrograph in Figure 8.2b, it is estimated that the deposited bead comprises 29% wire and 71% melted baseplate. The wire has a Mg concentration of 5.15 wt%, and the plate has no measured Mg in it. The expected Mg concentration in the molten pool (X_{Mg}^{pool}) is calculated by multiplying the concentration of Mg in the wire (X_{Mg}^{wire}) by the fraction of the deposited bead attributable to the wire (f_{Mg}^{wire}): $X_{Mg}^{pool} = X_{Mg}^{wire} \times f_{Mg}^{wire}$. The expected X_{Mg}^{pool} is 1.5 wt% (5.15 wt% × 0.29); however, the average analysed Mg content is only 0.3 wt%. Thus, approximately 80% of the Mg present in the feedstock wire vaporized from the molten pool. While there was a very high rate of vaporization from the molten pool, there was no identifiable Mg concentration gradient measured in the fusion zone material. Furthermore, the Mg from the wire was fully mixed within the deposited bead. This data supports the assumption that a high rate of convective mixing is present in the molten pool. From this it can be assumed that liquid phase diffusion of the vaporizing species does not limit the vapour flux from the molten pool.

Figure 8.5 shows an optical micrograph from the deposited bead. The scatter seen in the microprobe data can be attributed to the second phase present in the microstructure. The measured Mg content will vary slightly based on the relative concentration of matrix and second phase in the sampling volume.

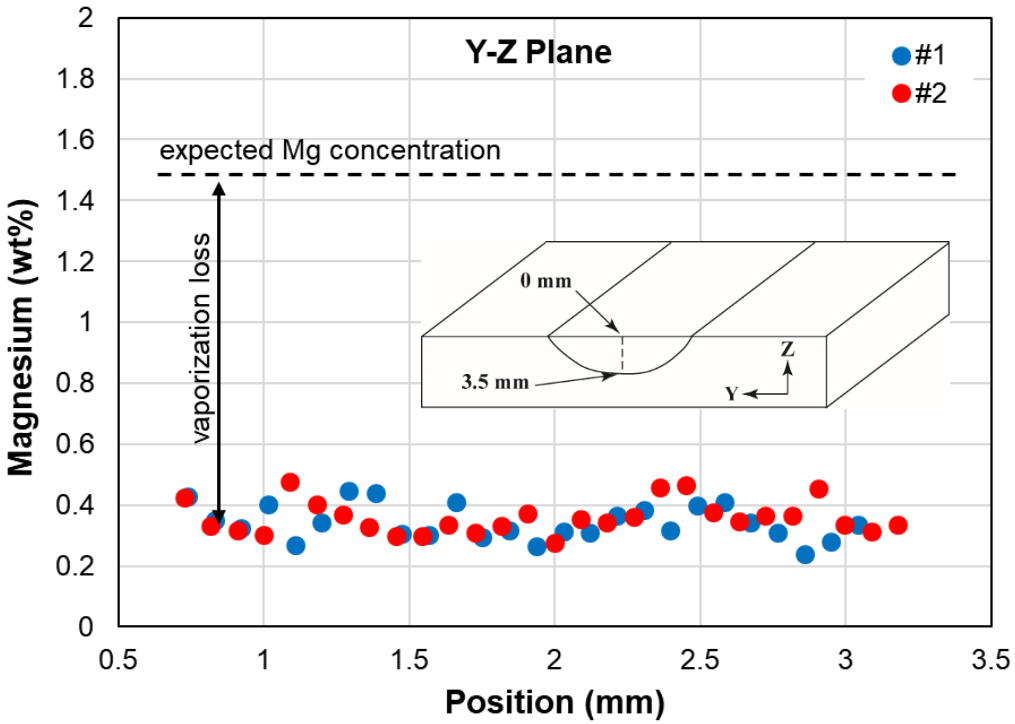

Figure 8.3: *Electron microprobe analysis of Mg concentration across the X-Y plane of the single bead deposit. Two parallel traces are shown in separate colours for each analysed plane. Zero position represents the left side deposited bead/substrate plate interface and the 6 mm position represents the right side deposited bead/substrate plate interface (see inset).*

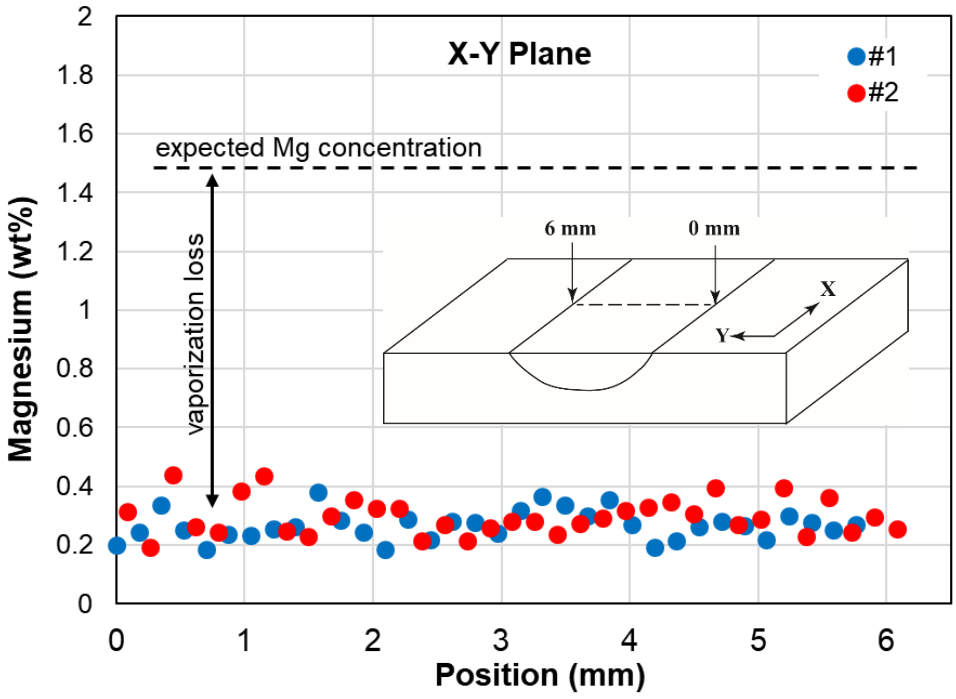

Figure 8.4: *Electron microprobe analysis of Mg concentration across the Y-Z plane of the single bead deposit. Two parallel traces are shown in separate colours for each analysed plane. Zero position represents the top of the deposited bead and the 3.25 mm position represents the deposit/baseplate interface (see inset).*

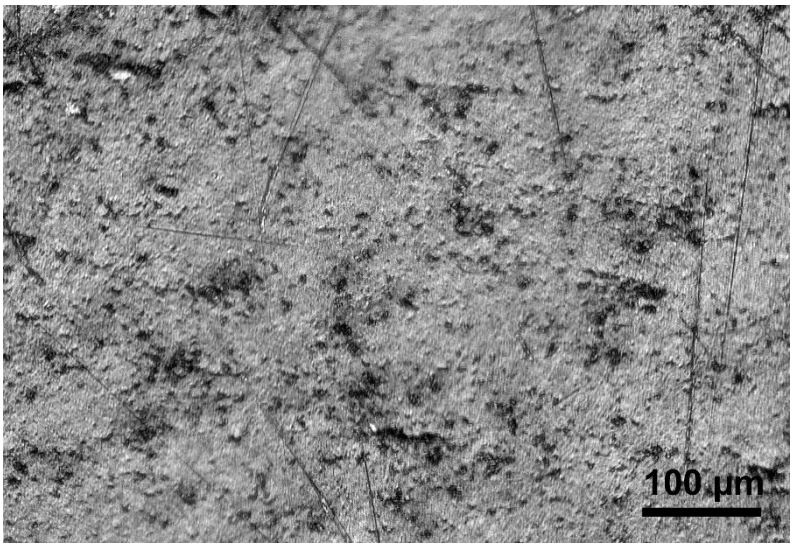

Figure 8.5: *Micrograph of deposited bead showing the phases present.*

The metallographic cross section~~s~~ shown in Figure 8.2b was used to measure the transverse molten pool size. The molten pool is assumed to be circular (supporting details and actual measurements are provided in Chapter 9). The measured transverse molten pool width was approximately 0.8 cm. The translation speed of the EBDED process was 0.85 cm/s for this experiment~~s~~. Thus, at the surface of the plate, any single location is molten for approximately one second as the beam translates over that point. As the molten pool is lenticular in shape, this dwell time will vary with depth but is generally greater than 0.5 second. From the welding literature previously discussed, the convection rate in the molten pool is assumed to be in the 50 cm/s to 100 cm/s range. The measured outer circumference of the molten pool from the taken from the transverse cross section is about 1.7 cm. Under these conditions, any location along the perimeter of the molten pool could fully circulate within the molten pool anywhere from 30 to 60 times prior to solidification.

The surface tension of aluminium as a function of temperature has a negative slope, i.e. the surface tension decreases as the temperature increases.[5] As discussed in Chapter 7, Section 7.4, surface tension-driven convection (i.e. Marangoni forces) dominate molten pool convection. Under these conditions, two oscillating convective loops are established in the

molten pool (Figure 7.2). This flow path is only half that of the full molten pool as described above – 0.85 cm instead of 1.7 cm effectively doubling the mixing rate from 30-60 time to 60 to 120 times prior to solidification.

8.4 Summary and Conclusions

Convective flow modelling studies in the welding literature predict molten pool mixing velocities of between 50 and 100 cm/s. The conditions of this experiment and the surface tension properties of the alloy predict full recirculation of the molten pool 60 to 120 times prior to solidification at any given location along the length of the bead. Under these conditions, it is expected that the alloying content in the molten pool is fully and completely mixed and does not provide a limiting factor in vaporization flux from the molten pool surface. The experiment confirmed these expectations. The Mg that was only present in the wire and not the baseplate was fully mixed within the molten pool and there was no evidence of local Mg concentration gradients. Furthermore, a significant amount of vaporization occurred (80% of total Mg content) and still the Mg content was uniform throughout the bead. In further experiments in this study it can be assumed that vaporization flux of Mg is not limited by liquid phase diffusion of Mg to the molten pool surface.

References

1. Choo, R.; Szekely, J., Vaporization kinetics and surface temperature in a mutually coupled spot gas tungsten arc weld and weld pool. *Welding Journal* **1992,** *71* (3), 77s-93s.

2. Collur, M.; Paul, A.; DebRoy, T., Mechanism of alloying element vaporization during laser welding. *Metallurgical Transactions B* **1987,** *18* (4), 733-740.

3. DebRoy, T.; Basu, S.; Mundra, K., Probing laser induced metal vaporization by gas dynamics and liquid pool transport phenomena. *Journal of Applied Physics* **1991,** *70* (3), 1313-1319.

4. He, X.; DebRoy, T.; Fuerschbach, P., Alloying element vaporization during laser spot welding of stainless steel. *Journal of Physics D: Applied Physics* **2003,** *36* (23), 3079.

5. Hatch, J. E.; Association, A.; Metals, A. S., *Aluminum: Properties and Physical Metallurgy*. American Society for Metals: 1984.

9.0 EFFECTS OF MAGNESIUM CONCENTRATION AND BASEPLATE TEMPERATURE IN SINGLE-BEAD DEPOSITS

9.1 Introduction

The overall goal of this project is to evaluate vaporization-induced chemical changes in a magnesium-bearing aluminium alloy processed using additive manufacturing. The chosen alloy is aluminium 2139, a high-strength Al-Cu alloy with minor additions of Mg and Ag (see Table 6.3 for composition limits). Of particular interest are the process-induced changes in Mg content (due mainly to evaporative loss) and what effect those changes have on microstructure and properties. By simulating the transient thermal effects of the AM process using single-bead deposits, the vapour loss of Mg over the span of an entire build sequence can be predicted. The resulting Mg concentration will have a distinct effect on the microstructure in the deposited material. This experiment quantifies these microstructure and property variations for deposits made with alloy 2139.

Various methods were used to evaluate the microstructure of the deposited beads. Optical and scanning electron microscopy (SEM) was used to evaluate the grain size and orientation. Energy dispersive spectroscopy (EDS) was used in conjunction with SEM to evaluate the composition of large intermetallic phases present in the deposited beads. Transmission electron microscopy (TEM) was used to visualize the shape of the precipitates and determine their habit plane in the aluminium matrix. Small angle neutron scattering (SANS) was used to quantify the

Table 9.1: *Target chemical composition of experimental 2139 aluminium-based alloys (in weight percent). Wire and plate Mg values were experimentally measured.*

	Cu	Mg			Ag	Mn	Al
		Target	Wire	Plate			
Alloy 1	5.00	0.20	0.037	0.19	0.35	0.40	balance
Alloy 2	5.00	0.50	0.038	0.44	0.35	0.40	balance
Alloy 3	5.00	0.80	0.67	0.71	0.35	0.40	balance

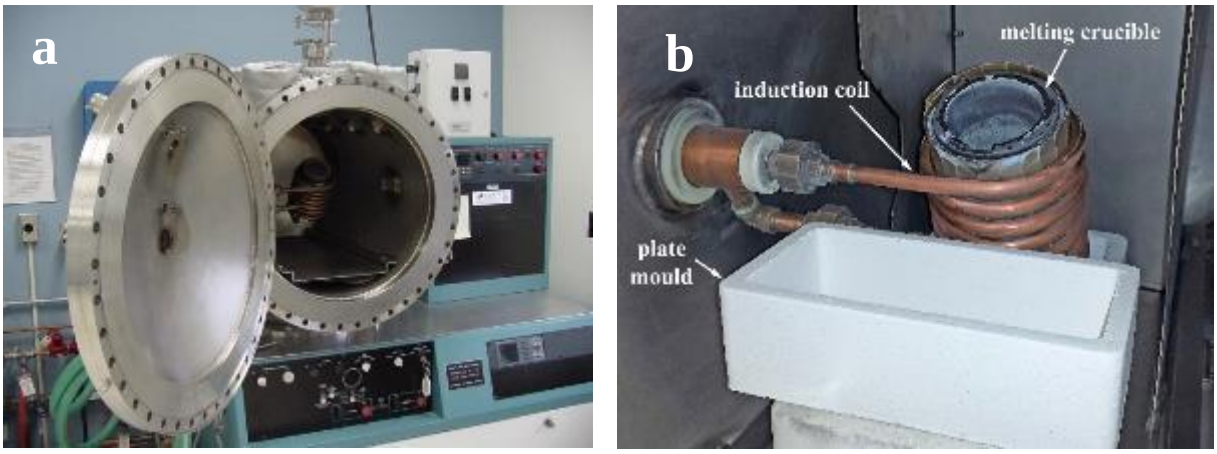

Figure 9.1: *Photograph of the induction melting furnace at NASA Langley Research Center (a) and a close-up of the interior showing the induction coil, melting crucible, and plate mould (b). Courtesy J.A. Newman, NASA Langley Research Center.*

diameter and thickness of the precipitate phases as well as qualitatively confirm the phases present in each sample. This method captures the precipitate statistics better than TEM as it is able to sample a much large volume of material. Finally, differential scanning calorimetry (DSC) was used to determine phase transformation reactions in each of the samples. Altogether, the data presents a complete picture of the phases present in each of the deposited beads that were examined.

9.2 Experimental Method and Materials

9.2.1 Wire and Baseplate Fabrication

Three separate alloy heats were created with the chemical compositions shown in Table 9.1. The alloys were chosen to span the Mg compositional limits of the alloy 2139 (0.2 wt% lower limit, 0.5 wt% nominal, 0.8 wt% upper limit).[1] The copper, silver, and manganese levels were held constant across the three alloy compositions such that the only variable was the effect of Mg concentration. Also shown in Table 9.1 is the as-measured Mg composition of both the wire and plate. The target Mg was close in the plate material but was considerably low in the 0.2 and 0.5 wt% Mg wire material. This was likely due to a processing anomaly and will be discussed at length in Chapter 10.

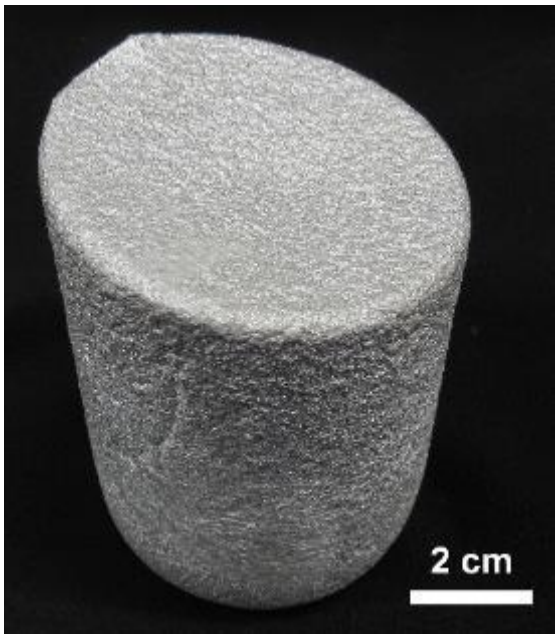

Figure 9.2: *Photograph of the as-cast ingot prior to extrusion.*

The alloy material was created by engineers and technicians in the Light Alloy Laboratory at NASA Langley Research Center, Hampton, Virginia, USA, using a laboratory-scale induction melting furnace made by Centorr Vacuum Industries, Nashua, New Hampshire, USA. Figure 9.1 shows an overall view of the furnace and a view inside the furnace that highlights the induction coil, melting crucible, and the tilt capability. Master alloy ingots (99.7%Al, Al-50%Cu, Al-25%Mg, Al-25%Mn) from Millward Alloys Inc., Lockport, New York, USA, along with 99.98% pure Ag shot from Alfa Aesar, Haverhill, Massachusetts, USA, were used to achieve the desired composition. The master alloys, provided in waffle ingot form, were sectioned into appropriately sized pieces and charged into a cylindrical graphite clay melting crucible with an overall target weight of 1.0–1.2 kg. The furnace was evacuated to 1.33×10^{-4} Pa and then backfilled to 71.1 kPa with laboratory-grade argon supplied by Arc3 Gases, Hampton, Virginia, USA. The master alloy charge was heated to just above the liquidus temperature of 916 K and held for a minimum of 2 min to allow for convective mixing, which was apparent by visual inspection through the furnace sight glass. The alloy was allowed to cool in the crucible to room temperature before it was extracted from the crucible. Figure 9.2

shows a photograph of one of the as-cast ingots. The final dimensions were approximately 6.7 cm in diameter and 9.5 cm in height.

In preparation for extrusion, the ingots were hot pressed at 748 K into a cylindrical mould 7.6 cm in diameter, which was necessary to close up any casting porosity and to shape the ingots to the appropriate size for the extrusion chamber. The hot pressing operation created mushroom-shaped flashing at the top of the ingot that was removed by lathe turning prior to extrusion. The ingots were finally machined to specifications provided by the extrusion facility such that the castings would fit within the charge chamber of the extrusion press.

Hot extrusion was performed at the Air Force Research Laboratory, Dayton, Ohio, USA, using a 6000 kN Lombard horizontal extrusion press. Each ingot was single-pass extruded at 670 K with a reduction ratio of 64:1, creating a 0.95 cm diameter rod. Each rod was cut into two 245 cm lengths and shipped to the wire drawing facility.

The wire drawing was conducted at Indalco Alloys, Inc., Mississauga, Ontario, Canada. The as-received rods were annealed at 608 K for 2 h prior to drawing. Each rod was drawn using standard wire drawing practices to a final wire diameter of 0.16 cm. The wire was cleaned and level wound onto standard plastic 30 cm diameter welding spools.

An identical melting process was followed for creating the matched composition baseplates used in the experiment. Three additional castings were made using the same compositions shown in Table 9.1. After melting the alloy charge and allowing it to fully mix, the melting crucible was tilt-poured within the induction furnace into a rectangular alumina mould (225 mm × 100 mm × 60 mm) and allowed to cool. Figure 9.1b shows the plate casting configuration.

The plate castings were post-processed to homogenize the microstructure and reduce as-cast porosity. Each cast plate was stacked between two 1.27 cm thick stainless steel plates along with a 25 μm interface layer of molybdenum foil between the aluminium casting and the steel

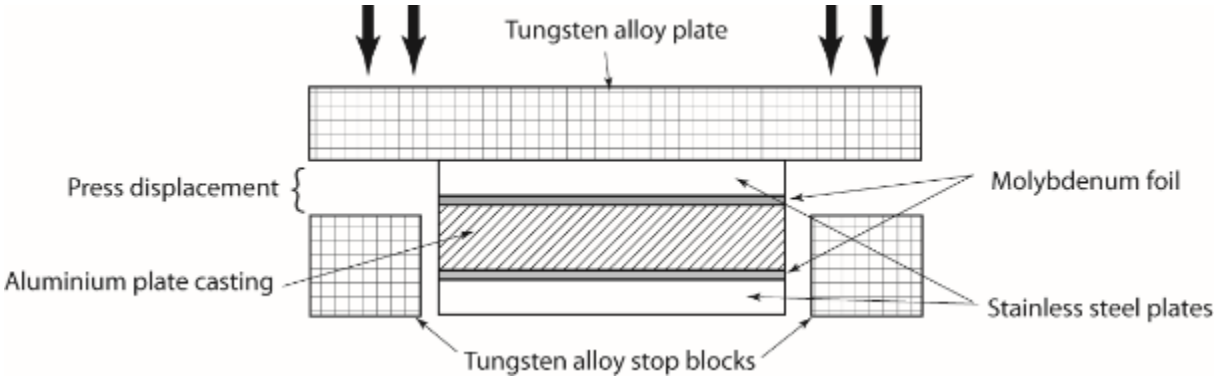

Figure 9.3: *Schematic cross-section of vacuum hot press operation for plate castings.*

plate. Four 2.54 cm tall blocks of tungsten alloy were placed outside the four corners of the stack to act as stops for the hot pressing operation. These blocks ensured that the cast aluminium plate was not pressed any thinner than 1.27 cm. Finally, a 2.54 cm thick tungsten alloy plate was placed on top of the stack to help uniformly distribute the load. Two thermocouples were placed near the cast plate to monitor the temperature profile throughout the hot pressing operation. Figure 9.3 shows a schematic representation of the vacuum hot pressing setup.

Hot pressing was done under vacuum at a temperature of 748 K. Once the target temperature was reached, force was applied at a ramp rate of 89 kN/min until a target force of 1157 kN was reached. After contact with the tungsten stop blocks, the stack was unloaded and the heat turned off. The material was allowed to cool overnight before removal. The hot pressed plates were then surface milled, which removed approximately 0.5 mm of material and left a

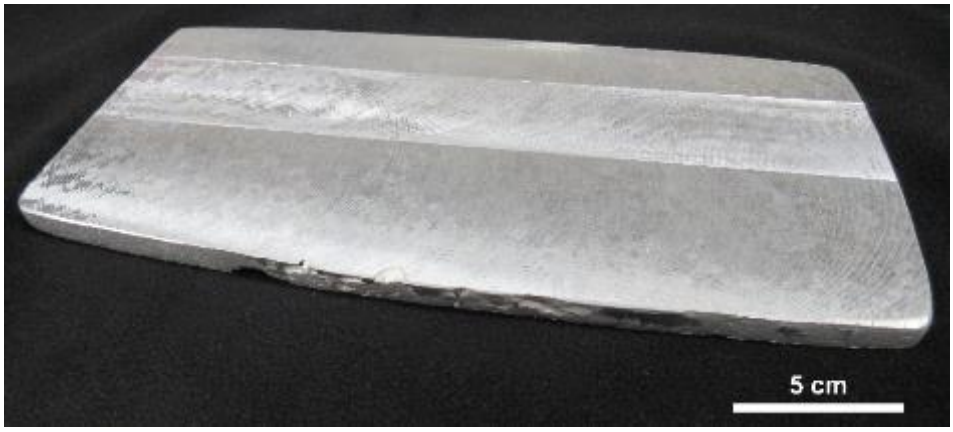

Figure 9.4: *Photograph of processed plate casting after hot pressing and skim milling of the surface.*

clean, flat surface. Figure 9.4 shows a photograph of one of the finished plates produced from a flat casting.

9.2.2 Single-Bead Deposition

The experimental test matrix consisted of a total of nine samples, as shown in Table 9.2. For each composition, single-bead trials were conducted at three different temperatures. The "ambient" trials simulated first-layer deposition when the baseplate is at ambient temperature and the molten pool is the smallest. The trials at higher temperatures simulated scenarios later in the deposition sequence when the previous layers have accumulated and retained residual heat and the molten pool is assumed to be larger.

Three rectangular blocks 10 cm long by 2.5 cm wide were cut from each of the processed plates using a band saw. Two of the three blocks from each composition had a single hole drilled and tapped on the long transverse side to provide an attachment point for a type K thermocouple. The third specimen was deposited at ambient temperature and did not require thermocouple measurement.

The three samples from each composition were clamped to a 30 cm × 30 cm aluminium plate. Run-on and run-off tabs were cut from 1100 aluminium bar stock and clamped before and after the experimental baseplate. This ensured that the experimental plate was deposited under steady-state conditions while the start/stop sequences took place in the run-on/off tabs. The experimental baseplate material was elevated off the aluminium tooling plate using two small lengths of 0.16 cm diameter wire. This limited thermal conduction into the tooling and helped achieve and maintain the proper experimental temperature for each baseplate run. The

Table 9.2: *Experimental test matrix. Composition in wt%.*

	0.2% Mg	**0.5% Mg**	**0.8% Mg**
Ambient	2L	5L	8L
348 K	2M	5M	8M
423 K	2H	5H	8H

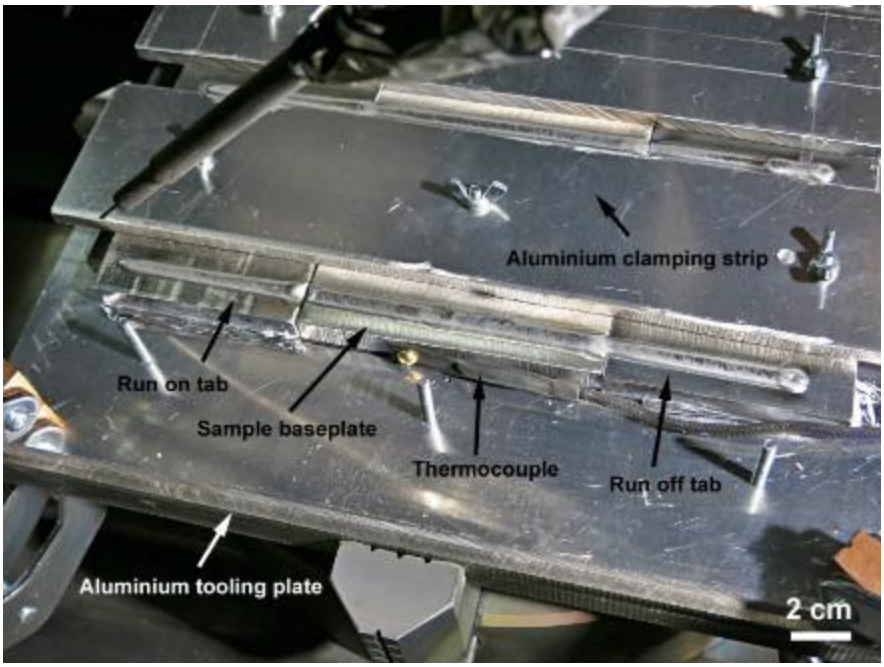

Figure 9.5: *Photograph of experimental setup. One clamping strip has been removed to show detail of the setup.*

run-on/off tabs were shimmed to the proper height using aluminium foil and all three pieces of material (run-on tab, experimental baseplate, run-off tab) were clamped to the tooling plate using aluminium clamping strips. A photograph of the experimental setup is shown in Figure 9.5.

The single-bead deposition experiments were performed on a Sciaky EBAM 110 system at Lockheed Martin Space, Littleton, Colorado, USA. The three samples from each composition were fixtured together on a tooling plate as described above and single-pass deposits were made with the matching composition wire. For the ambient temperature sample, a single preheat pass was used prior to deposition. This is standard operating procedure for the process; it helps to preheat and clean the surface by burning off any residual contaminants from the substrate plate to ensure that the first bead forms a metallurgical bond with the plate. The preheat and deposition conditions are shown in Table 9.3. The deposition conditions are the most stable for aluminium alloy deposits using the EBDED process. This deposit was made on the ambient sample immediately after resetting to the start location. For the moderate-temperature sample (348 K), three consecutive preheat passes were made at the same conditions described above.

Table 9.3: *Process conditions used for the single bead preheat and deposition trials.*

	Power (W)	Travel Speed (cm/s)	Wire feed (cm/s)
Preheat	2000	3.39	n/a
Deposition	2400	0.85	2.12

After the preheat passes, the thermocouple reading was monitored until the temperature peaked and stabilized, approximately 5 to 8 min. Then the deposition pass was conducted using the deposition setting described above. The same approach was used for the high-temperature sample (423 K), except five preheat passes were used. The measured peak temperatures for the samples are shown in Table 9.4. From this data it can be concluded that each preheat pass added about 15 K to the substrate material. The "ambient" sample, though not measured, was likely 15 K above ambient temperature when the deposition was made.

9.2.3 Single-Bead Deposit Preparation

All of the single-bead deposits were solution treated and aged according to peak hardness conditions as determined in a previous experiment: 800 K for 2 h with water quench, followed by 433 K for 18 h with air cool.[2] After heat treatment, each sample was sectioned into multiple pieces for analysis using an abrasive cut-off saw. A transverse slice through the bead and substrate plate was made 2.54 cm from the start edge for a standard metallographic mount. Thin slices of material were carefully cut from the fusion zone of the bead for chemical analysis, transmission electron microscopy (TEM), small-angle neutron scattering (SANS), and differential scanning calorimetry (DSC). First, the crown of the bead was ground flat, then three cuts were made to extract a thin slice of material as shown in Figure 9.6. For the SANS samples, the dimensions were 7 mm wide by 15 mm long by 1 mm thick. The width and depth of the

Table 9.4: *Measured baseplate temperatures after preheat passes. Error for the type K thermocouple used is 0.75% of the measured value resulting in uncertainty of approximately ± 2.75 K.*

	2L	2M	2H	5L	5M	5H	8L	8M	8H
Measured baseplate temperature (K)	n/a	345	393	n/a	329	362	n/a	348	388

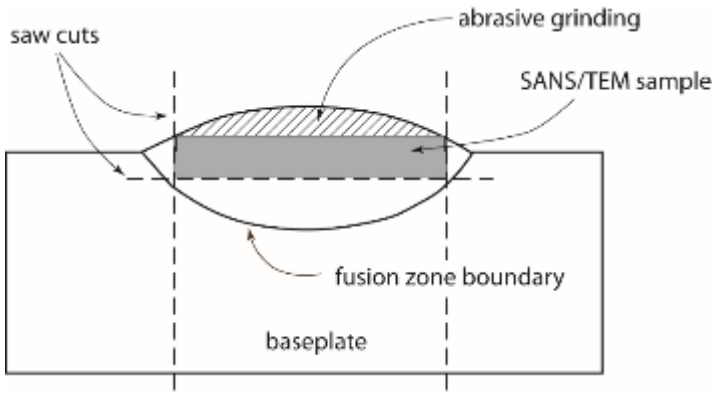

Figure 9.6: *Schematic showing how the thin slices of material were extracted from the single-bead deposit for examination.*

single-bead deposits limited the ability to make a larger sample. No additional preparation was necessary for the SANS sample. For the TEM samples, the saw cuts were made such that the thickness was approximately 0.5 mm. For chemical analysis, the SANS sample slice (post measurement) and the remnants of the TEM sample slice were used (0.2–0.5 g total mass). Chemical testing was performed by Luvak, Inc., Boylston, Massachusetts, USA, using inductively coupled plasma mass spectroscopy (ICP-MS). A full chemical analysis was performed on each baseplate and each wire composition. Magnesium content was measured on the extracted fusion zone material from the nine experimental single-bead deposits.

The transverse slices through the deposited bead and baseplate were mounted in Buehler EpoxiCure, a two-part cold-curing epoxy. The mounted samples were ground using SiC abrasive discs at 320, 400, and 600 grit and polished using diamond suspensions to 1 μm. Prior to etching, microhardness measurements were taken from the deposited bead and from the baseplate material far away from the fusion zone using a Leco M400-G1 microhardness tester. A 500 g-force load was used with a Vickers diamond pyramid indenter with measurements spaced approximately 0.75 mm apart. After hardness measurements were made, the samples were etched with Keller's reagent (95 mL H_2O, 2.5 mL HNO_3, 1.5 mL HCl, 1.0 mL HF) for 10 s to reveal microstructural features. Three photomicrographs were taken at 25x encompassing the entire deposited bead, and the images were subsequently stitched together into a wide field-

of-view panorama using Adobe Photoshop Elements. The cross-sectional area of the deposited bead was measured using ImageJ, an image analysis software package. In ImageJ, a pixels-per-millimetre relationship was established using the micron marker from the optical images. The deposited bead was then outlined using the selection tool, and the area, in square millimetres, was calculated using the established pixel-to-millimetre ratio. The solidification ripple marks on the surface of the solidified deposited beads were used to approximate the surface area of the molten pool. A Nikon DSL camera was used to capture a high-resolution image of the surface of each bead. The leading edge of the pool is assumed to be semi-circular, while the trailing edge is assumed to be the same shape as the solidification scallop marks. Details of the surface area calculation, along with a representative image of the scalloped bead surface is presented in Chapter 10 (see Figure 10.5).

A 3.05 mm diameter disc punch was used to extract TEM blanks from the 0.5 mm slice taken from the fusion zone. The discs were mechanically thinned using a disc grinder and successive grits of 600 and 1200 SiC abrasive paper until a final thickness of approximately 100 μm was reached. The foils were then electropolished to perforation using an E.A. Fishione automatic twin jet electropolisher at 40 V and 11.5 mA using an electrolyte containing 6% perchloric acid, 35% n-butyl alcohol and 59% methanol (volume percent) held at 233 K. Subsequent ion milling was performed using a Gatan Precision Ion Milling system to clean the samples and further thin the perforated area. A voltage of 2.5 keV with a sputtering angle of 5.5° was applied for 30 min. TEM analysis was performed on a Philips CM200 operated at 200 kV using a double-tilt specimen holder at the University of Canterbury, Christchurch, New Zealand.

Small-angle neutron scattering was performed on the BILBY instrument on the Open Pool Australian Lightwater reactor (OPAL) at the Australian Nuclear Science and Technology Organisation (ANSTO), Lucas Heights, New South Wales, Australia. The BILBY instrument

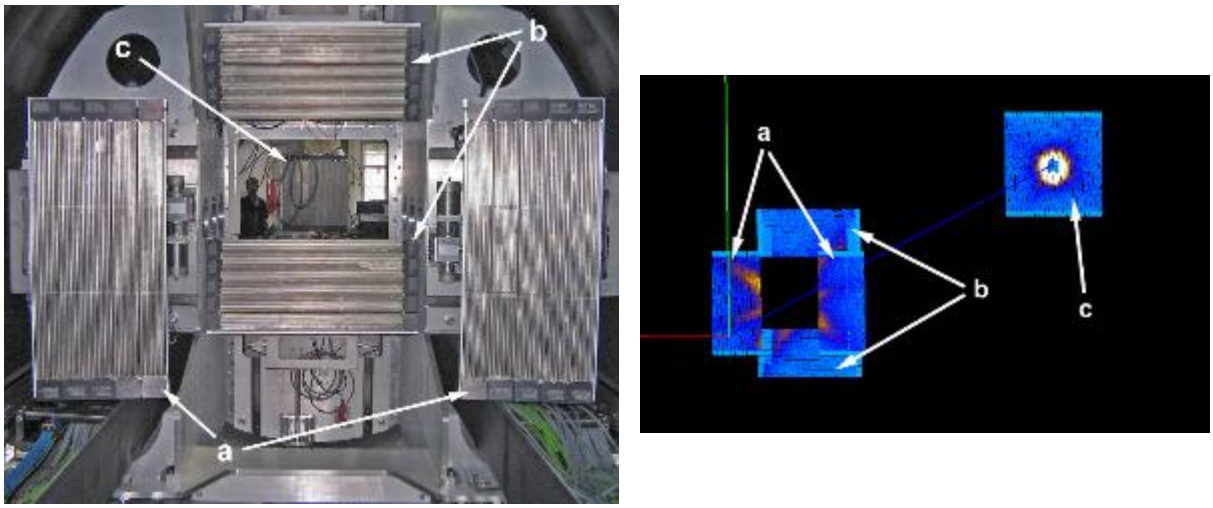

Figure 9.7: *Photograph (left) and raw 2D data set (right) showing BILBY detector configuration: (a) left/right curtain detectors, (b) up/down curtain detectors, and (c) rear detector.*

uses four mechanical choppers to pulse the beam, allowing it to operate in time-of-flight mode and measure a wide spectrum of wavelengths (2–20 Å). BILBY also has two sets of independently movable curtain detectors in addition to a rear detector inside an 18 m vacuum tank. This configuration allows it to capture a very wide q vector range in a single experimental setup. A photograph of the detector configuration along with an experimental data set is shown in Figure 9.7. The BILBY instrument physical setup for this experiment is shown in Table 9.5.

The aluminium slices from the single-bead deposits were approximately 7 mm wide by 15 mm long by 1 mm thick. These specimens were placed between two cadmium aperture discs with a 5 mm opening to shield against edge effects during the experiment. The sample and

Table 9.5: *SANS test conditions.*

Test condition	Value (mm)
source aperture diameter	40
sample aperture diameter	5
beam stop radius	80
rear detector distance from sample	16000
up/down curtain distance from sample	4000
up/down curtain distance from beam centre	250
left/right curtain distance from sample	3000
left/right curtain distance from beam centre	200

aperture discs were placed in a standard specimen holder. Photographs of the specimen details are shown in Figure 9.8. BILBY has a mechanical stage that can accommodate 10 specimen holders and can be programmed to run sequential experiments without user input. The first two trials were performed using a blocked beam condition and an open beam condition. These trials allowed background effects to be characterized so that they could be subtracted from the subsequent experimental data. The ten experimental samples included the nine samples shown in the matrix in Table 9.2 and one sample taken from the 0.5% Mg baseplate. This baseplate sample served as the nominal control value for the experiment; it had the target Mg composition of 0.5 wt%, and because it was not re-melted during the deposition trial, it was not subject to vaporization conditions.

The four mechanical choppers were set to give a wavelength band of 2–18 Å. For the experiment, data was collected from each sample for 20 min in transmission and 120 min in scattering. The first measurement showed definitive streaking in the 2D scattering plots, so the samples were rotated 90° and remeasured to check for consistency. The streaking was consistent for both scans. For the second scan, the samples were measured in transmission for 20 min and scattering for 140 min.

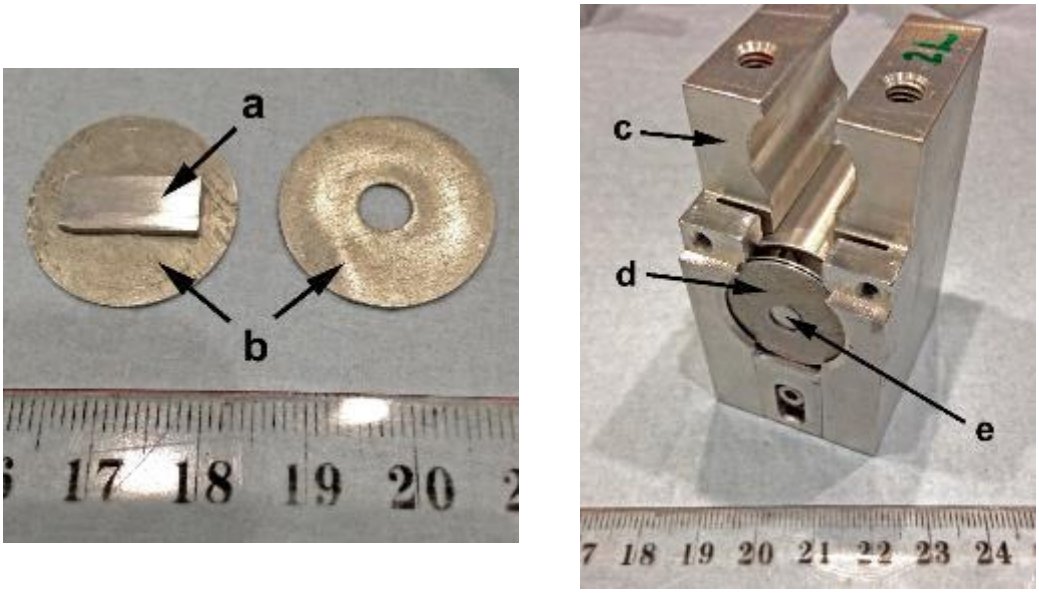

Figure 9.8: *Left: photograph of (a) specimen and (b) cadmium aperture discs; Right: (c) standard BILBY specimen holder showing (d) configuration of cadmium aperture discs and (e) experimental specimen. Scale marker in cm.*

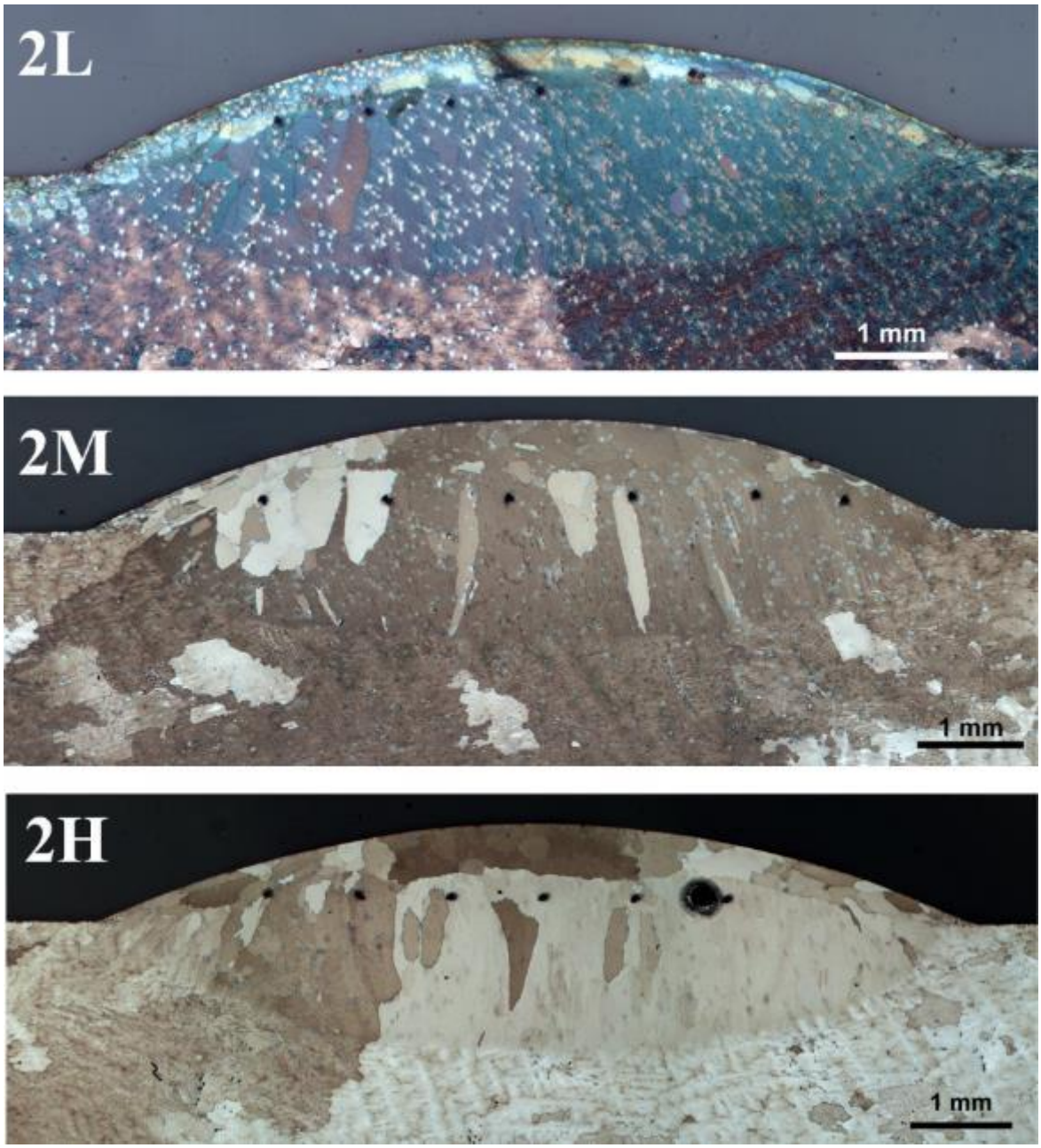

Figure 9.9: *Optical cross sectional micrographs of the 2-series deposited beads. Sample 2L was intentionally over-etched to enhance the intermetallic phase (bright spots) apparent in both the baseplate and the deposit. The intermetallic phase is present in the other samples as blue-gray specks. The over-etching is sample 2L was simply to emphasize the presence of the phase.*

9.3 Optical Metallography Results and Discussion

Cross-sectional micrographs are shown for each of the nine experimental samples in Figures 9.9, 9.10, and 9.11. Comparison of the nine samples shows that all but 5H had a similar cross-sectional bead profile. The transverse shape of the bead is lenticular, indicating that the heat source was operating in conduction mode and not keyhole mode. As discussed in Chapter

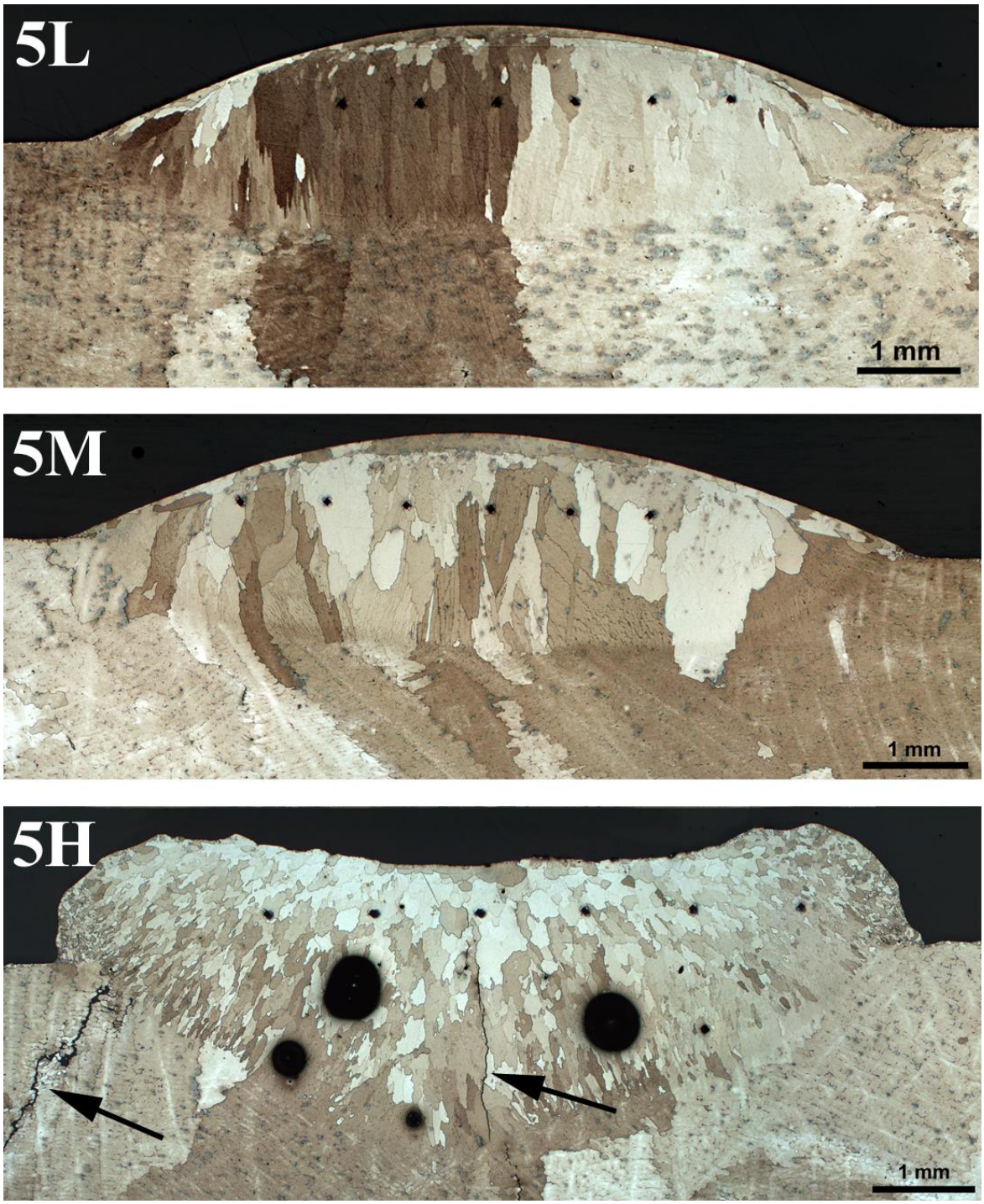

Figure 9.10: *Optical cross sectional micrographs of the 5-series deposited beads. Arrows in image 5H shows locations of cracks in substrate and deposit.*

7, this is preferred for additive manufacturing because it reduces the chance of beam-induced defects, such as collapsed keyhole porosity. Regardless, three of the nine samples showed macroscale porosity (2H, 5H, and 8L). The porosity was spherical, which indicates the pores are likely due to trapped gas. Note that the evenly spaced dark spots across each of the beads

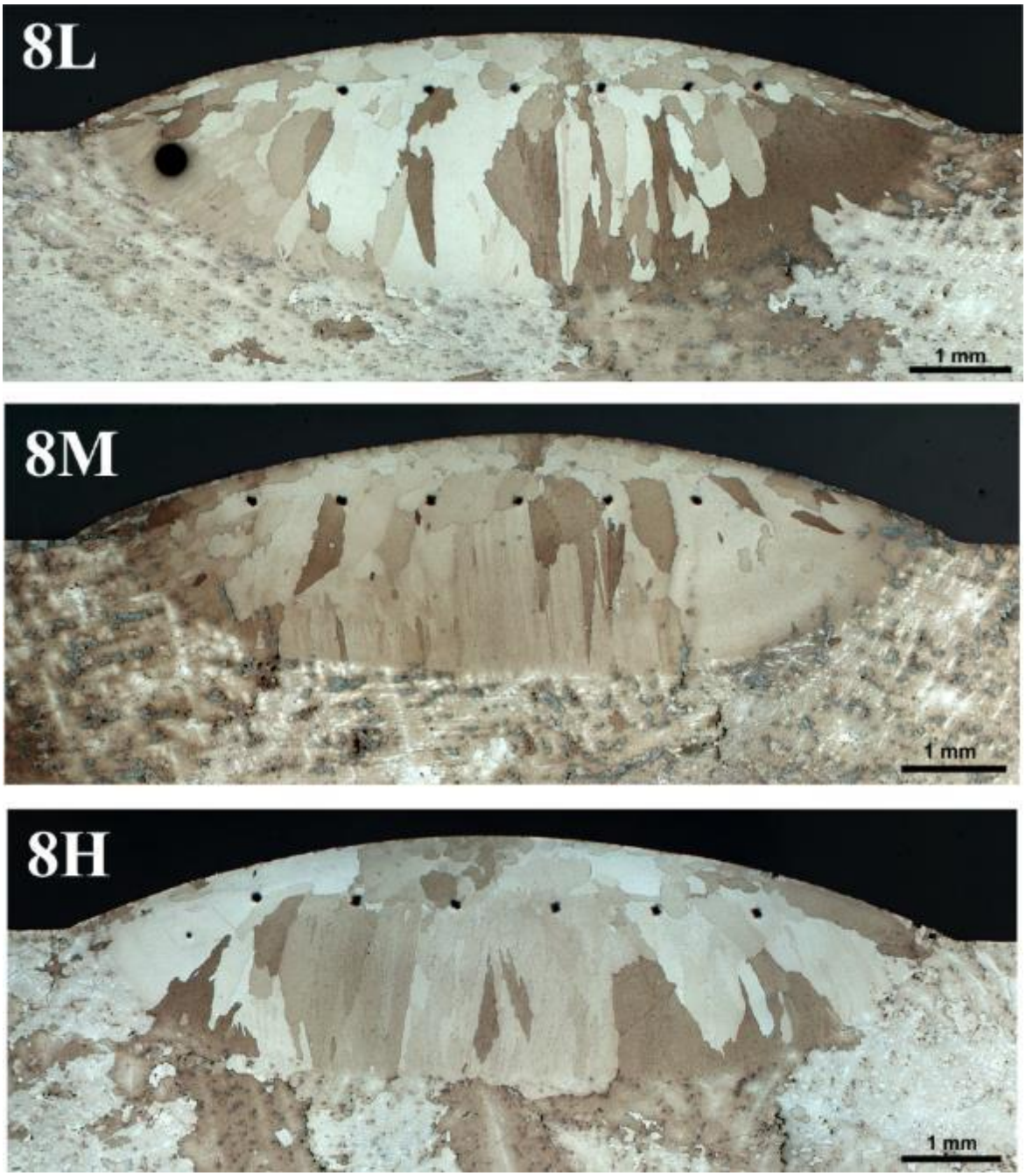

Figure 9.11: *Optical cross sectional micrographs of the 8-series deposited beads.*

are microhardness indents and not pores. Sample 5H showed particularly severe porosity that accounted for 3.7% of its cross-sectional area. Figure 9.12 shows a larger image of sample 5H along with notable defects found in the deposit and baseplate. The baseplate for sample 5H showed areas of solidification porosity, cracking, and relatively large gas porosity from the casting process. There was also a crack through the approximate centreline of the deposited bead. The centreline crack is likely due to hot tearing during solidification. Visually, sample

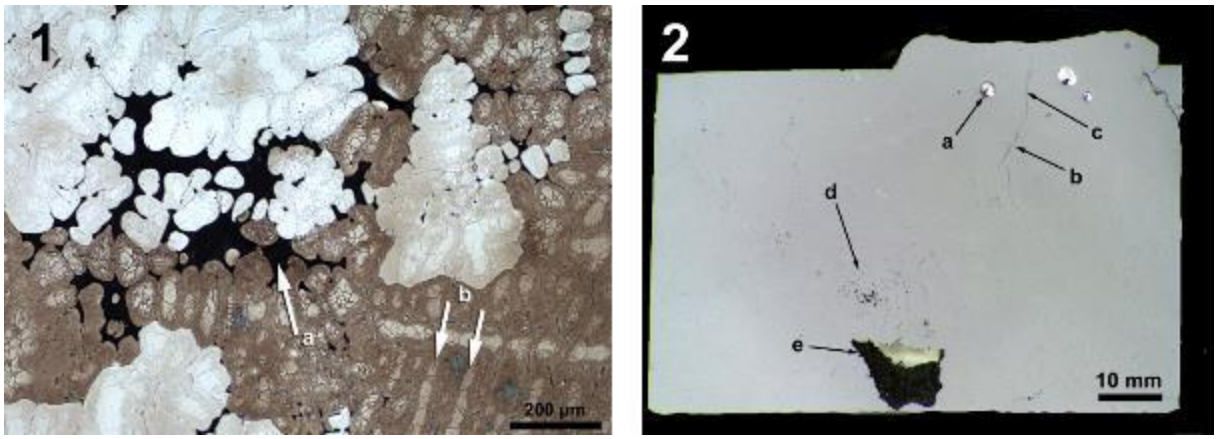

Figure 9.12: *Optical micrographs of sample 5H showing defects in both the deposited bead and the baseplate. Image 1 shows casting defects in the baseplate, including shrinkage voids (a) and suspected coring segregation (b). Image 2 shows the as-polished cross-section with gas pore in the deposit (a), crack in the baseplate (b), crack in the deposit (c), casting porosity in the baseplate (d), and gross casting void in the baseplate (e).*

5H had a rough, uneven appearance and did not have the hemispherical cap shape seen in all the other samples at the location the cross-sectional cut was made. Also, during the deposition process, there was considerable spatter from the bead, and the molten pool was visibly turbulent. Again, this was unique to sample 5H. With this evidence, it can be concluded that there were significant casting defects in the substrate plate for 5H, which likely included major porosity and possibly segregation of alloying elements. While it cannot be determined with absolute certainty, it is assumed that these defects in the substrate plate affected the deposition and resulted in sample 5H's unusual behaviour and appearance.

With the noted exception of sample 5H, all the other samples showed similar grain structures. A few notable features can be seen in sample 8L as shown in Figure 9.13. The grain structure is columnar from the deposit/baseplate interface to just below the bead crown surface where the grains become more equiaxed. There is also strong evidence of epitaxial growth in the deposited beads based on visual contrast in the etched cross-section. The grains maintain the approximate orientation of the baseplate and grow vertically, resulting in a distinctly columnar shape. The preferred solidification growth direction in cubic materials is along the ⟨001⟩-type directions.[3] and it is likely that these grains obtain this texture. This preferential

growth is enhanced when there is a steep thermal gradient present and has been documented for welding and additive manufacturing processes in many materials.[4-6]

None of the single bead deposited samples showed evidence of a heat affected zone (HAZ). Many AM-fabricated alloys show evidence of layering due to microstructural scale differences in the HAZ. While multiple layer deposits were not explored in this study, prior work has shown no evidence of a HAZ. This is significant in that it implies that the microstructure is uniform across the layer boundaries and free from gradients that could be a preferred path for strain localization, crack propagation, or other failure mechanism in the material. The lack of HAZ means the material is free from microstructural gradients and should have more uniform properties across the layers.

Sample 5H is also distinctively different with respect to the grain structure. As can be seen in Figure 9.10, the grain structure still shows columnar features; however, the overall grain size is much smaller and the grain aspect ratio is significantly reduced. The turbulence

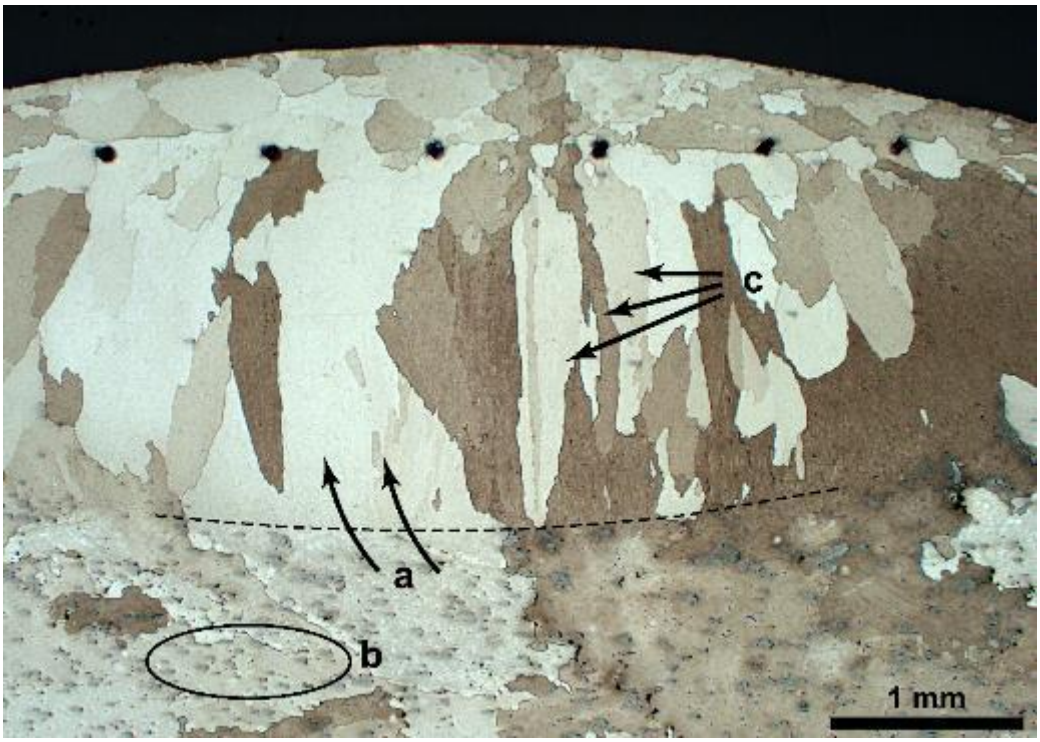

Figure 9.13: *Micrograph of sample 8L showing distinctive solidification features present in the deposited beads. (a) Epitaxial-like growth is apparent at the substrate/deposit interface, (b) the intermetallic eutectic present in the cast baseplate have been fully dissolved in the deposit, and (c) columnar solidified grain structure throughout the bulk of the deposit.*

witnessed in the molten pool during the deposition process likely influenced the grain structure development. Other research has documented that agitation in the molten pool during welding can refine the grain structure by promoting nucleation or by fracturing dendrites at the solidification front. The dendrites then provide nuclei within the melt.[7-8]

Finally, the baseplate microstructure and some of the deposited microstructures show uniformly distributed coarse particles. These particles (shown clearly as the bright spots in image 2L in Figure 9.9) likely formed during solidification as the insoluble elements were rejected ahead of the solidification boundary. Most of the particles decorate the interdendritic regions of the baseplate and the grain boundaries in the deposit. The particles were very apparent in the 2-series deposited beads but were less apparent in the 5-series and almost completely absent in the 8-series samples (compare baseplate and deposited bead in Figure 9.13). An explanation for the origin and difference in intermetallic content in the deposited beads will be discussed in Section 9.6.

9.4 Electron Microscopy Results and Discussion

Scanning electron microscopy (SEM) was performed on select samples to aid in the identification of the large, interdendritic phase present in the baseplates and the 2- and 5-series deposited beads. Figure 9.14 shows a representative image from sample 2L taken within the baseplate material. EDS was performed on three locations within the field of view, identified as “a,” “b,” and “c” in the image. The two locations (“a” and “b") corresponding to the interdendritic phase show an approximate Al:Cu ratio of 8:1. Location “c” is in the matrix and shows the average Cu concentration (5 wt% or 20:1 Al:Cu ratio). Point “a” has increased Mn concentration over the concentration in the matrix, and points “a” and “b” show increased Ag.

Talamantes-Silva et al. did a comprehensive study of precipitate phases in aluminium copper alloys using SEM and x-ray diffraction.[9] Their alloy had similar concentrations of Cu, Mg, and Mn but lacked the Ag present in the alloy used in this study. They determined that the

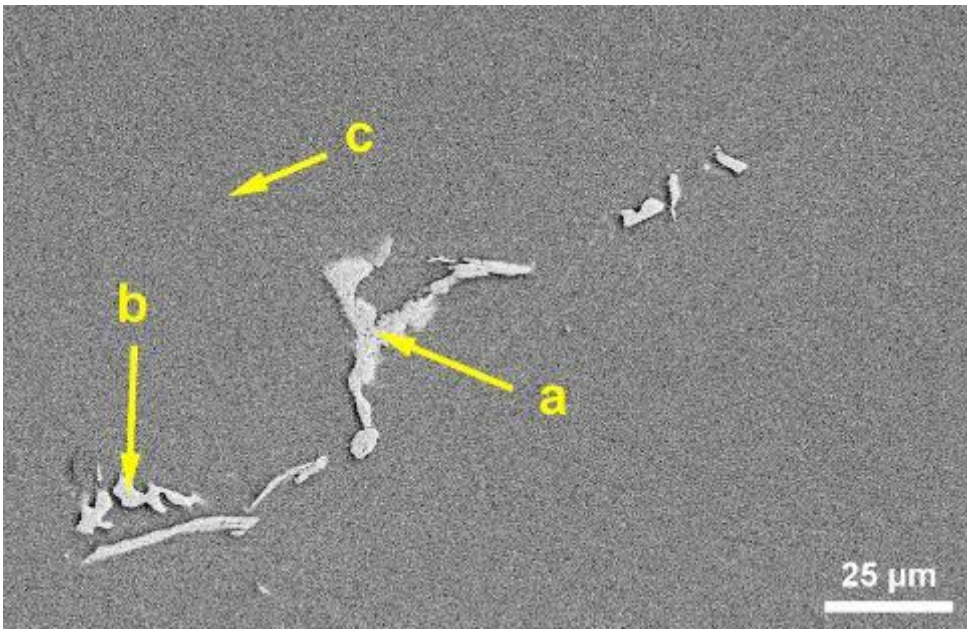

Figure 9.14: *Scanning electron micrograph of intermetallic phases seen in the baseplate and the 2- and 5-series deposits. See text in Section 9.4 for label descriptions.*

interdendritic phase was actually a combination of at least three distinct phases: Al_2Cu, Al_7FeCu, and Al_2Mn_3Cu. They described this as a "complex eutectic." The insoluble elements (Fe, Mn) are rejected ahead of the solidification front and are the last to solidify within the interdendritic regions. The additional element present in the alloy in this study, Ag, is effectively insoluble in aluminium at room temperature so it also is likely rejected into the intermetallic phase. Thus the intermetallic likely contains one or more phases with Al, Mn, and Ag present. Exact identification of this microconstituent was outside the scope of this study.

TEM analysis was performed on select samples to characterize the size, shape, and habit plane of the precipitates that formed during the aging heat treatment. Figure 9.15 shows a representative bright-field micrograph from each of the 2-, 5-, and 8-series of samples. To aid in particle identification, the samples were tilted to a particular zone axis prior to bright-field image capture. A selected area diffraction pattern was taken at the particular zone axis and is shown as insets in each of the three images in Figure 9.15. The micrograph from sample 2L (Figure 9.15a) is taken near the $\langle 100 \rangle_\alpha$ zone axis. As has been documented by many previous studies, the θ phase (also θ′ and θ″, or generically θ-type) obtains specific orientation

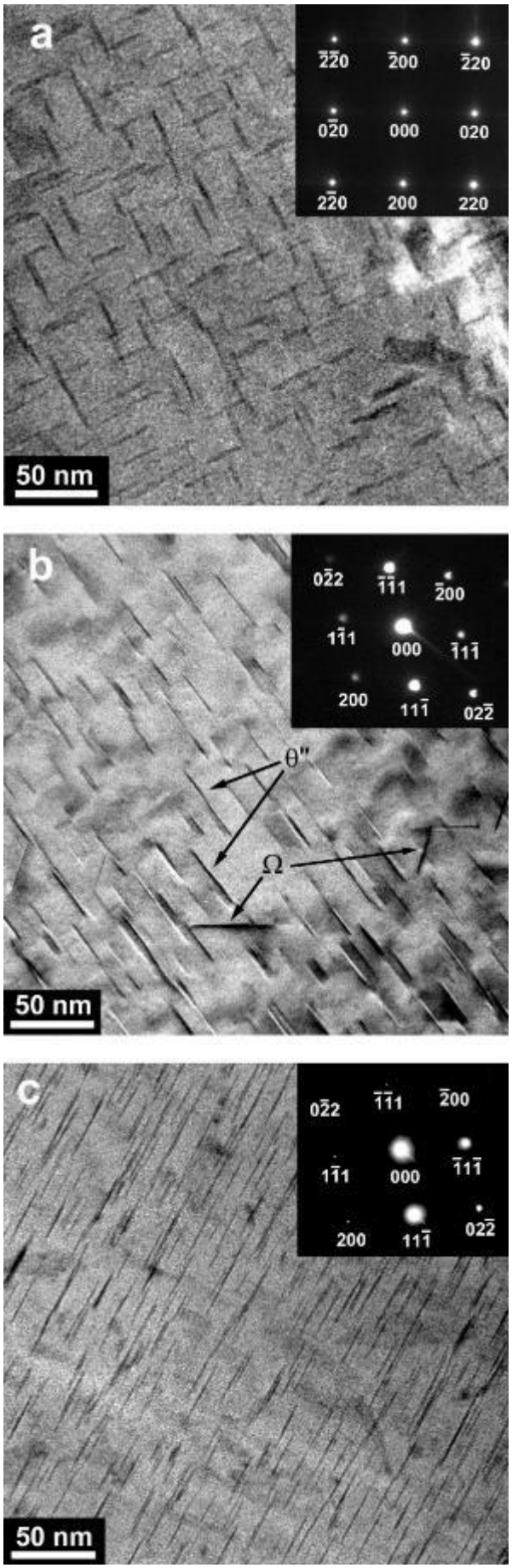

Figure 9.15: *Transmission electron micrographs of (a) sample 2L, (b) 5H, and (c) 8M. Image (a) is taken along the ⟨100⟩ zone axis, while images (b) and (c) are taken along the ⟨110⟩ zone axis (see SAED inset in each image). Image (b) identifies one variant of θ″ and two variants of Ω. Image (a) contains all θ; image (c) contains all Ω.*

relationships with the matrix that lie along the $\{100\}_\alpha$ family of planes, while the Ω phase resides on the $\{111\}_\alpha$ family of planes.[10-12] When imaged from near the $\langle 100\rangle_\alpha$ zone axis, the θ-type phase can be viewed edge-on, which helps in determining thickness and diameter. Also, because the $\{100\}_\alpha$ planes are 90° apart when viewed down the [100] direction, the particles can be confidently identified at θ-type if the misorientation between variants is 90°. Clearly, the particles shown in Figure 9.15a are all θ-type, as they appear edge-on and the two variants are 90° apart. This sample was also examined near the $\langle 110\rangle_\alpha$ zone axis in search of the Ω phase, but none was observed.

It is difficult with absolute certainty to determine if the Al_2Cu precipitate present in Figure 9.15a is θ″ or θ′. Ringer and Hono calculated a metastable phase diagram for the Al-rich side of the Al-Cu phase diagram with associated solvus boundaries for GP zones, θ″, and θ′.[13] At the aging temperature used in this study (433 K), a 5 wt% copper alloy would be just below the GP solvus and well below the θ″ and θ′ solvus lines, indicating that all three phases are possible. Studies have also correlated aging temperature to precipitate character. Ringer and Hono also documented separate Al-Cu aging studies at 403 K and at 463 K. The lower aging temperature allows extensive GP zone formation followed by θ″ at longer aging times. Aging at 463 K prevents GP zone formation, and θ″ nucleates directly from the supersaturated solid solution. Papazian[14] did a calorimetric study of precipitation in Al-Cu (alloy 2219) at the same aging temperatures as Ringer and Hono used in their study. At the lower temperature, the microstructure was predominantly θ″ and the particle diameters were about 10 nm after 2.2 d of aging. The higher temperature aging showed primarily θ″ up to 8 h of aging, after which θ′ began to form. The microstructure was completely θ′ after 36 h (T62 temper condition). The aging treatment used in this study falls in between the two conditions discussed in prior work cited above (433 K for 18 h), and the composition of the alloys in this study may alter the details

of the metastable solvus temperatures and time-temperature-transformation relations; thus, it is difficult to tell with certainty which phase is present in the TEM micrographs. Fundamentally, this detail is unimportant, as it does not matter which {100}-Al_2Cu variant the particles are (θ″ or θ′); it only matters that they are not Ω. The Ω phase on the {111} planes are critical for achieving peak strength in alloy 2139, thus the interest is in the relative fraction of W and θ-type. From this point onward, it is assumed that the particles are an undetermined mixture of θ″ and θ′, but for convenience the phase will be referred to as θ′.

Sample 5H in Figure 9.15b shows a mixture of phases present. This image was taken near the $\langle 110 \rangle_\alpha$ zone axis (see inset), which makes two of the four habit plane variants of Ω visible and one of the three habit plane variants of θ′ visible. Determination of which particle corresponds to which particular Al_2Cu variant can be made by measuring the angles between the particles. In face-centred cubic crystals, the angle between the {111} and {100} planes is 54.7°, and the angle between different {111} planes is 70.5°. The angles between the particles were measured using ImageJ image analysis software; this analysis was used to determine which particles are θ′ and which are Ω. The particles are labelled in Figure 9.15b. In this field of view, a considerably higher fraction of θ′ is present than Ω. Sample 5H was found to have 0.21 wt% Mg from ICP-MS. As will be concluded in later analysis within this chapter, 0.20 wt% Mg is approximately the critical concentration necessary to encourage the formation of Ω over θ′.

Sample 8M in Figure 9.15c shows only a high density of Ω present, which was found to have 0.30 wt% Mg from ICP-MS. This image was also captured near the $\langle 110 \rangle_\alpha$ zone axis (see inset), though it was tilted slightly away from the zone such that only one of the two variants visible at that zone axis were diffracting. This sample was also tilted to the $\langle 100 \rangle_\alpha$ zone axis and no θ′ was observed (not shown). Given the small sampling volume of the TEM foil, this

cannot conclusively eliminate the possible presence of θ′ in this sample, but it clearly has much less than either 2L or 5H. Because all three images from the three different samples were taken at the same magnification, it is useful to compare the respective sizes of the precipitates present. The θ′ has much smaller diameter than the Ω phase. This size difference will be quantified later in the chapter using small-angle neutron scattering.

Quantification of the precipitate volume fraction can be accomplished in the TEM using convergent beam electron diffraction (CBED) to determine the foil thickness.[15] With this method, an image of the two-beam condition is captured at the same location as the bright-field image showing the particles. In this two beam image, the Kossel-Mollenstedt fringes are visible (Figure 9.16). The measured distance between these fringes ($\Delta\theta_i$) can be used to determine the deviation (s_i) for the *i*th fringe using

$$s_i = \lambda \frac{\Delta\theta_i}{2\theta_B d^2} \tag{9.1}$$

where λ is the wavelength, θ_B is the Bragg angle for the diffracting plane, and d is the interplanar spacing. Each s_i is assigned an integer value n_i and s_i^2/n_i^2 is calculated. The calculated value s_i^2/n_i^2 is plotted with respect to $1/n_i^2$. If this relationship is linear, the foil thickness is given by the intercept $1/t^2$. If not, the integer n_i is incremented by 1 and the

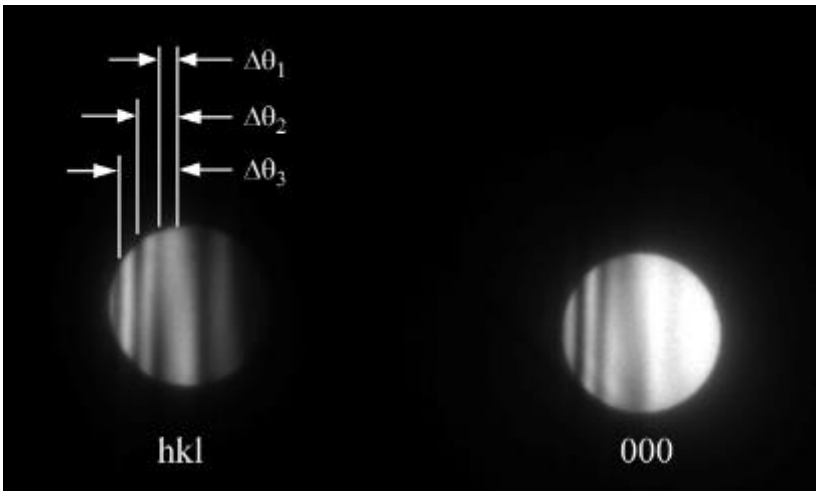

***Figure 9.16**: TEM image showing two beam condition with visible Kossel-Mollenstedt fringes and the method for measuring the distance, Δθ.*

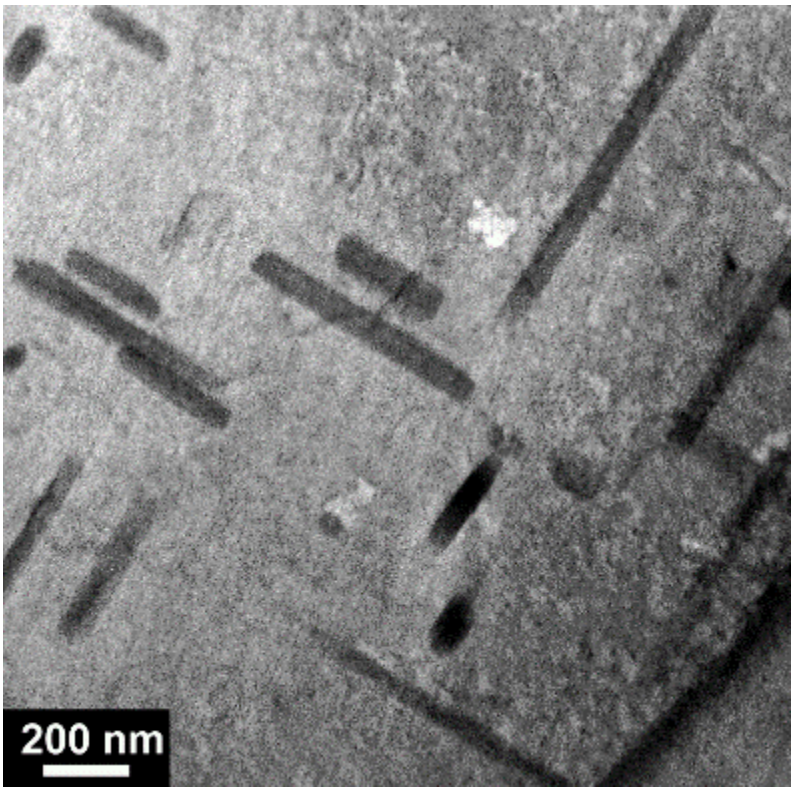

Figure 9.17: *Transmission electron micrograph of $Al_{20}Cu_2Mn_3$ ("T" phase) dispersoid particles in sample 8H.*

process is repeated until the relationship is linear. Unfortunately, the digital camera on the TEM used for this analysis was not capable of capturing these images due to the risk of damaging the camera. The attempt to quantify the precipitate volume fraction using TEM had to be abandoned.

There was a separate phase identified during TEM examination, shown in Figure 9.17. This phase is rod-shaped and is much larger than the Al_2Cu phases. It has a diameter of 50–100 nm and variable length in the hundreds of nanometers range. Other published TEM studies in this alloy have identified this phase as $Al_{20}Cu_2Mn_3$, often labelled the "T" phase.[16-17] The T phase does not precipitate from the solid solution during aging but rather forms on solidification or during the solution heat treatment. These incoherent dispersoid particles refine the grain structure and improve overall mechanical properties.[16] They are present in all of the samples, because the Cu and Mn concentrations are constant across samples. For the microhardness

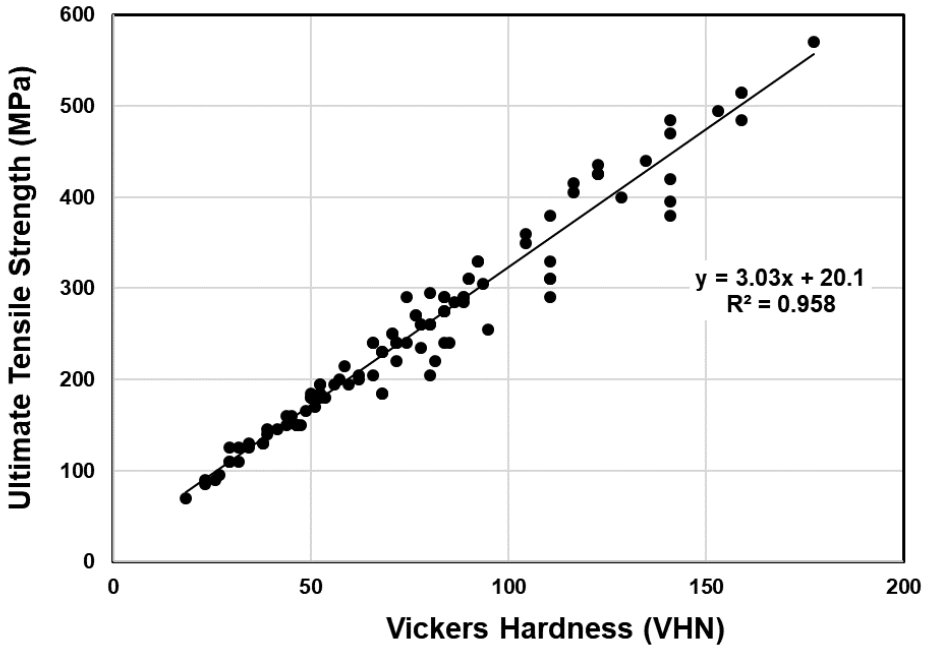

Figure 9.18: *Plot of hardness versus ultimate tensile strength for wrought aluminium alloys in the T6_ condition. Data from ASM Metals Handbook: Desk Edition.*[18]

measurements, it was assumed that the contribution of the T phase was consistent across all nine samples.

9.5 Microhardness Results and Discussion

Microhardness measurements were taken in both the deposit and baseplate of each sample using a LECO M400-G1 with a Vickers indenter. Aluminium alloys have been shown to exhibit a strong linear relationship between hardness and strength.[18] Data from the *ASM Metal Handbook: Desk Edition* was used to plot the graph in Figure 9.18.[19] The data was selected from wrought aluminium alloys in solution treated and aged condition (T6 temper). The data shows a strong linear relationship with an R^2 value of 0.96. The linear fit equation is $\sigma_{UTS} = 3.0333(VHN) + 20.146$, where σ_{UTS} is the ultimate tensile strength in MPa and VHN is the measured Vickers hardness number. Using this equation, a predicted ultimate tensile strength was calculated using the measured hardness values from each sample. These predicted values are shown in Table 9.6 and plotted in Figure 9.19. Also shown in Table 9.6 is the calculated ratio in hardness between the baseplate material and the deposited bead, both of which were

Table 9.6: *Measured hardness values from each of the samples (solution heat treated and peak aged condition). Also shown is a prediction of the strength using a calculated linear relationship and the ratio between the deposit hardness and baseplate hardness.*

	Hardness (VHN)	Predicted UTS (MPa)	Ratio to Baseplate Hardness
2L	130 ± 2	415 ± 30	1.02
2M	130 ± 3	415 ± 30	1.02
2H	130 ± 2	415 ± 30	1.02
5L	134 ± 8	427 ± 50	0.92
5M	136 ± 3	433 ± 30	0.94
5H	136 ± 4	433 ± 30	0.94
8L	143 ± 2	454 ± 30	0.86
8M	143 ± 3	454 ± 30	0.86
8H	141 ± 5	448 ± 40	0.85
2	127 ± 10	405 ± 60	
5	145 ± 20	461 ± 70	
8	166 ± 8	525 ± 50	

subjected to the same heat treatment. Because the Mg concentration is the only variable among the samples, the difference in hardness in the three-sample series is primarily due to the Mg concentration. The 2-series had very little Mg content in the baseplate and feed wire, so the vaporization effect was minimal. The 2-series baseplate and deposits had essentially the same hardness. The 8-series had higher overall Mg content, so the difference in hardness between the 8-series samples and baseplate was larger due to vaporization loss of Mg in the deposited bead. This effect will be discussed in greater detail in the following chapter. While the focus is on Mg content due to vaporization loss, there are also other factors that can affect the measured hardness in the samples, including grain size, crystallographic texture, and chemical segregation. These effects may also be factors in the measured hardness difference between the baseplates and deposited bead material. The microstructures vary somewhat; however, the differences in hardness are assumed to be dominated by Mg concentration variations and the resulting effect on precipitate character.

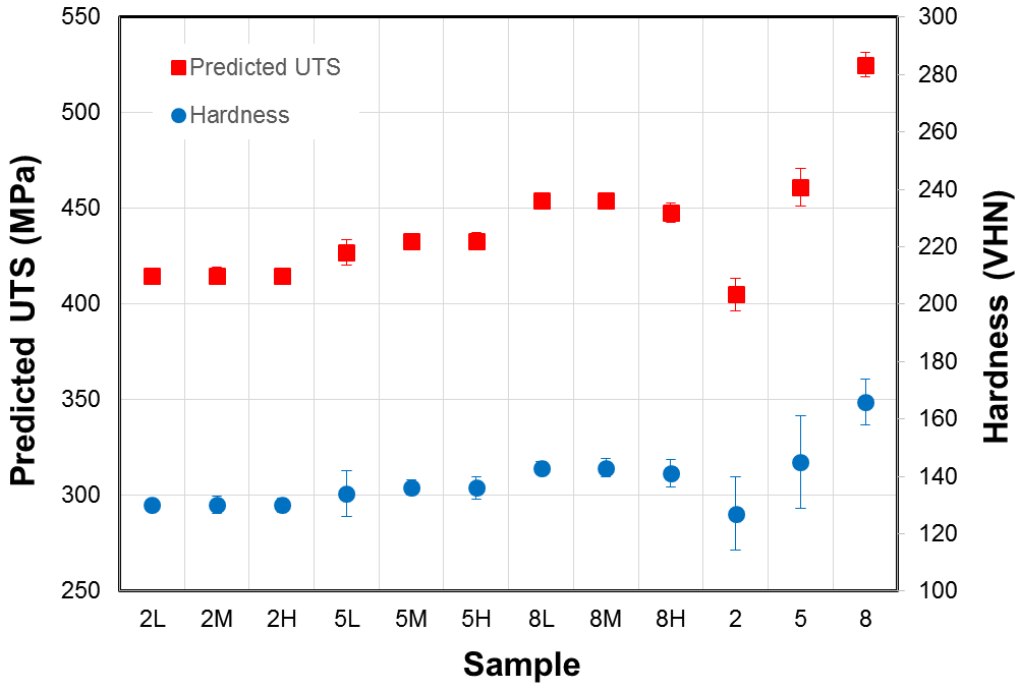

Figure 9.19: *Graph showing measured hardness values (blue data) and predicted tensile strength (red data) for each sample.*

9.6 Small-Angle Neutron Scattering Results and Discussion

Small-angle scattering (X-rays and neutrons) have been used to characterize a variety of precipitation-hardened aluminium alloys.[20] In fact, the original work by Guinier establishing the existence of what we now call GP zones was conducted using small-angle X-ray scattering.[21] The technique is well suited for characterizing distributed particles in the 1–100 nm size range, which is the expected particle size range based on published studies of the alloy used in this experiment.[10] Neutrons were chosen for this experiment based on availability at the OPAL reactor at the Australian Nuclear Science and Technology Organisation. The details of the experiment are described in Section 9.1.3.

The two-dimensional background-subtracted small-angle neutron scattering (SANS) plots for each of the nine experimental samples and the nominal 0.5 wt% Mg baseplate sample

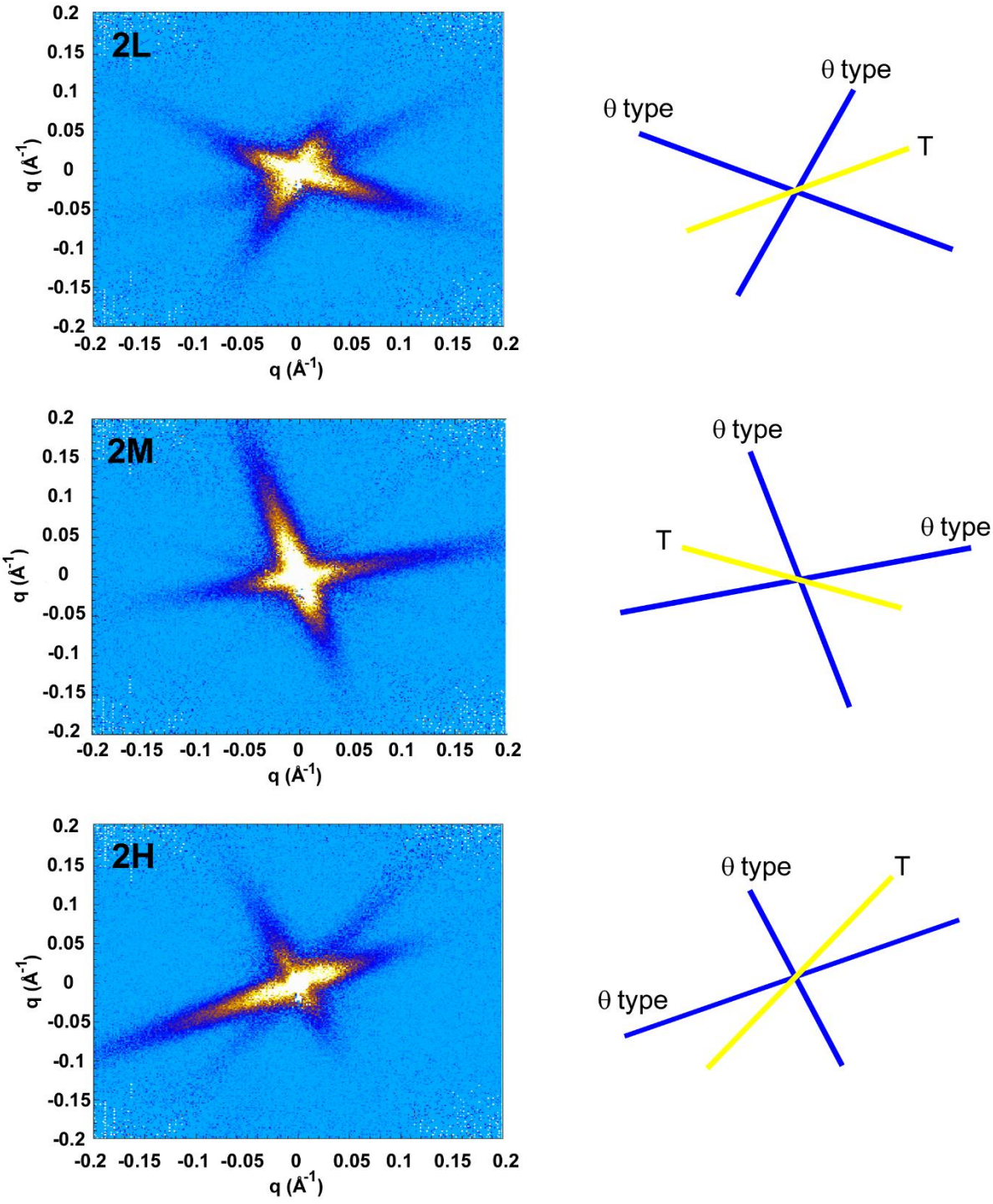

Figure 9.20: *Two-dimensional small-angle scattering plots from the 2-series samples with their associated scattering streak interpretation.*

are shown in Figures 9.20 through 9.23. The crystallographic texture has a distinct effect on the scattering from each sample. As described above and shown in Figure 9.13, the solidified grains

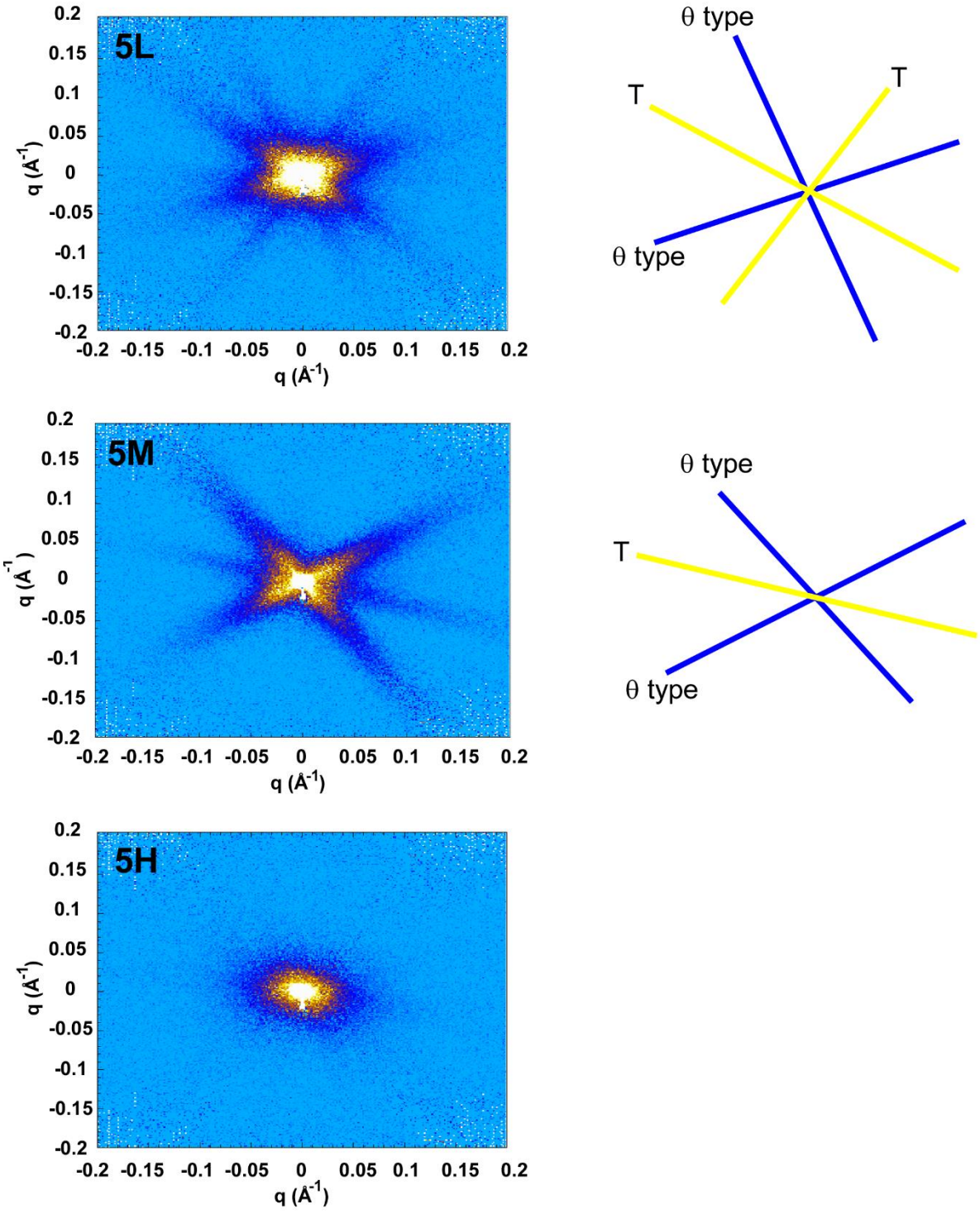

Figure 9.21:*Two-dimensional small-angle scattering plots from the 5-series samples with their associated scattering streak interpretation. Sample 5H has no discernable streaks due to the more random nature of the grain structure with respect to the neutron beam direction.*

in the deposited bead grow normal to the plane of the baseplate. When the SANS samples were extracted from the deposited beads, the thickness dimension of the sample was aligned with the preferred direction of crystal growth in the deposit. This orientation was necessary to get a

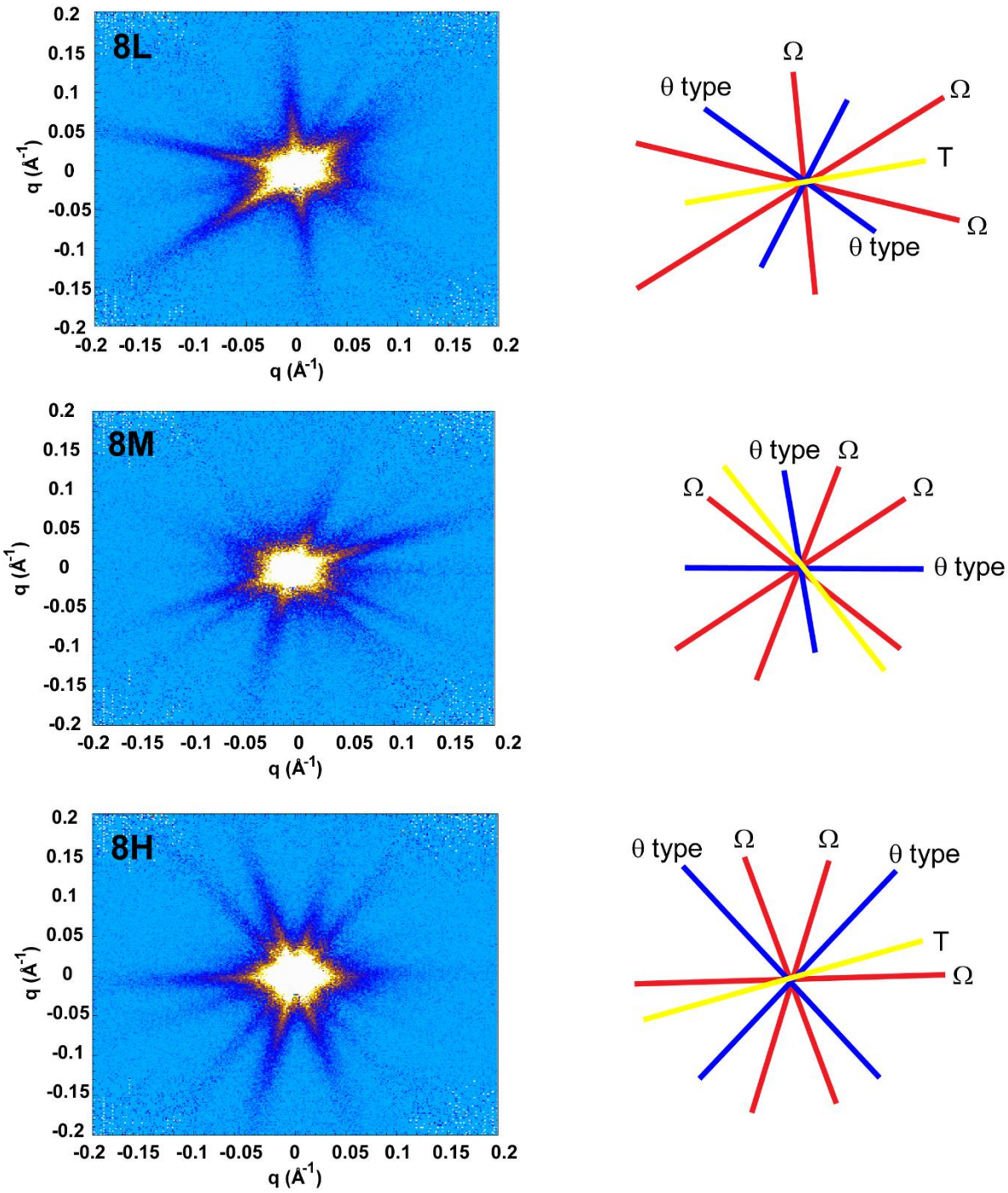

Figure 9.22: *Two-dimensional small-angle scattering plots from the 8-series samples with their associated scattering streak interpretation.*

sample with the required dimensions for the test; however, it provided a distinct benefit in terms of the 2D signal captured during the experiment. The favoured ⟨001⟩ crystal growth direction in the deposited bead was lined up parallel to the direction of the neutron beam during the experiment. This preferred alignment of the crystals with respect to the beam led to a distinctive

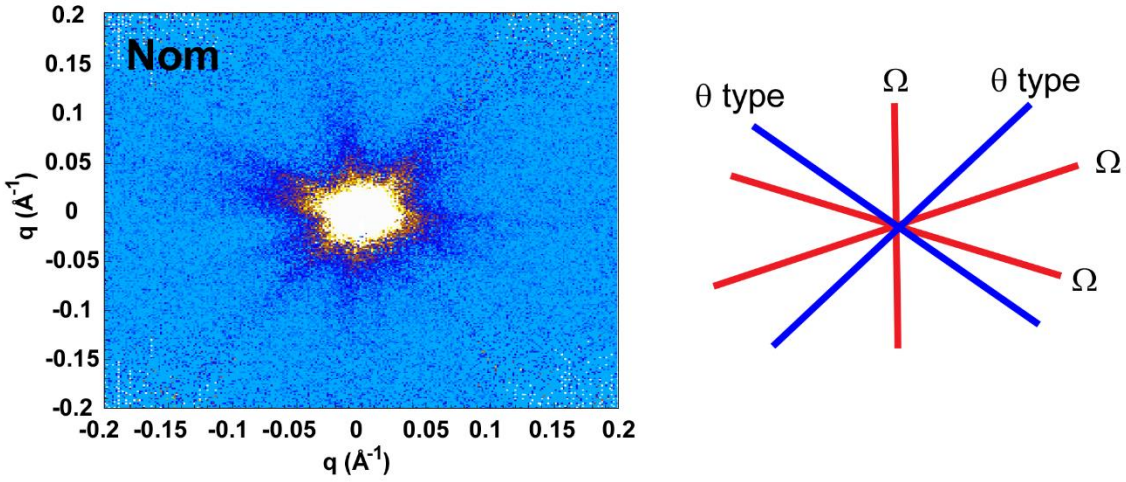

Figure 9.23: *Two-dimensional small-angle scattering plots from the baseplate sample (nominal 0.5 wt% Mg) with its associated scattering streak interpretation.*

scattering pattern in the 2D images, indicative of which planes within the crystal were scattering. In this alloy, the fact that the θ′ phase and the Ω phase reside on different planes means that the scattering signal from the 2D plots can be used to qualitatively determine the precipitate phase present. This has been described extensively by other researchers working in a similar aluminium system.[22-24] The streaking effect is similar to that seen in TEM selected area diffraction patterns. The thin film effect creates reciprocal lattice rods (relrods) such that are parallel to the beam and normal to the plan of the TEM foil. This makes diffraction spots visible even when the Bragg condition is not precisely satisfied.[15] In these samples, viewing the precipitates edge-on with respect to the neutron beam means that the relrods are oriented perpendicular to the frame of beam. Thus, the Ewald sphere intersects these relrods through their long axis resulting in a streak in the direction of reciprocal space diffraction spot.

The effect of the scattering from the two different particles is described schematically in Figure 9.24a and compared with the actual data from sample 8H in Figure 9.23b. The schematic representation was adapted from work by De Geuser et al.[24] Their work studied Al-Cu-Li alloys in which the strengthening phases are θ′ on $\{100\}_\alpha$ planes and T1 (Al_2CuLi) on $\{111\}_\alpha$ planes. While one of the phases is different (T1 versus Ω), the preferred habit plane of the two systems

is identical; thus, we can apply the same quantitative descriptions of scattering streaks to determine which phases are present in each sample. The direction of the streaks can be related to the angle between the sample normal and the {111} planes (for Ω) and the {100} planes (for θ). In the 2D plots, the angles from past experiments by De Geuser et al. can be measured and correlated to the results from this experiment. The angles between each streak for each associated phase are shown in Figure 9.24a.

Returning to Figures 9.20 through 9.22, comparisons can be made among the nine samples in terms of the particular phases present and their relative quantities. The 2-series samples are dominated by scattering from particles on the $\{100\}_\alpha$ planes, indicating primarily θ′ (while the SANS data does not differentiate between θ″, θ′, or θ, for consistency θ′ will be used in this discussion). The 5-series samples show more of a mix of the two phases with streaks from both present. Sample 5L shows more prominent evidence of Ω compared to sample 5H. Sample 5H shows only very faint streaking from either phase. Recall that this sample had less crystallographic texture compared to the other samples (Figure 9.10). This lack of preferred orientation reduces the intensity of the streaking due to scattering off of each distinct matrix orientation. In a perfectly random crystal, there would be no streaks present; however, as

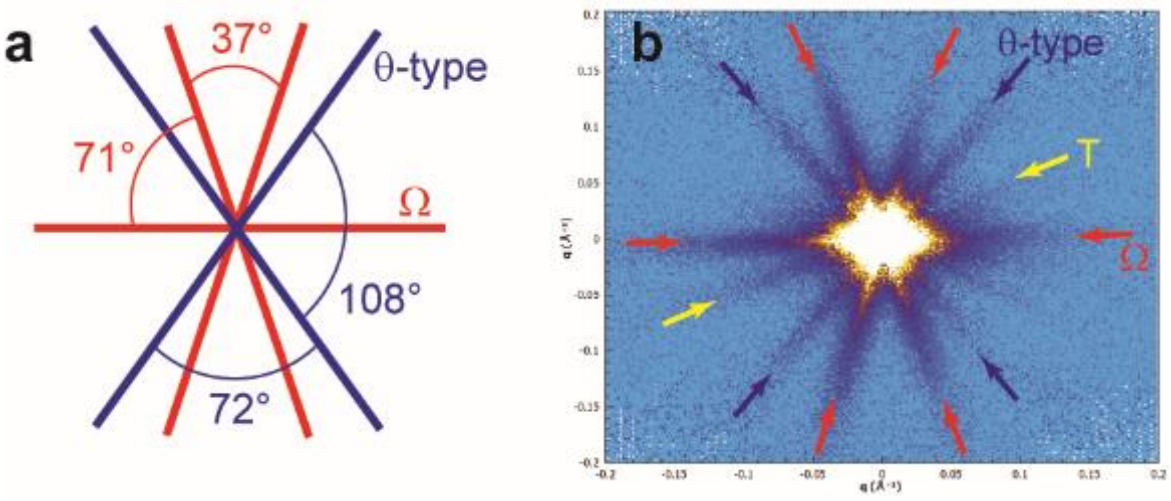

Figure 9.24: *(a) Schematic representation of the streaks present in the small-angle scattering data and (b) the 2D scattering pattern from sample 8H. The red lines in (a) are associated with the Ω phase, while the blue lines are associated with the θ′ phase.*

discussed later in this section, useful data can still be extracted from the scattering experiment by using the integrated intensity over the experimental q range and fitting a curve to the results. Samples in the 8-series showed the strongest streaking due to the Ω phase on the $\{111\}_\alpha$ planes. Because the 8-series samples had the highest Mg content, this result was expected. Finally, the small-angle scattering plot of the nominal sample (0.5 wt% Mg baseplate) shows that all streaks are present, but they are much less distinct compared to those of the other deposited beads. Similar to sample 5H, the nominal sample does not have a strong crystallographic texture; the streaking is less intense because the scattering planes are more randomly oriented.

All of the 2D scattering plots contain additional faint streaking not associated with either the θ′ phase or the Ω phase. This streaking is assumed to be from the large T phase ($Al_{20}Cu_2Mn_3$) described in the TEM discussion in Section 9.4 and noted in Figure 9.17. As with θ′ and Ω, the streaking in the 2D patterns implies a specific habit plan for the T phase and orientation relationship (OR) with respect to the aluminium matrix. Chen has identified these ORs and determined that there are at least three distinct variants.[17] These three variants are OR I: $\{200\}_T\langle010\rangle_T \parallel \{200\}_{Al}\langle010\rangle_{Al}$; OR II: $\{200\}_T\langle010\rangle_T \parallel \{403\}_{Al}\langle010\rangle_{Al}$; OR III: $\{200\}_T\langle010\rangle_T \parallel \{301\}_{Al}\langle010\rangle_{Al}$. The specific OR variant was not correlated with the streaking in the 2D SANS plots in this experiment. Since the neutron beam was interrogating a 5 mm diameter sample 1 mm thick, it encompassed many grains within the deposited bead. The T phase was identified within the bulk of the grains and it is assumed that there was sufficient phase present to result in streaking in the 2D SANS patterns.

The background-subtracted 2D scattering data for each sample was radially averaged and plotted as a function of the scattering vector ($q = 4\pi \sin\theta/\lambda$), where 2θ is the scattering angle and λ is the wavelength (2–18 Å in this experiment). The results are shown in Figure 9.25. The scattering trend for all samples is essentially the same, with the most significant deviations around 0.01 $Å^{-1}$. This range corresponds to a feature length scale of about 100–1250 Å,

determined through the relationship $d \sim 2\pi/q$, where d is the feature length.[25] The most significant deviations among the samples can be attributed to differences in the size of the precipitate phases. The 8-series and the nominal sample show the most significant deviation from compared to the other samples. This is due to the presence of a large (or larger) amount of Ω in these two samples.

The traditional method for interpreting SANS/SAXS data is through manipulation of the data, as plotted in Figure 9.25. A few specific examples are shown in Figure 9.26. Figure 9.26a shows the standard intensity versus scattering vector plot. The transition in slope highlighted by the dashed lines can be used to interpret the radius and thickness of the particle. Deschamps and De Geuser showed that the first transition point (q_1 in Figure 9.26) is related to the particle radius through $q_1 = \sqrt{2}/R$, where R is the particle radius, and the second transition point is related to the thickness through $q_2 = \sqrt{2}/t$, where t is the particle thickness.[26] As can be seen in the data from this experiment (Figure 9.25), the scattering curve does not flatten out to a constant value at low scattering vectors. This is due to the presence of the T phase. Transmission electron microscopy results confirm that the T precipitate has size features (100–200 nm) consistent with the length scales indicated by the low q scattering vectors shown in Figure 9.25.

Additional manipulation of the scattering curve is done by plotting $\ln(I)$ versus q^2, commonly called the Guinier plot (Figure 9.26b), and Iq^2 versus q, called the Kratky plot (Figure 9.26c). The slope of the low q linear portion of the Guinier plot (indicated by dashed line) can be used to determine the radius of gyration (R_g) of the particle from which the scattering occurs. The radius of gyration is related to the moment of inertia of an object and corresponds to a sphere that has the same moment of inertia as the particle being analysed.[20] For disc-shaped particles such as θ′ and Ω, the radius of gyration is related to the disc radius (R) and thickness (t) through

$$R_g^2 = \frac{R^2}{2} + \frac{t^2}{12} \qquad 9.2$$

The existence of the T phase in the sample makes a simple Guinier plot analysis difficult in these experimental materials, as the low q portion of the $\ln(I)$ versus q^2 curve does not have a distinct linear portion.

The Kratky plot can also be used to determine the volume fraction of particles by calculating the integrated intensity of the curve (Figure 9.26c, shown in the hatched area). The data collected during the experiment needs to be supplemented with estimations of the behaviour at close to zero and close to infinity. Dumont et al. demonstrated this method for the η phase in an Al-Zn-Mg alloy.[27] The integrated intensity Q_0 is represented by

$$Q_0 = \int_0^\infty I(q)q^2dq = 2\pi^2(\Delta p)^2 f_v(1-f_v) \qquad 9.3$$

where Δp is the difference in the density of scattering factors between the precipitate and matrix and f_v is the volume fraction. This proved successful for Dumont et al., as the η phase forms as a low aspect ratio platelet; however, in this experiment, the particles have a high aspect ratio (>5:1) and are not randomly oriented in the sample. Deschamps and De Geuser determined that

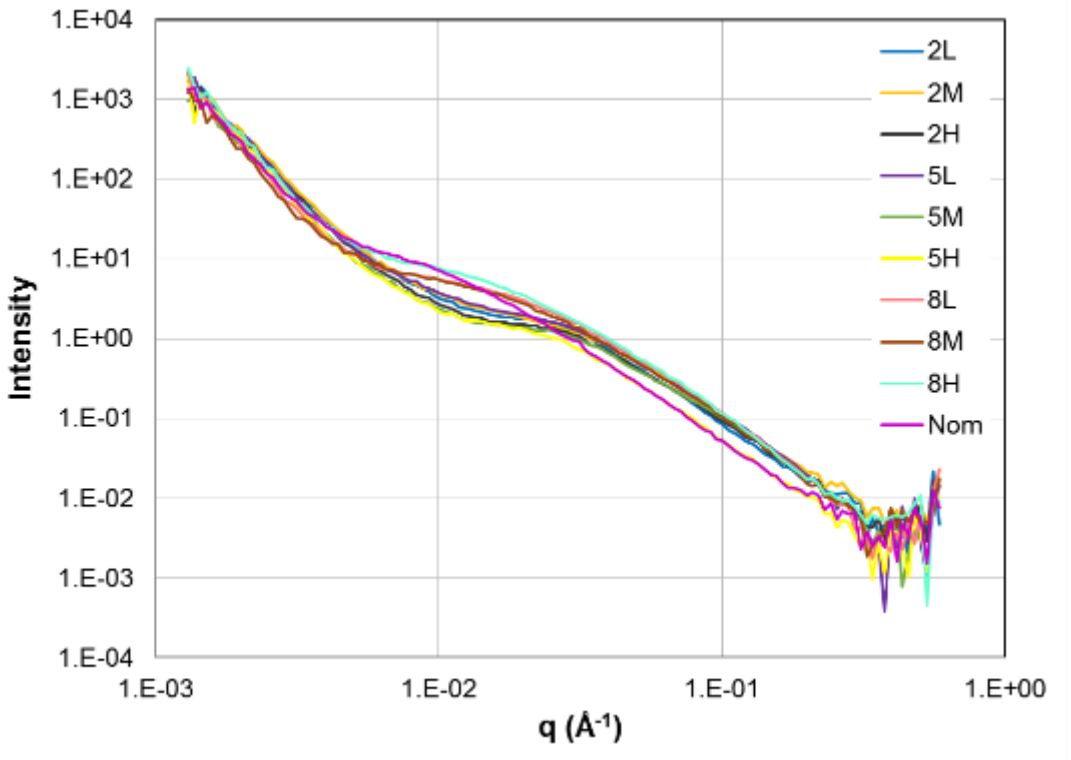

Figure 9.25: *Radially averaged, background-subtracted small-angle scattering data from each sample.*

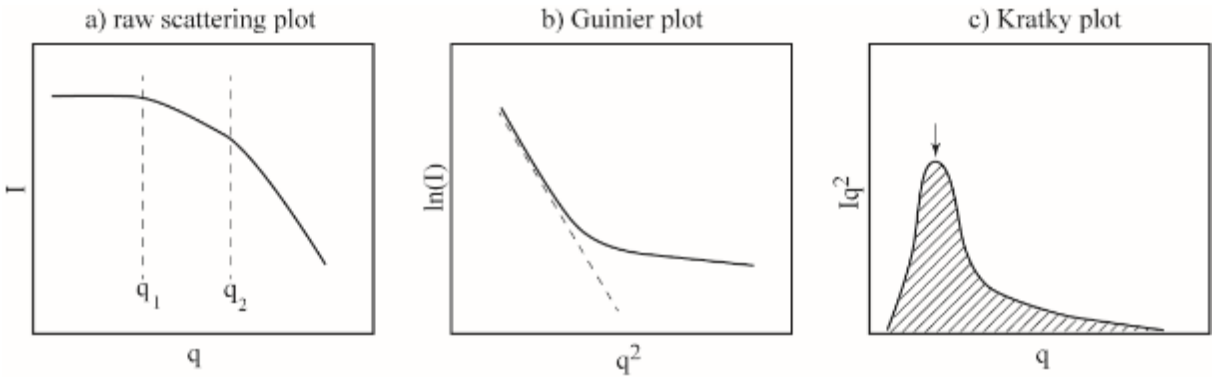

Figure 9.26: *Schematic representations of radially averaged small-angle scattering data. (a) Raw scattering plot, (b) Guinier plot, and (c) Kratky plot can be used to extract information about the particles being analysed.*

under these conditions (high aspect ratio and highly oriented particles), there is not a simple relationship between integrated intensity and volume fraction.[26] Unfortunately, the SANS method is not effective for calculating particle volume fraction in this experiment.

Due to the difficulty in calculating particle size using traditional plotting methods, a computer modelling program was used to analyse the SANS results from this experiment. SasView is a small-angle scattering analysis software package developed and managed by an international collaboration of small-angle scattering facilities.[28] This program allows the user to make informed predictions about the size and shape of the particle (e.g., by using transmission electron microscopy data). The software iteratively calculates the particle size features that best fit the chosen model constraints and the experimental data. Electron microscopy analysis from this experiment and from other documented experiments in this alloy show that the particles are high aspect ratio discs. SasView offers many fitting models, including ellipsoid and cylinder, the two most applicable to this material. Both fitting models were applied to a sample of the data using the Levenberg–Marquardt fitting algorithm (default for SasView). Levenberg–Marquardt is a method for fitting a function F(x) using

$$F(x) = \frac{1}{2}\sum_{i=1}^{m}[f_i(x)]^2 \qquad 9.4$$

By letting the Jacobian of $f_i(x)$ be $J_i(x)$, the Levenberg–Marquardt fitting method solves **p**

$$(J_k^T J_k + \lambda_k I)p_k = -J_k^T f_k \qquad 9.5$$

where λ_k are nonnegative scalars and I is the identity matrix. The cylinder model (in which the thickness of the disc corresponds to the length of the cylinder and the radius of the disc corresponds to the radius of the cylinder) proved to be the most accurate when compared to select particle measurements made from TEM micrographs for both samples 2H and 8H.

An example of the data and corresponding SasView model fit is shown in Figure 9.27. The blue markers are the experimental data, and the red line is the cylinder model fit. The model is truncated at the point where the T phase begins to shown a scattering effect ($q = 5 \times 10^{-3}$ Å^{-1}). This limits the SasView analysis to particles within the range of interest (10–100 nm) and avoids effects of the T phase that interfere with the model fit. The user assumes a particle shape and the model fits the data to that chosen shape. In this case, the chosen model shape was a cylinder. The model is able to determine both the particle radius and the particle thickness. There was a distinct variation in particle radius among the samples; however, there was not a variation in particle thickness. The particle thickness was determined to be in the 1–3 nm range for all the samples, which corresponds well to other particle measurement experiments

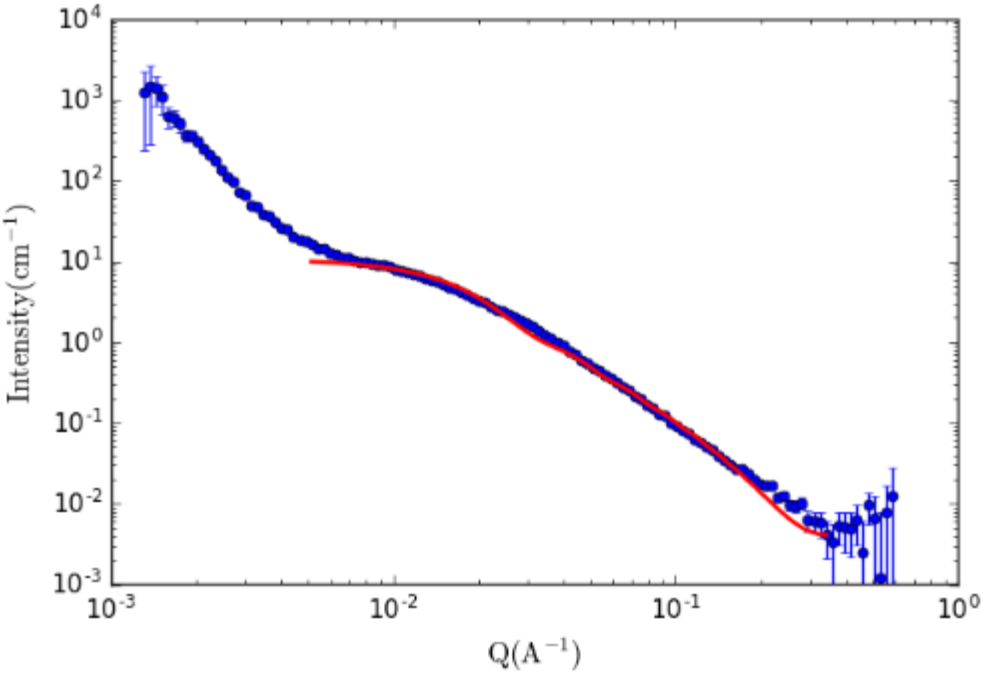

Figure 9.27: *Plot of experimental data (blue markers) for sample 8H and the corresponding cylinder model fit (red line) calculated using SasView software.*

documented in this alloy.[29-31] The entire dataset with duplicate measurements for each sample, fitting error (χ^2) and associated errors for both thickness and diameter are shown in Table 9.7.

The calculated particle diameter from the SANS data model fit is plotted in Figure 9.28 along with the microhardness measured for each sample. There is a clear correlation between Mg level in the deposit and the Ω and/or θ′ particle diameter. A similar trend is apparent for the Mg concentration and the microhardness. In general, as the Mg level decreases in the sample, the plate diameter decreases and the hardness decreases. This is a clear indication that Mg vaporization loss during the additive manufacturing process must be carefully monitored to ensure that the properties remain consistent.

Many researchers have discussed the critical Mg level in Al-Cu-Mg-Ag alloys at which the transition from θ′ phase on $\{100\}_\alpha$ planes to Ω on $\{111\}_\alpha$ planes occurs. Chester and Polmear showed that at 0.3 wt% Mg, the microstructure was dominated by Ω, while at 0.1 wt% Mg, very little Ω was present.[32] Gable et al. compared an alloy with 0.24 wt% Mg to an alloy with 0.1 wt% Mg.[12] While not quantified, TEM analysis showed that the 0.24 wt% Mg alloy

Table 9.7: *Tabulated results from SANS data model fit computed using SasView software.*

Cylinder model - Levenberg-Marquardt fit					Average				Average	
Sample		Length Å	Radius Å	χ^2	Thickness nm	Diameter nm	Length Error (Å)	Radius Error (Å)	Thickness Error (nm)	Diameter Error (nm)
8H	1	16.7	111.9	19.6	1.74	24.23	0.4	0.4	0.03	0.09
	2	18.1	130.4	22.3			0.2	0.5		
8M	1	15.1	101.0	13.7	1.29	19.76	0.3	0.5	0.08	0.09
	2	10.7	96.7	23.7			1.3	0.4		
8L	1	11.7	94.3	16.1	1.45	18.83	1.6	0.4	0.09	0.08
	2	17.3	94.0	15.7			0.2	0.4		
5H	1	18.7	75.8	2.1	2.05	14.97	0.4	0.6	0.06	0.11
	2	22.3	74.0	3.5			0.8	0.5		
5M	1	14.6	58.9	7.3	1.47	11.50	0.3	0.3	0.03	0.06
	2	14.8	56.1	7.8			0.3	0.3		
5L	1	11.2	68.6	9.4	1.28	12.80	0.3	0.3	0.03	0.06
	2	14.4	59.4	7.3			0.2	0.3		
2H	1	14.7	61.7	3.1	1.72	11.77	0.3	0.3	0.05	0.07
	2	19.7	56.0	6.2			0.6	0.3		
2M	1	16.1	63.7	9.2	1.31	12.52	0.7	0.3	0.14	0.06
	2	10.1	61.4	11.0			2.1	0.3		
2L	1	14.4	68.6	4.6	1.73	13.69	0.3	0.4	0.03	0.08
	2	20.2	68.3	4.0			0.3	0.4		
Nom	1	21.3	191.2	11.1	2.28	36.02	0.3	1.0	0.03	0.19
	2	24.2	169.0	14.4			0.3	0.9		

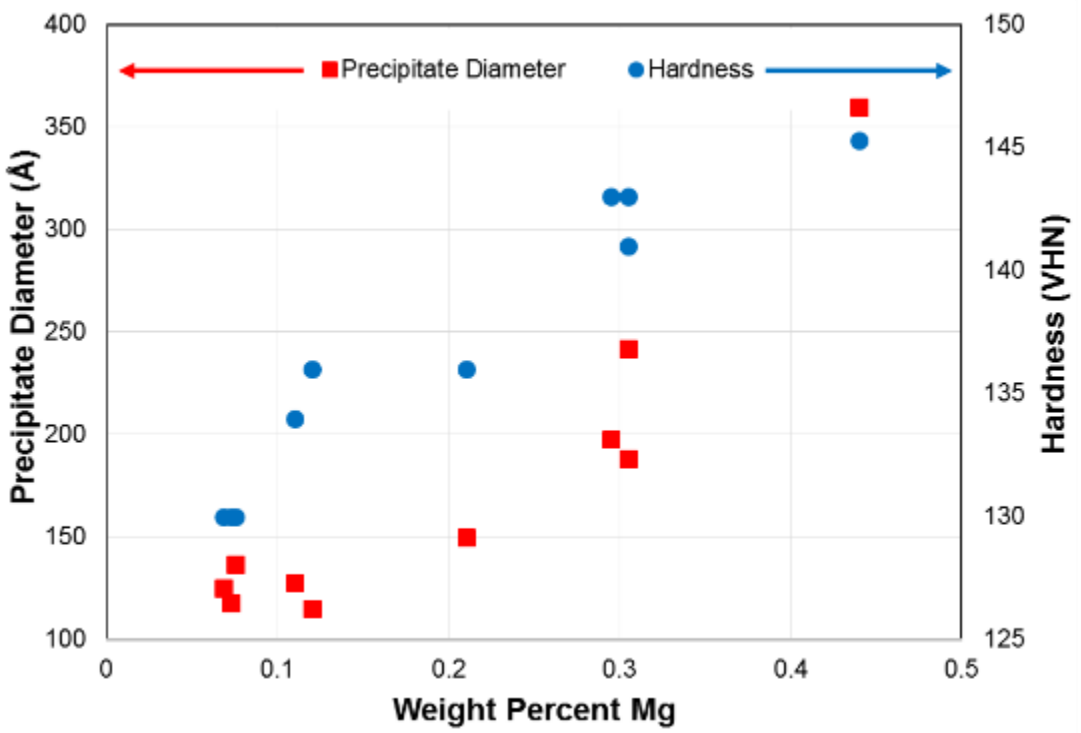

Figure 9.28: *Plot of precipitate diameter (left axis) and hardness (right axis) for each of the nine experimental deposited beads and the nominal (Nom) 0.5 wt% Mg baseplate material.*

had a much higher number density of Ω plates than the 0.1 wt % Mg alloy. Marceau et al. tied the critical composition to the quantity of Cu-Mg clusters formed upon quenching.[33] Again, the critical value was about 0.2 wt% Mg. Similar conclusions can be drawn from the current experiment. At Mg concentrations less than 0.2 wt%, the plate diameter is between 10 and 15 nm. With increasing Mg levels beyond 0.2 wt%, the plate diameter steadily increases all the way up to about 36 nm at a Mg level of 0.44 wt%.

Kang et al. calculated the habit plane variations in interfacial energy between the Ω and θ′ phases in Al-Cu alloys. On their own, the Ω precipitates on $\{111\}_\alpha$ and θ′ precipitates on $\{100\}_\alpha$ have interfacial formation energies of 2.12 eV nm^{-2} and 1.55 eV nm^{-2}, respectively. With these values, θ′ would be energetically favourable and the preferred precipitate; however, if an interfacial layer of 100% Mg is put between the matrix and the Ω precipitate on $\{111\}_\alpha$, the interfacial formation energy becomes −0.25 eV nm^{-2}. Sufficient Mg is therefore necessary

to provide an interfacial formation energy reduction between Ω and the matrix and favour the formation of Ω over θ′.

It has been well documented that Ag also plays a role in the interfacial layer between the precipitate and the matrix. Reich et al.,[34] Rainforth et al.,[35] and Murayama and Hono[36] all document a Mg:Ag ratio of 1 at the interface using atom probe tomography and nanobeam spectroscopy. Initially, the Mg and Ag form co-clusters at single vacancy sites upon quenching. The Cu then diffuses to these clusters and the precipitates begin to form. While Mg is necessary for the formation of Ω, Ag is not; however, the presence of Ag along with Mg greatly enhances the volume fraction of Ω. Vacancy trapping of Ag and Mg during quenching inhibits the formation of dislocation loops and suppresses θ′, which needs a defect structure on which to nucleate.[35] This vacancy trapping effect favours the formation of Ω in alloys with sufficient Mg and Ag. As Ag is much less volatile compared to Mg and it has a less critical influence on the formation of Ω, the Ag content was not measured or compared in this experiment.

Muddle and Polmear determined that the atomic misfit strain between the matrix and Ω precipitate in the direction normal to the $\{111\}_\alpha$ habit plane was about 9.3%, while parallel to the plane the misfit strain was only about 0.02%.[37] Similarly, Auld determined that the mismatch at the coherent interface was effectively zero.[38] This large difference in misfit strain favours the growth in the radial direction (parallel to $\{111\}_\alpha$) over growth in the thickness direction (normal to $\{111\}_\alpha$).

Additionally, Rosalie and Bourgeois showed that in Al-Cu alloys containing silver, the silver can segregate to the interface of the θ′ precipitates, both on the coherent surface in the habit plane and the semi-coherent lateral surface.[39] This Ag barrier inhibits Cu transport to the growing particle's edge and thus limits its radial growth. For Ω particles, however, it was shown by Hutchinson et al. that there is no interface species at the semi-coherent edge boundary.[40] Hono also showed similar result using atom probe tomography where it was clear that there

was no interface species adsorption at the semi-coherent edge; thus Ω is not growth-inhibited by an interfacial diffusion barrier. From these past studies it can be concluded that strain and interfacial energy favour thin and long Ω platelets over θ′ in Al-Cu-Mg-Ag alloys as long as there is sufficient Mg to reduce the interfacial energy at the Ω/α coherent boundary.

The SANS data presented in Figures 9.20 through 9.22 does not quantitatively distinguish between the phases present. There is no way to know whether the scattering contribution is from the θ′ phase or the Ω phase; however, Figure 9.24 does offer a qualitative assessment of the phases present based on the definitive streaking present in the 2D patterns. From this combined data we can conclude that the 2-series samples contain predominantly θ′ with little or no Ω. The low analysed Mg content of these deposited beads combined with the critical Mg level assessment from the literature support this conclusion. The 5-series samples have a mixture of both phases, though TEM and SANS data support the conclusion that the predominant phase is θ′. Again, this is supported by literature data suggesting a critical value of >0.2 wt% Mg is necessary to encourage Ω formation. The 5-series samples have Mg concentrations below 0.2 wt% with the exception of sample 5H, which had an Mg concentration of 0.21 wt%. The particle diameter plot in Figure 9.28 shows sample 5H is the point where the plate diameter starts to increase, indicating sufficient Mg for the formation of Ω. Finally, the 8-series samples have a significant fraction of Ω present, though there is still θ′ present as shown in the 2D scattering plots in Figures 9.20, 9.21, and 9.22. Fundamentally, as the Mg level increases, the energy barrier for precipitation on $\{111\}_\alpha$ planes is reduced to a point where it is less than that for precipitation on $\{100\}_\alpha$ planes, thus favouring Ω over θ′. The coherency mismatch at the particle/matrix interface in the $\{111\}_\alpha$ habit plane is effectively zero, driving growth in that plane and limiting thickening in the lateral direction.

9.7 Differential Scanning Calorimetry Results and Discussion

DSC has been used extensively in the characterization of precipitation-hardened aluminium alloys. Under ramp heating, a comparison of the differential heat flow from a small sample of the alloy to a pure control sample can yield information about the phases present and the various reactions that occur at specific temperatures. Specifically, endothermic reactions associated with particle dissolution and exothermic reactions associated with precipitation can be determined at specific temperatures as the sample is heated. The output from a DSC test is a thermogram showing heat flow versus temperature. Specific precipitate reactions can be identified by analysing the heat flows in the thermograms. Generally, a secondary method such as electron microscopy is used to determine exactly which heat flow peak corresponds to which particular precipitate phase. This is done by interrupting the scan after a particular exothermic peak and then conducting SEM/TEM examination of the sample to identify the precipitate. The alloy samples in this study have all been solution heat treated and aged to peak strength, so the DSC thermograms should first show dissolution of the main strengthening phase(s) and then precipitation of equilibrium phases. Because extensive DSC data exists in the scientific literature on Al-Cu alloys, the thermograms generated in this experiment will be correlated with established results from previous experiments.

The raw DSC data must first be corrected for background and transient heat capacity effects. These combined effects can be approximated by a linear function with respect to temperature.[41] A standard method for correction is to draw a line through two points on the thermogram curve where reactions are not known to occur and subtract that linear function from the overall thermogram. Once corrected for background/transient effects, the data must then be normalized such that relevant comparisons can be made from each sample. Dividing by sample weight, the resulting curve can then be plotted as normalized heat flow (W/g) as a function of

temperature (K). An example of the full correction procedure is shown in Figure 9.29 in which the raw data from sample 2L is shown along with the final corrected thermogram.

Thermogram plots for each of the nine deposited samples are shown in Figure 9.30. For clarity, each series is presented on its own individual graph. A negative heat flow indicates an endothermic reaction (heat flowing into the sample) and a positive heat flow indicates an exothermic reaction. The former is associated with particle dissolution reactions and the latter with precipitation reactions. Relative quantification is possible for single reactions with non-overlapping peaks by integrating the area under the curve for each reaction. This was not attempted due to the mixed nature of the phases (Ω and θ-type) present for each dissolution/precipitation reaction. The energy absorbed/released is presumably different for θ′ and Ω, and, since the curves for the reactions of these particles are not distinct, a reliable quantification cannot be made.

The 2-series thermograms were nearly identical, as can be seen in Figure 9.30a. The 5-series thermograms are similar but not identical. Note that the 5H thermogram is omitted, because the test did not capture a continuous, reliable signal. The 8-series thermograms are similar to each other but distinctly different from the other series. For comparison, the nominal condition (5-series baseplate) thermogram is shown in Figure 9.31. The nominal condition most

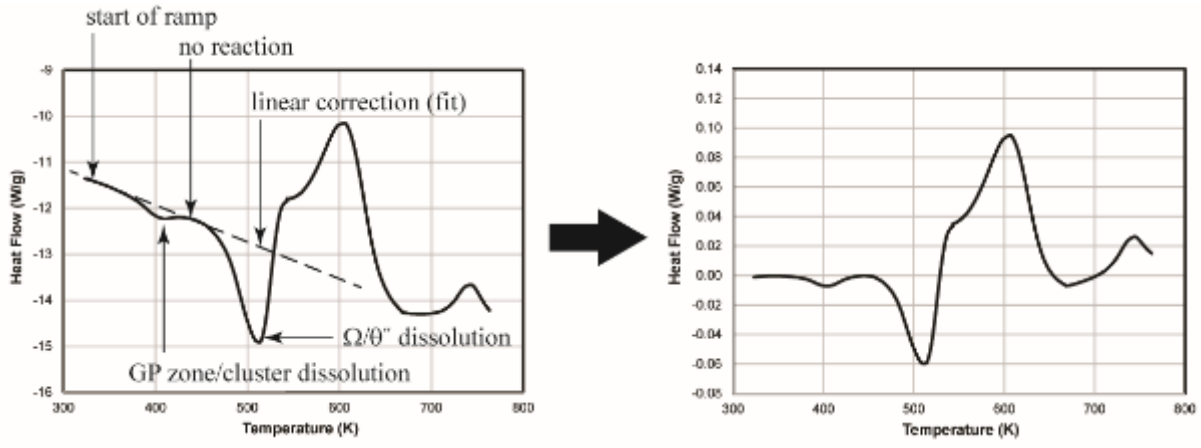

Figure 9.29: *Correction procedure for the raw thermogram data. A linear function is created from two points where reactions are not occurring (dashed line) and is then subtracted from the overall curve.*

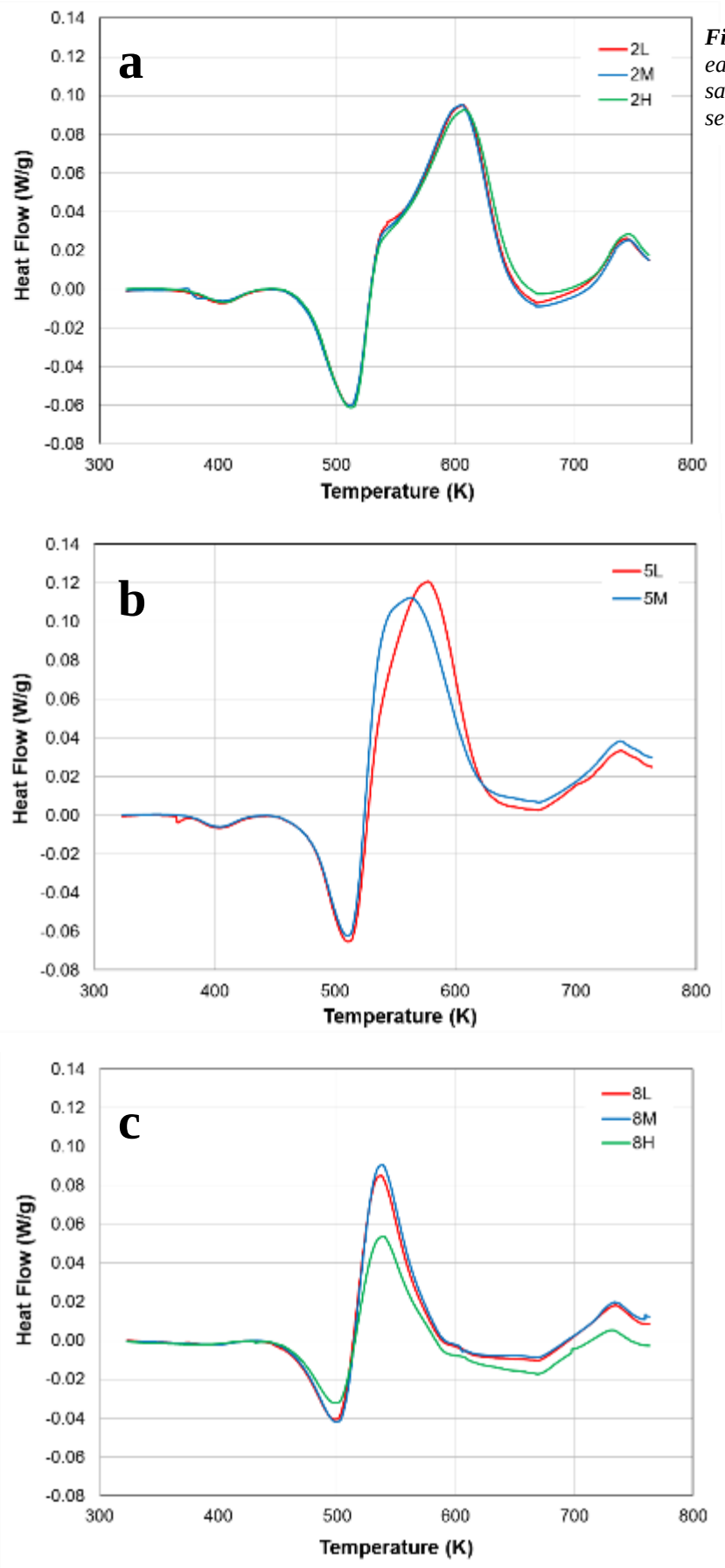

Figure 9.30: *Thermograms from each of the nine deposited bead samples: (a) 2-series samples, (b) 5-series samples, (c) 8-series samples.*

closely resembles the 8-series samples. Note that as the Mg level increases from the 2- to the 8-series, the thermogram of the deposited and heat treated material trends toward that of the 0.5 wt% Mg baseplate material.

For clarity, representative thermograms from each series (2L, 5L, and 8L) are plotted on one graph in Figure 9.32. The differences among the series are readily apparent when plotted together. The distinct thermal events are labelled "a" through "g" on the plot. The knowledge gained from the microscopy and SANS data helps with the interpretation of the first two endothermic dissolution peaks. Prior published DSC data from similar Al-Cu alloys is presented in Table 9.8 and also helps with reaction identification across the entire thermogram. It is worth noting that the heat rate has an effect on reaction peak temperature. This is driven by the kinetics of the process and can be different for different precipitate reactions within a given alloy system. Generally, a faster heating rate shifts the peak temperature higher, so it is worth noting that the temperature of the reaction peak in experiments with different heating rates may not exactly align.[42] The heating rate in this study was 20 K/min; the heating rates in the referenced published studies are listed in Table 9.8.

Peak "a" is present in the 2- and 5- series thermograms but is absent from the 8-series thermogram. The data from Papazian documents a GP zone dissolution reaction at about 420 K.[43] The endothermic reaction at point "a" has a peak at around 410 K, matching well with the data from Papazian. The 8L sample does not have the characteristic GP zone dissolution peak, suggesting a modified precipitation sequence. The established precipitation sequence for Al-Cu alloys is

$$\alpha \rightarrow GP\ zones \rightarrow \theta'' \rightarrow \theta' \rightarrow \theta$$

For Al-Cu-Mg alloys, the precipitation sequence may include the equilibrium S (Al_2CuMg) phase in alloys with Mg > 0.1 wt%:

$$\alpha \rightarrow co\text{-}clusters \rightarrow GP\ zones \rightarrow S' \rightarrow S$$

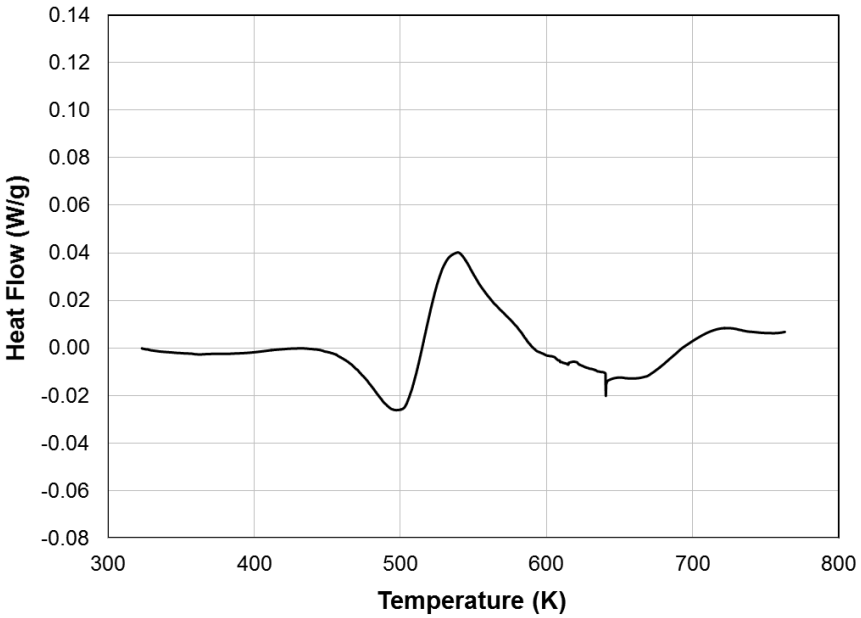

Figure 9.31: *Thermogram from the 0.5 wt% Mg baseplate material.*

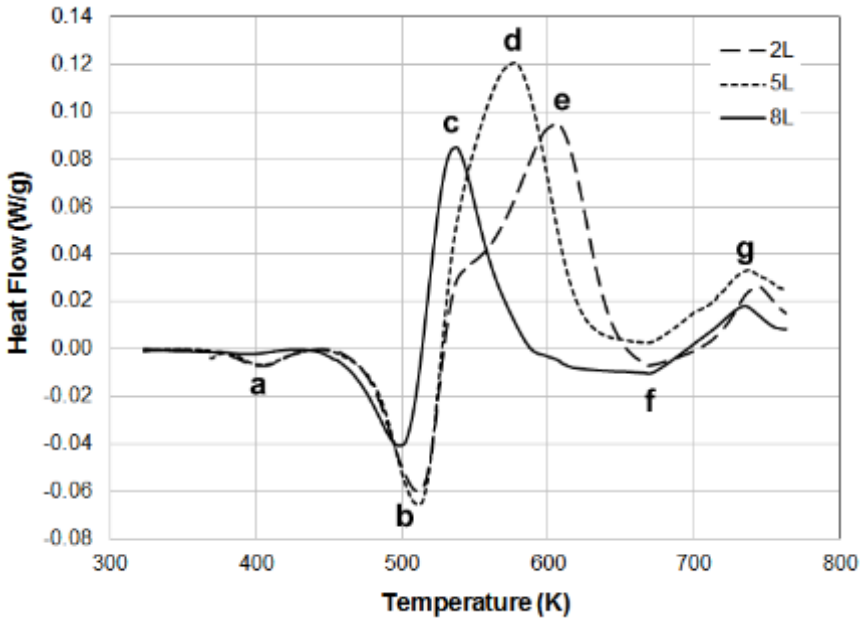

Figure 9.32: *Thermograms from each series (2L, 5L, and 8L) showing the distinct differences in the dissolution and precipitation behaviour.*

For Al-Cu-Mg-Ag alloys, the modified sequence is

$$\alpha \rightarrow co\text{-}clusters \rightarrow \Omega \rightarrow \theta$$

Magnesium, when present with silver, has been shown to form co-clusters at vacancy sites that limit the diffusion of Cu in the matrix.[44-46] This prevents GP zone formation and alters the precipitation sequence such that the Ω phase nucleates directly on the co-clusters. While Ω is

chemically invariant to θ (Al_2Cu), its habit plane is $\{111\}_\alpha$ versus $\{100\}_\alpha$ for the θ phase. It has been identified as a metastable phase and is eventually replaced by the stable θ phase under appropriate aging conditions.[38] The lack of a GP zone dissolution peak suggests that in sample 8L, the precipitation sequence is the modified one that includes Ω. This is further supported by prior work in this alloy that has shown that a minimum of 0.2 wt% Mg is required to promote the modified precipitation sequence.[33] In this study, the 8L sample had approximately 0.3 wt% Mg, while 5L had 0.1 wt% Mg and 2L had 0.08 wt% Mg.

The second endothermic peak (labelled "b" in Figure 9.32) is due to the dissolution of the major strengthening phase (Ω or θ-type). The peak-temperature location along with the maximum heat flow are distinctly different for sample 8L compared to those for 5L and 2L. This would indicate that the dissolving precipitate is different in 8L compared to the dissolving precipitate in the other two samples. Li and Shenoy have conducted DSC on a similar alloy composition and have identified a number of peaks.[30] They showed an endothermic peak at around 500 K (20 K/min heating rate) that they attributed to Ω phase dissolution. This corresponds very closely to the major endothermic peak in sample 8L. The relatively high Mg content in this sample (0.3 wt%) is enough to favour the formation of Ω through the modified precipitation sequence described above. In samples 5L and 2L, the major endothermic peak is shifted to a slightly higher temperature, approximately 515 K. It is assumed that this peak is due to θ″ dissolution. It is generally believed that θ″ forms directly from GP zones, while θ′ nucleates independently on defect structures such as dislocations. The fact that this material was not mechanically worked prior to aging suggests that θ′ should be suppressed due to lack of nucleation sites. This would lead to the conclusion that the thermogram peak at location "b" in Figure 9.32 for samples 2L and 5L is due to dissolution of θ″.

The most distinguishing difference among the three alloys lies in the 510–650 K range. The three exothermic peaks labelled "c," "d," and "e" in Figure 9.32 exhibit differences in peak location and temperature range of the reactions. Peak "c" in sample 8L can be correlated with work by Li and Shenoy, showing that this exotherm is due to combined θ′ and S′ (Al_2CuMg) precipitation. There is also agreement with published work by Jena et al.,[42] Shih et al.,[47] Charai et al.,[48] and Gao et al.[49] regarding the location of the S′ precipitation peak (between 550 and 570 K). The S′ phase is thermodynamically possible in the 8-series (0.3 wt% Mg) but not in the 2-series (<0.1 wt% Mg); thus, the exotherm curves for samples 2L (labelled "e" in Figure 9.32) and 5L (labelled "d" in Figure 9.32) cannot be due to S′ phase but are likely due to θ′. A study by Oguocha and Yannacopoulos documented the relative positions of both θ′ and S′ in a study of the precipitation behaviour of alloy 2618 (Al-2.3Cu-1.1Fe-1.5Mg-1.0Ni, in wt%).[50] They found that the S′ phase formed prior to the θ′ phase with the exotherm peak at 525 K for the former and 590 K for the latter. This shift is reflected in the position of peak "c" relative to "d" and "e." The earlier transition into the exothermic reaction is likely influenced by the S′ precipitation in the 8-series material and the lack of any S′ (and only θ′ phase) in the 2- and 5-series material.

Table 9.8: *Collected DSC data from similar alloys available in the research literature. The phase identification includes either a (P) for precipitation reaction or a (D) for dissolution reaction.*

Alloy	Condition	Phase	Temp K	Heating Rate K/min	Reference
Al-1.53Cu-0.79Mg	ST + age at 403 K for 6/12 hours	S′ (P)	570	10	Jena[41]
Al-1.53Cu-0.79Mg	ST + age at 403 K for 6/12 hours	S′ (D)	650	10	Jena[41]
Al-1.53Cu-0.79Mg	ST + age at 403 K for 6/12 hours	S′ (D)	670	20	Jena[41]
Al-2.62Cu-1.35Mg	ST + age at 463 K for 0.5 hour	S′ (P)	560	10	Shih[46]
Al-2.03Cu-1.28Mg	ST + age at 423 K for 96 hours	S′ (P)	560	20	Charai[47]
Al-5.1Cu-0.8Mg-0.5Ag-0.7Mn-0.13Zr	ST + age at 433 K for 16 hours	Ω (D)	500	20	Li[29]
Al-5.1Cu-0.8Mg-0.5Ag-0.7Mn-0.13Zr	ST + age at 433 K for 16 hours	θ′/S′ (P)	570	20	Li[29]
Al-6.2Cu-0.28Mn-0.2Fe-0.09V-0.06Ti-0.16Zr	ST + age at 463 K for 36 hours	θ′ (P)	550	10	Papazian[14]
Al-6.2Cu-0.28Mn-0.2Fe-0.09V-0.06Ti-0.16Zr	ST + age at 463 K for 36 hours	θ (P)	720	10	Papazian[14]
Al-6.2Cu-0.28Mn-0.2Fe-0.09V-0.06Ti-0.16Zr	ST + cold work	GP (D)	420	10	Papazian[42]
Al-2.73Cu-0.45Mg-0.42Mn	ST + age at 423 K for 24 hours	S′ (P)	550	10	Gao[48]

Peak “e” cannot be correlated with any particular phase in previously documented studies in the Al-Cu-X alloy systems. The only major difference in microstructure, beyond θ′ versus Ω content, is the presence of the mixed intermetallic eutectic product in the deposited bead. Recall that this intermetallic phase was present in the 2-series samples and to a lesser degree in the 5-series samples. With no other obvious microstructural difference between the samples, it is assumed that the peak labelled “e” is due to coarsening of these intermetallic phases. The peak at location “d” in sample 5L is then a combination of the θ′/S′ precipitation exotherm and the mixed intermetallic coarsening exotherm.

The absence of the intermetallic eutectic product phases in the 8-series samples can be correlated with the maximum temperature in the molten pool. The Hertz–Knudsen equation, which calculates the vaporization loss from the condensed phase to the gaseous phase, can be adapted to the AM process to provide a vaporization flux as a function of temperature (detailed discussion of this topic is provided in the following chapter). In this study the vaporization flux was measured using the analysed Mg content in the deposited bead and the bead geometry, as outlined in Chapter 10. With the Mg flux measured, the molten pool temperature can then be estimated using the Hertz–Knudsen equation. The estimated molten pool temperature is 1190 K in the 2-series, 1280 K in the 5-series, and 1370 K in the 8-series. Without knowing the exact intermetallic composition, it can be inferred that the eutectic reaction temperature is $1190\ K < T < 1370\ K$. This would explain the presence of the intermetallic phase in the 8-series baseplate, but lack of intermetallic phase in the 8-series deposited bead. The higher molten pool temperature in the 8-series allows the eutectic to dissolve, while the lower molten pool temperatures in the 2- and 5-series do not.

The broad dissolution trough indicated by location “f” in Figure 9.32 corresponds to dissolution of θ′ and S′. This is supported by prior work by Jena et al.[42] Finally, peak “g” is due

to nucleation of the equilibrium θ phase, common to all three alloys and the final reaction in the sequence prior to melting.

9.8 Summary and Conclusions

Single-bead deposits were made using three different aluminium alloy 2139 compositional variants. The Mg content was targeted at the composition minimum, nominal, and maximum values as allowed by the industry specification. All other solute elements were held constant. Single-bead deposits using these three alloy variants were made on their matching composition baseplates at three different temperatures. The temperature variation simulates the residual heat present in subsequent layers during multilayer deposition. The three compositions deposited at three unique temperatures resulted in a matrix of nine total samples.

Single-bead deposits were made using an electron beam wire directed energy deposition process. Beam-only, non-melting passes were used to preheat the baseplate, and the temperature was recorded using an attached thermocouple. The single-pass deposits were sectioned and prepared for metallurgical analysis using optical, scanning, and transmission electron microscopy; microhardness; small-angle neutron scattering; and differential scanning calorimetry.

The target compositions in two of the three wires were not met; however, there was enough Mg variation when the total of the deposited wire and re-melted baseplate was considered. The results of the analysis showed that the Mg concentration in the deposited beads is directly related to the microstructure and the properties. Below the 0.2 wt% Mg threshold, the microstructure is dominated by 12–14 nm diameter θ-type precipitates residing on $\{100\}_\alpha$ habit planes. Above the 0.2 wt% Mg threshold, the precipitates begin to change to the Ω phase. The Ω phase resides on the $\{111\}_\alpha$ habit planes and has a diameter between 15 and 35 nm, with the diameter increasing with increasing Mg content. This conclusion was validated by TEM, SANS, and DSC.

The hardness of the deposited material also shows a direct correlation to the Mg content. This conclusion supports prior studies in Al-Cu alloys which show that Ω is a more potent strengthener than θ. For peak performance out of additively manufactured 2139, the Mg level must be maintained above the 0.2% minimum value to ensure that the primary strengthening phase is Ω.

This study examined variations in both Mg content and variations in the baseplate temperature with single bead deposits made using aluminium alloy 2139. The goal was to document what effect Mg variation has on the deposited microstructure and measured properties. The critical Mg concentration was 0.2 wt% below which favoured the formation of θ-type precipitates while above which favoured the formation of the Ω phase. As Ω is the desired phase in 2139, it is critical to ensure that Mg vaporization loss during the process does not drive the Mg concentration below 0.2 wt%. It was found that underlying substrate temperature (100 K variation) has little effect on the Mg vaporization loss and subsequently little effect on the resulting microstructures and properties. For deposition processes using this alloy, it is critical to maintain a constant Mg vaporization rate such that the microstructure and properties are uniform within a given part.

A final comment regarding the applicability of these experimental results to actual conditions in additive manufacturing processes. Additive manufacturing uses multiple beads of material stacked in rows and layers. For full metallurgical bonding and defect-free structures, re-melting of subsequent beads is required. This re-melting causes additional vaporization and further dilution of the Mg content which is not addressed in this study. Additional work is necessary to fully understand realistic vaporization conditions in stacked bead configurations common in additive manufacturing processes.

References

1. SAE, AMS 4468 Aluminum Alloy, Plate 5.0Cu - 0.4Mn - 0.5Mg - 0.4Ag (2139-T84) Soution Heat Treated, Cold Worked, and Artificially Aged.

2. Brice, C.; Shenoy, R.; Kral, M.; Buchannan, K., Precipitation behavior of aluminum alloy 2139 fabricated using additive manufacturing. *Materials Science and Engineering: A* **2015,** *648*, 9-14.

3. Flemings, M. C., Solidification Processing. In *Materials Science and Technology*, Wiley-VCH Verlag GmbH & Co. KGaA: 2006.

4. Dehoff, R.; Kirka, M.; Sames, W.; Bilheux, H.; Tremsin, A.; Lowe, L.; Babu, S., Site specific control of crystallographic grain orientation through electron beam additive manufacturing. *Materials Science and Technology* **2015,** *31* (8), 931-938.

5. Thijs, L.; Kempen, K.; Kruth, J.-P.; Van Humbeeck, J., Fine-structured aluminium products with controllable texture by selective laser melting of pre-alloyed AlSi10Mg powder. *Acta Materialia* **2013,** *61* (5), 1809-1819.

6. Wei, H.; Mazumder, J.; DebRoy, T., Evolution of solidification texture during additive manufacturing. *Scientific reports* **2015,** *5*.

7. Cui, Y.; Xu, C.; Han, Q., Microstructure improvement in weld metal using ultrasonic vibrations. *Advanced Engineering Materials* **2007,** *9* (3), 161-163.

8. Mostafapour, A.; Gholizadeh, V., Experimental investigation of the effect of vibration on mechanical properties of 304 stainless steel welded parts. *The International Journal of Advanced Manufacturing Technology* **2014,** *70* (5-8), 1113-1124.

9. Talamantes-Silva, M.; Rodríguez, A.; Talamantes-Silva, J.; Valtierra, S.; Colás, R., Effect of solidification rate and heat treating on the microstructure and tensile behavior of an aluminum-copper alloy. *Metallurgical and Materials Transactions B* **2008,** *39* (6), 911-919.

10. Scott, V.; Kerry, S.; Trumper, R., Nucleation and growth of precipitates in Al–Cu–Mg–Ag alloys. *Materials Science and Technology* **1987,** *3* (10), 827-835.

11. Kerry, S.; Scott, V., Structure and orientation relationship of precipitates formed in Al-Cu-Mg-Ag alloys. *Metal science* **1984,** *18* (6), 289-294.

12. Gable, B. M.; Shiflet, G.; Starke Jr, E., Alloy development for the enhanced stability of Ω precipitates in Al-Cu-Mg-Ag alloys. *Metallurgical and Materials Transactions A* **2006,** *37* (4), 1091-1105.

13. Ringer, S.; Hono, K., Microstructural evolution and age hardening in aluminium alloys: atom probe field-ion microscopy and transmission electron microscopy studies. *Materials Characterization* **2000,** *44* (1), 101-131.

14. Papazian, J. M., A calorimetric study of precipitation in aluminum alloy 2219. *Metallurgical Transactions A* **1981,** *12* (2), 269-280.

15. Williams, D. B.; Carter, C. B., The transmission electron microscope. In *Transmission electron microscopy*, Springer: 1996; pp 3-17.

16. Chen, A.; Zhang, L.; Wu, G.; Peng, Y.; Li, Y., Effect of Mn addition on microstructure and mechanical properties of cast Al–2Li–2Cu–0.8 Mg–0.4 Zn–0.2 Zr alloy. *Journal of Materials Research* **2016,** *31* (2), 250-258.

17. Chen, Y.; Pan, S.; Liu, W.; Liu, X.; Tang, C., Morphologies, orientation relationships, and evolution of the T-phase in an Al-Cu-Mg-Mn alloy during homogenisation. *Journal of Alloys and Compounds* **2017,** *709*, 213-226.

18. Cahoon, J.; Broughton, W.; Kutzak, A., The determination of yield strength from hardness measurements. *Metallurgical and Materials Transactions B* **1971,** *2* (7), 1979-1983.

19. Davis, J., ASM Metal Handbook: Desk Edition. *ASM International* **1998**.

20. Cousin, F., Small angle neutron scattering. *EPJ Web of Conferences* **2015,** *104*, 01004.

21. Guinier, A., Structure of age-hardened aluminium-copper alloys. *Nature* **1938,** *142* (3595), 569-570.

22. Deschamps, A.; Garcia, M.; Chevy, J.; Davo, B.; De Geuser, F., Influence of Mg and Li content on the microstructure evolution of Al Cu Li alloys during long-term ageing. *Acta Materialia* **2017,** *122*, 32-46.

23. Deschamps, A.; Sigli, C.; Mourey, T.; De Geuser, F.; Lefebvre, W.; Davo, B., Experimental and modelling assessment of precipitation kinetics in an Al–Li–Mg alloy. *Acta Materialia* **2012,** *60* (5), 1917-1928.

24. De Geuser, F.; Bley, F.; Deschamps, A., A new method for evaluating the size of plate-like precipitates by small-angle scattering. *Journal of Applied Crystallography* **2012,** *45* (6), 1208-1218.

25. Glinka, C. Fundamentals of small angle neutron scattering 2004. https://www.ncnr.nist.gov/summerschool/ss04/information/SANS_tutorial.pdf (accessed October 3, 2017).

26. Deschamps, A.; De Geuser, F., Quantitative characterization of precipitate microstructures in metallic alloys using small-angle scattering. *Metallurgical and Materials Transactions A* **2013,** *44* (1), 77-86.

27. Dumont, M.; Lefebvre, W.; Doisneau-Cottignies, B.; Deschamps, A., Characterisation of the composition and volume fraction of η′ and η precipitates in an Al–Zn–Mg alloy by a combination of atom probe, small-angle X-ray scattering and transmission electron microscopy. *Acta Materialia* **2005,** *53* (10), 2881-2892.

28. SasView for small angle scattering analysis. http://www.sasview.org/ (accessed April 14, 2017).

29. Chang, Y.; Howe, J., In situ HRTEM study of Ω precipitate dissolution in an Al-Cu-Mg-Ag alloy. *Ultramicroscopy* **1993,** *51* (1), 46-63.

30. Li, Q.; Shenoy, R., DSC and TEM characterizations of thermal stability of an Al–Cu–Mg–Ag alloy. *Journal of Materials Science* **1997,** *32* (13), 3401-3406.

31. Knowles, K.; Stobbs, W., The structure of {111} age-hardening precipitates in Al–Cu–Mg–Ag alloys. *Acta Crystallographica Section B: Structural Science* **1988,** *44* (3), 207-227.

32. Chester, R.; Polmear, I., The metallurgy of light alloys. *Institution of Metallurgists, London* **1983**, 75.

33. Marceau, R.; Sha, G.; Ferragut, R.; Dupasquier, A.; Ringer, S., Solute clustering in Al–Cu–Mg alloys during the early stages of elevated temperature ageing. *Acta Materialia* **2010,** *58* (15), 4923-4939.

34. Reich, L.; Murayama, M.; Hono, K., Evolution of Ω phase in an Al–Cu–Mg–Ag alloy—a three-dimensional atom probe study. *Acta Materialia* **1998,** *46* (17), 6053-6062.

35. Rainforth, W.; Rylands, L.; Jones, H., Nano-beam analysis of Ω precipitates in a Al-Cu-Mg-Ag alloy. *Scripta Materialia* **1996,** *35* (2), 261-265.

36. Murayama, M.; Hono, K., Three dimensional atom probe analysis of pre-precipitate clustering in an Al-Cu-Mg-Ag alloy. *Scripta Materialia* **1998,** *38* (8), 1315-1319.

37. Muddle, B. C.; Polmear, I., The precipitate Ω phase in Al-Cu-Mg-Ag alloys. *Acta Metallurgica* **1989,** *37* (3), 777-789.

38. Auld, J., Structure of metastable precipitate in some Al–Cu–Mg–Ag alloys. *Materials Science and Technology* **1986,** *2* (8), 784-787.

39. Rosalie, J. M.; Bourgeois, L., Silver segregation to θ′(Al_2Cu)–Al interfaces in Al–Cu–Ag alloys. *Acta Materialia* **2012,** *60* (17), 6033-6041.

40. Hutchinson, C.; Fan, X.; Pennycook, S.; Shiflet, G., On the origin of the high coarsening resistance of Ω plates in Al–Cu–Mg–Ag alloys. *Acta materialia* **2001,** *49* (14), 2827-2841.

41. Starink, M., Analysis of aluminium based alloys by calorimetry: quantitative analysis of reactions and reaction kinetics. *International Materials Reviews* **2004,** *49* (3-4), 191-226.

42. Jena, A.; Gupta, A.; Chaturvedi, M., A differential scanning calorimetric investigation of precipitation kinetics in the Al-1.53 wt% Cu-0.79 wt% Mg alloy. *Acta Metallurgica* **1989,** *37* (3), 885-895.

43. Papazian, J. M., Calorimetric studies of precipitation and dissolution kinetics in aluminum alloys 2219 and 7075. *Metallurgical and Materials Transactions A* **1982,** *13* (5), 761-769.

44. Honma, T.; Yanagita, S.; Hono, K.; Nagai, Y.; Hasegawa, M., Coincidence Doppler broadening and 3DAP study of the pre-precipitation stage of an Al–Li–Cu–Mg–Ag alloy. *Acta Materialia* **2004,** *52* (7), 1997-2003.

45. Ferragut, R.; Dupasquier, A.; Macchi, C.; Somoza, A.; Lumley, R.; Polmear, I., Vacancy–solute interactions during multiple-step ageing of an Al–Cu–Mg–Ag alloy. *Scripta Materialia* **2009,** *60* (3), 137-140.

46. Somoza, A.; Petkov, M.; Lynn, K.; Dupasquier, A., Stability of vacancies during solute clustering in Al-Cu-based alloys. *Physical Review B* **2002,** *65* (9), 094107.

47. Shih, H.-C.; Ho, N.-J.; Huang, J., Precipitation behaviors in Al-Cu-Mg and 2024 aluminum alloys. *Metallurgical and materials transactions A* **1996,** *27*, 2479-2494.

48. Charai, A.; Walther, T.; Alfonso, C.; Zahra, A.-M.; Zahra, C., Coexistence of clusters, GPB zones, S ″-, S′-and S-phases in an Al–0.9% Cu–1.4% Mg alloy. *Acta Materialia* **2000,** *48* (10), 2751-2764.

49. Gao, N.; Davin, L.; Wang, S.; Cerezo, A.; Starink, M. J., Precipitation in stretched Al-Cu-Mg alloys with reduced alloying content studied by DSC, TEM and atom probe. **2002**.

50. Oguocha, I.; Yannacopoulos, S., Precipitation and dissolution kinetics in Al–Cu–Mg–Fe–Ni alloy 2618 and Al–alumina particle metal matrix composite. *Materials Science and Engineering: A* **1997,** *231* (1), 25-33.

10.0 VAPORIZATION ANALYSIS

10.1 Thermodynamics of Al-Mg Alloys

Basic vaporization concepts were introduced and discussed in Chapter 7. These concepts, derived from basic physics principles, have been adapted and applied to the study of vapour loss in a variety of fusion-based welding processes. Fusion-based additive manufacturing processes are analogous to welding and the vaporization concepts developed in the past can be adapted and applied to the study of vapour loss in AM processes. These concepts are useful for estimating the magnesium loss in alloy 2139 used in this study.

The magnesium flux in the alloy as a function of temperature can be calculated using the Hertz-Knudsen equation given in Chapter 7 (Eq. 7.1). This equation calculates the molar flux from the condensed phase to the gaseous phase and can be adapted to determine the Mg mass flux from the molten pool in the AM process. The equation must be multiplied by the atomic mass of Mg (M_{Mg}) to convert from molar to mass terms. It also must include the coefficient of evaporation (α_e) term. The mass flux of Mg from the molten pool is then:

$$J_{Mg} = \frac{\alpha_e M_{Mg} p^0_{Mg}}{\sqrt{2\pi M_{Mg} RT}} \qquad 10.1$$

The coefficient of evaporation accounts for the atoms that evaporate but re-condense back into the molten pool. For the analysis presented here, it is assumed that $\alpha_e = 0.85$ (see Section 7.2 for discussion) such that 85% of the vaporizing Mg atom truly escape the molten pool while 15% re-condense back into the liquid. The molecular weight (M_{Mg}) is 0.024305 kg/mol and the universal gas constant (R) is 8.31446 Pa-m^3/mol-K. Simplification of this equation yields

$$J_{Mg} = 1.833 \times 10^{-3} (p^0_{Mg}) T^{-1/2} \qquad 10.2$$

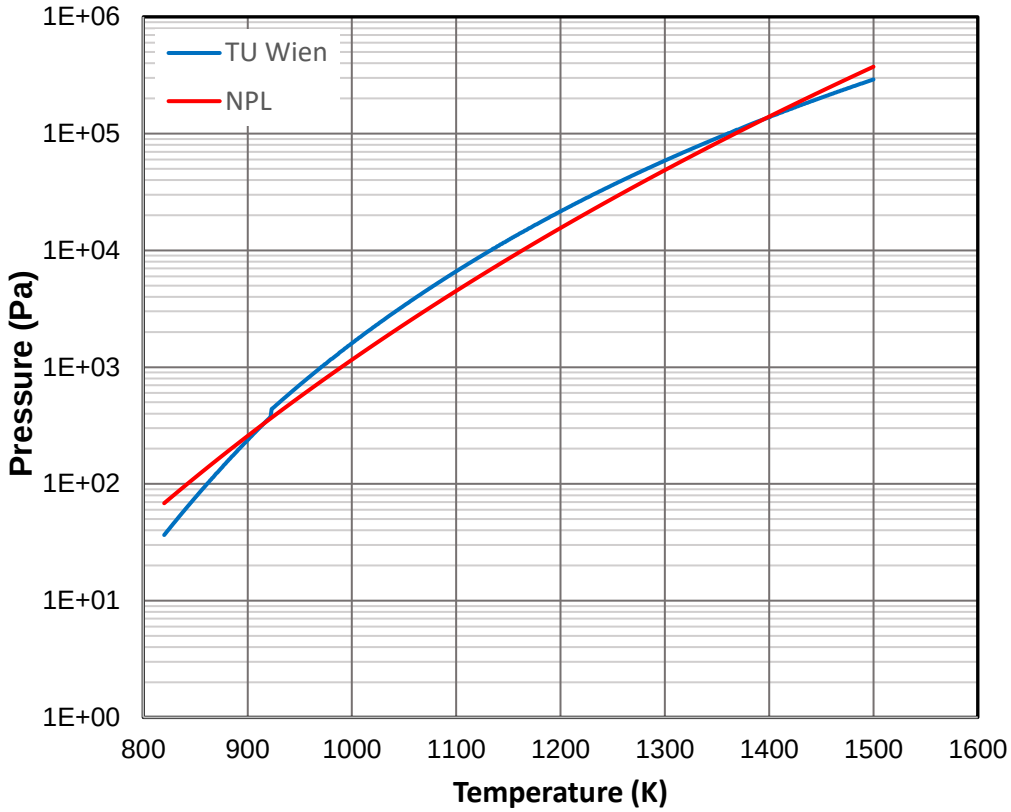

Figure 10.1: *Vapour pressure of pure magnesium over its condensed phase as a function of temperature from two different sources.*[1,2]

In Eq.. 7.1 the standard vapour pressure of the pure substance was used (P^0_{Mg}). For Mg in dilute alloy form, the partial vapour pressure of Mg over the alloy (p^0_{Mg}) must be used. This value is a function of temperature and can be computed using established thermodynamic relationships. With p^0_{Mg} given as a function of temperature, the mass flux of Mg vapour from the molten pool is then described purely in terms of temperature.

10.2 Vapour Pressure of Pure Magnesium

The vapour pressure as a function of temperature for most elements has been tabulated and is available from a number of sources. For the vaporization analysis here, two sets of data were selected for comparison; data by the TU Wien Institut für Angewandte Physik, Vienna, Austria,[1] and the Kaye and Laby Tables of Physical and Chemical Constants through the National Physical Laboratory, Teddington, United Kingdom.[2] The data from both sources show

very close agreement and are plotted in Figure 10.1. For calculation in this present work, the average value between these data sets is used.

10.3 Vapour Pressure of Magnesium in the Alloy

The vapour pressure over the pure substance is not directly useful in this study. However, it can be used to calculate the vapour pressure over the alloy using established thermodynamic relationships. In an ideal binary condensed solution, the partial pressure of the solute species over the condensed alloy phase (p_i) would be linearly related to the atomic fraction of the solute in the alloy (X_i)

$$p_i = X_i P_i \tag{10.3}$$

where P_i is the standard vapour pressure over the pure condensed substance. Ideal solutions assume there is no interaction between the atoms due to mixing and the value $\Delta H_{mix} = 0$. Rarely do mixtures exhibit ideal behaviour. For a general condensed solution, the partial pressure of the solute over the alloy is related to the partial pressure over the pure substance by the chemical activity (a_i), a measure of the effective concentration of a solute species under non-ideal conditions. Thus for a general condensed solution, Eq. 10.3 can be rewritten

$$p_i = a_i X_i \tag{10.4}$$

The activity is related to the concentration by the activity coefficient (γ_i)

$$a_i = \gamma_i X_i \tag{10.5}$$

The relationship between a_i and X_i is shown schematically in Figure 10.2. The straight line with a slope of 1 represents an ideal solution. Studies have shown that dilute Al-Mg alloys are thermodynamically non-ideal as the enthalpy of mixing is not zero.[3-5] The dark curved line is representative of a regular solution. Of particular importance to this work is the relationship at the dilute end of the curve since alloy 2139 has a nominal X_{Mg} of 0.0057 (mass fraction of Mg = 0.005). For dilute solutions, a_i/X_i is a constant value. This is known as Henry's Law and is shown by the straight dashed line in Figure 10.2.

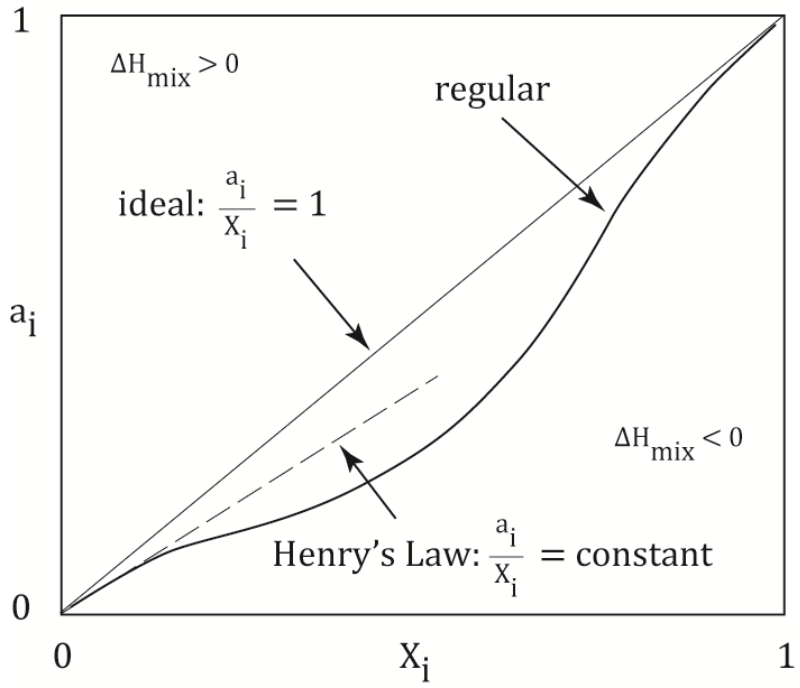

Figure 10.2: *Schematic showing relationship between the chemical activity (a_i) and the atomic fraction of the solute (X_i) at a fixed temperature.*

For a regular solution, the relationship between the activity (a_i) and the concentration of solute (X_i) is given by

$$RT\ ln\left(\frac{a_i}{X_i}\right) = \Omega(1 - X_i)^2 \qquad 10.6$$

where Ω is a temperature independent property called the interaction energy and is given by

$$\Omega = N_a z \varepsilon \qquad 10.7$$

where N_a is Avogadro's number, z is the number of bonds per atom, and ε is a factor relating bond energies.[6] The right hand side of Eq. 10.6 is constant for a constant solute composition. Substituting the relationship for a_i/X_i in Eq. 10.5 into equation 10.6 yields

$$RT\ ln(\gamma_i) = C \qquad 10.8$$

where C is a constant. If the value of γ_i is known at any particular temperature, the value of C can be calculated and used to determine the value of γ_i for any other temperature, in dilute solutions. Once the activity coefficient is determined as a function of temperature, the activity as a function of temperature can be calculated through the relationship in Eq. 10.5. Finally, the

Table 10.1: *Thermodynamic data for dilute Al-Mg alloy from Tiwari and Moser et al.*[6,7]

	T (K)	X_{Mg}	a_{Mg}	γ_{Mg}
Tiwari	1073	0.0055	0.0048	0.8780
Moser	1100	0.0052	0.0035	0.6705

partial pressure of the solute over the alloy as a function of temperature can then be calculated using Eq. 10.4.

Two studies have measured the thermodynamic properties of liquid Al-Mg alloys and have experimentally determined the activity of magnesium (a_{Mg}) in aluminum. Tiwari used a magnesium concentration cell to measure a_{Mg} in Al-Mg alloys using the emf method, with a particular focus on dilute alloys (< 10 at% Mg).[7] Moser et al. used three different methods to measure the thermodynamic properties of Al-Mg alloys, one of which was direct vapour pressure measurement using the Knudsen effusion method.[8] Both studies made measurements at Mg concentrations very close to the Mg concentration in aluminium 2139. Tiwari made a measurement at $X_{Mg} = 0.0055$ and Moser et al. made a measurement at $X_{Mg} = 0.00522$ (recall that in alloy 2139 $X_{Mg} = 0.0057$, nominal). The relevant data from both studies are shown in Table 10.1. Both studies concluded that Al-Mg alloys obey Henry's Law and show a slight negative deviation from ideal solution behaviour at low Mg concentrations (similar to the solid curved line shown schematically in Figure 10.2). These data can be used to estimate relevant thermodynamic properties for the alloy under investigation.

Using Eq. 10.8 and the data in Table 10.1, the constant (*C*) can be calculated for each data set. For the data from Tiwari, *C* = -1160.8 Pa-m^3/mol and for Moser et al. *C* = -3689.2 Pa-m^3/mol. Rearrangement of Eq. 10.6 yields

$$\gamma_i = exp\left(\frac{C}{RT}\right) \qquad 10.9$$

which allows the calculation of γ_i for any temperature. The activity can then be calculated using Eq. 10.5. Finally, the partial pressure over the alloy can be calculated using Eq. 10.4.

10.4 Vaporization Flux and Molten Pool Temperature

Returning to the simplified Hertz-Knudsen equation (Eq. 10.2), the mass flux of magnesium from the alloy molten pool can now be calculated as a function of temperature. Figure 10.3 shows a plot of the calculated results using Eq. 10.2 combined with the data analysis from Tiwari and Moser et al. in the temperature range 820 K to 1500 K. In a dilute Al-Mg alloy ($X_{Mg} \approx 0.005$), this relationship can be used to predict the mass vapour flux based on a known molten pool temperature, or conversely, the temperature of the molten pool based on a known mass vapour flux.

The vaporization flux was determined experimentally. For each of the nine samples described in Chapter 9, a small section of the deposit we extracted for chemical analysis. This sample was carefully cut such that it contained only material taken from the fusion zone of the bead as shown in Figure 9.6. Samples of the feedstock wire and baseplate for each of the three

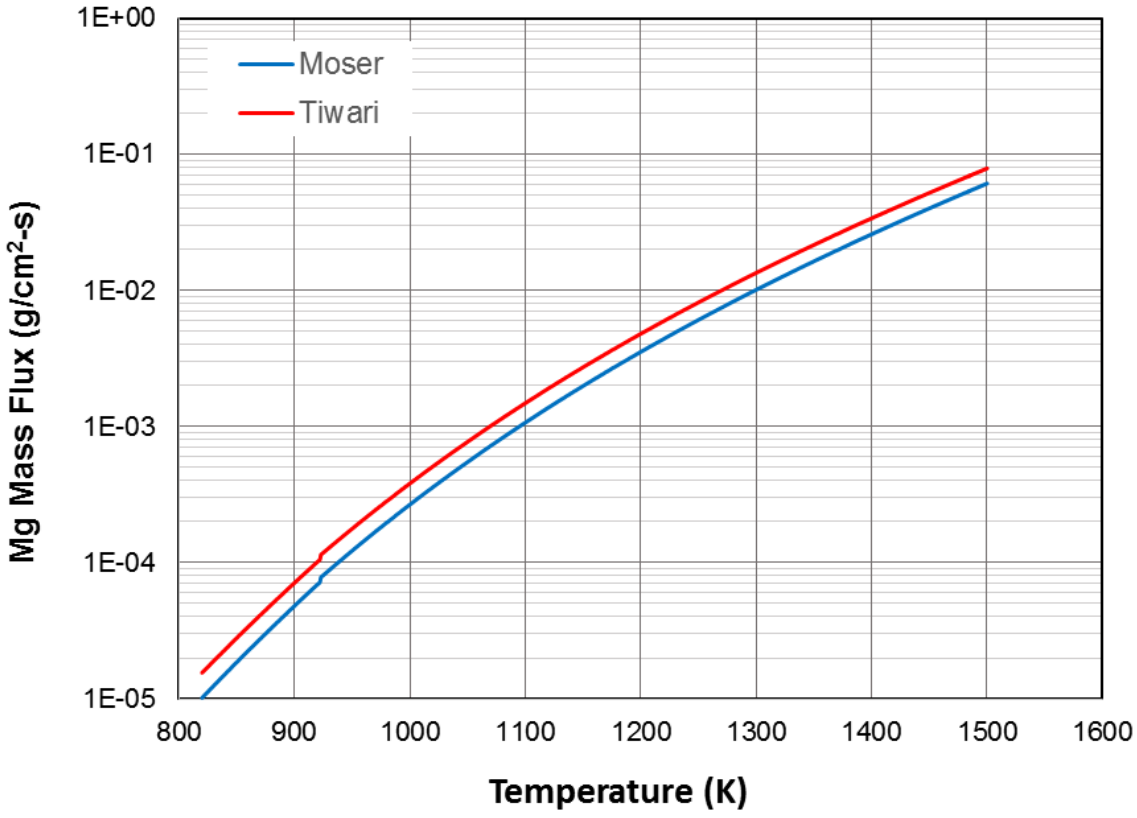

Figure 10.3: *Graph of magnesium vapour flux as a function of temperature for a dilute Al-Mg alloy. The curves were generated from thermodynamic data from Tiwari and Moser et al.*[6,7]

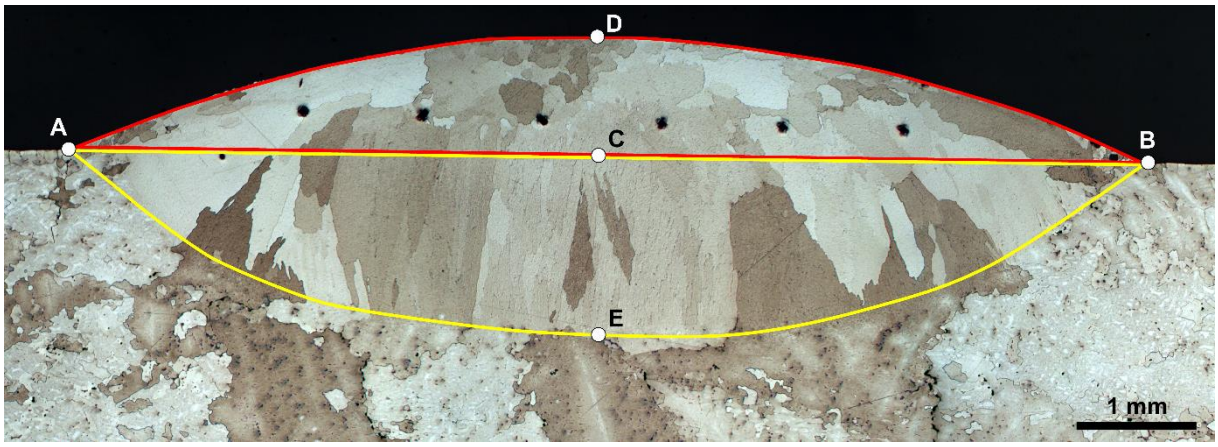

Figure 10.4: *Cross-sectional micrograph of specimen 8H showing areas and locations used for measurement. Refer to the text for a description of the various reference marks.*

experimental compositions were also analysed providing Mg concentration in the wire, the baseplate, and the deposited combination of the two.

Optical metallography was used to determine molten pool dimensions. Sample 8H is shown in Figure 10.4 along with reference notation used for the measurements. First, the cross sectional area of the deposited bead cap (highlighted by the red outline) and the fusion zone within the baseplate (highlighted by the yellow outline) were measured using ImageJ image analysis software. The deposited bead cap area (red area) divided by the total cross section area (red plus yellow areas) provides the fraction of the total fusion zone that is due to the wire. Likewise, the baseplate fusion zone area divided by the total area provides the fraction of the fusion zone that is due to re-melted baseplate. Assuming a constant bead cross-sectional profile, these area fractions are the same as the volume fraction of the deposited bead due to the wire feedstock versus re-melted baseplate. It is necessary to know these measurements since the wire and the baseplate have different analysed compositions. Additional linear measurements were taken and the results are shown in Table 10.2. The measurements, referenced back to the notation in Figure 10.4, are: “Total Height” is the distance between points D and E, “Crown Height” is the distance between points C and D, and “Width” is the distance between points A and B. Table 10.2 shows the result of the area measurements and also shows the calculation

Table 10.2: *Cross sectional measurements through each deposited bead.*

	Total cross section (mm^2)	Bead cross section (mm2)	% wire	% plate	Total Height (mm)	Crown Height (mm)	Width (mm)
8H	16.619	6.140	26.978%	73.022%	2.544	0.987	9.027
8M	13.998	5.975	29.915%	70.085%	2.325	1.033	8.576
8L	16.084	6.062	27.373%	72.627%	2.550	0.967	9.046
5H	18.415	8.364	31.233%	68.767%	2.723	0.868	8.485
5M	11.618	5.779	33.218%	66.782%	2.080	1.120	8.201
5L	11.698	5.566	32.241%	67.759%	1.934	1.046	8.008
2H	13.464	5.574	29.278%	70.722%	2.230	0.941	8.507
2M	12.441	5.898	32.161%	67.839%	2.087	1.067	8.287
2L	11.737	5.834	33.202%	66.798%	2.079	1.093	8.136

representing the percentage of fusion zone attributable to both the wire ("% wire") and the baseplate ("% plate"). On average, about 1/3 of the deposited bead volume was attributed to the wire feedstock and 2/3 of the deposited bead volume was attributed to re-melted baseplate.

The deposited bead measurements were used to calculate an estimated surface area of the molten pool. It was assumed that the molten pool had a spherical cap shape and that the flux came entirely from the pool surface and not from the molten wire before it enters the pool. This is a reasonable assumption as the wire feed directly into the molten pool creating a liquid metal bridge as opposed to discrete droplets forming and falling into the pool. Fitting a circle to the molten pool cap cross section (arc intersecting points A, D, and B in Figure 10.4) using ImageJ software showed that this assumption, at least in the cross-sectional view, was accurate. The surface of the deposited beads were also photographed and analysed. Figure 10.5 shows the photographed surface of sample 2M. A white circle is overlaid onto the image which allows for comparison against the solidification scallop marks, indicative of the molten pool shape. The circle shows close agreement to the scallop marks on the bead surfaces. Samples in the 2-series and 5-series were in very good agreement with the circle approximation. Samples in the 8 series deviated slightly in that the trailing edge of the molten pool was very slightly teardrop shaped.

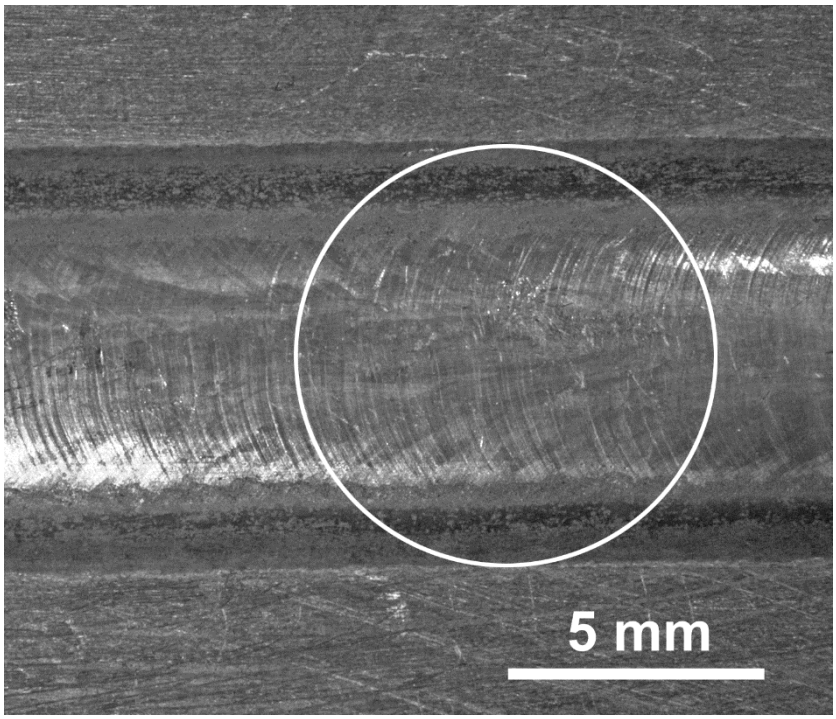

Figure 10.5: *Optical photograph of bead 2M looking down on the surface. A circle is overlaid on the image to compare with the solidification scallop marks, justifying the assumption that the molten pool is circular.*

While the shape was not quite circular, the measured surface area was essentially the same. Thus a circular approximation was used for all the samples.

The equation for the surface area of a spherical cap (A_{cap}) was used to approximate the surface area of each deposited bead

$$A_{cap} = \pi(r^2 + h^2) \qquad 10.10$$

where r is the radius of the cap (distance between points C and B in Figure 10.4) and h is the height of the cap (distance between points C and D in Figure 10.4).[9] The surface area for each bead is shown in Table 10.3.

The surface area and total cross-sectional area increase with increasing Mg content. The 2 series of samples has the smallest molten pool while the 8 series has the largest. These samples all received the same energy input so the difference in the molten pool size and shape must be due to the Mg content, the only variable between the sample series. With the exception of sample 8L, the surface area also increases with the amount of preheat provided to the baseplate

Table 10.3: *Estimated molten pool surface area, measured mass loss (using equation 10.11), calculated mass vapour flux, and estimated temperature of the molten pool.*

	Molten Pool Surface Area (cm^2)	Mass Loss (g)	Flux (g/cm^2-s)	Est. Temp (K)
8H	0.6706	1.841	0.0233	1378
8M	0.6112	1.585	0.0220	1371
8L	0.6721	1.781	0.0225	1374
5H	0.5891	0.538	0.0078	1261
5M	0.5676	0.607	0.0091	1277
5L	0.5380	0.657	0.0104	1291
2H	0.5962	0.263	0.0037	1192
2M	0.5751	0.242	0.0036	1188
2L	0.5574	0.202	0.0031	1174

prior to deposition. This is expected since the residual heat in the baseplate provided by the preheat passes reduces the amount of beam energy needed to reach melting. The excess beam energy (preheat versus no preheat) goes toward increasing the molten pool superheat and growing the dimensions of the molten pool.

Each deposited bead composition, as determined by plasma spectroscopy, was used to calculate a solidus and liquidus temperature with Thermo-Calc, a thermodynamic calculation tool from Thermo-Calc Software, Solna, Sweden. A phase equilibrium calculation was done for each deposit and each baseplate composition. This calculation predicted phase fraction at any temperature and the liquidus and solidus temperatures. The solidus and liquidus temperature results are shown in Figure 10.6. Increasing Mg content lowers the solidus temperature. The difference between solidus temperature at the minimum Mg content (0.2 wt%) and the maximum Mg content (0.8 wt%) is 18 K. The larger molten pool in the higher Mg content material can be attributed to the reduced solidus temperature. For a given power input from the electron beam, a composition with a higher Mg content will have a larger molten pool as there is less energy required to achieve melting.

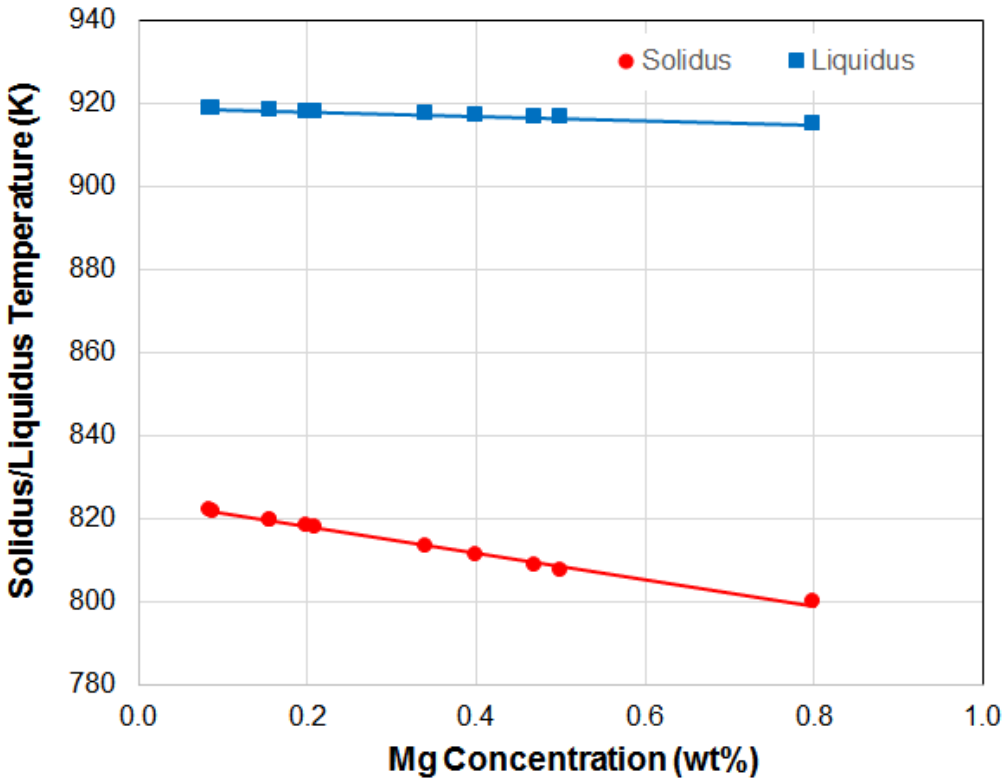

Figure 10.6: *Thermo-Calc calculated solidus and liquidus temperature for each deposited bead as a function of magnesium content.*

An additional factor affecting the molten pool size is the surface tension of the alloy. Garcia-Cordovilla et al. showed that increasing Mg concentration in Al-Mg alloys led to a reduction in the liquid surface tension in air.[10] The effect was small – 2% lower for a 0.8 wt% Mg alloy compared to pure aluminium. Comparing the crown height measurement (distance between C and D in Figure 10.4) shows that the 8-series had the shortest crown height, indicative of a lower surface tension. The measurement comparisons are shown in Table 10.2.

Results from the chemical measurements are shown in Table 10.4. Each bead was measured for Mg only while a sample from each of the three wires and three baseplates were measured for all alloying constituents. The target Mg concentration in the wires and baseplates were not met. In particular, there were essentially only trace amounts of Mg in the two wires that were targeted to have 0.2 wt% and 0.5 wt% Mg. It is uncertain what caused this discrepancy. Two possible scenarios can be speculated upon. First, during the casting process

Table 10.4: *Analysed Mg content in the deposited beads, feedstock wires, and the baseplates.*

	Mg % Deposit	Mg % Wire	Mg % Plate	Nominal Mg %	Loss
8H	0.305	0.670	0.710	0.699	56.4%
8M	0.295	0.670	0.710	0.698	57.7%
8L	0.305	0.670	0.710	0.699	56.4%
5H	0.210	0.037	0.440	0.314	33.1%
5M	0.120	0.037	0.440	0.306	60.8%
5L	0.110	0.037	0.440	0.310	64.5%
2H	0.073	0.038	0.185	0.142	48.9%
2M	0.069	0.038	0.185	0.138	50.3%
2L	0.075	0.038	0.185	0.136	44.9%

the Mg was not fully incorporated into the melt. During the melting operation, the casting was visually inspected throughout the melting process using a sight glass on the furnace. Once the casting charge was fully molten and convection in the liquid melt was apparent, the induction current was lowered and the melt was held for at least 10 minutes. While it was assumed that there was adequate convection in the melt to fully stir the composition, it was never verified within the casting. It is possible there are large chemical gradients in the processed castings which led to chemical gradients in the wire. The deposition experiment only used a small length of wire (≈ 65 cm used out of a total of 21,000 cm wire produced from the ingot) and it is possible the Mg is concentrated in other parts of the wire due to casting segregation. The second possibility is that the Mg vaporized during the casting process. The casting furnace was pumped down to a hard vacuum prior to melting, however, it was backfilled with argon gas to a pressure of 76 MPa prior to melting. If the superheat put into the melt was sufficiently high, the Mg could have vaporized during the melting process. The lack of adequate Mg in the two low Mg wire compositions is unfortunate; however, it does not invalidate the experiment. Since there was Mg at near the expected levels in the baseplate, the combination between the two did result in an adequate difference in total Mg content between the three sets of deposited beads.

In Table 10.4, the "Nominal Mg %" is the sum of the Mg content in the wire multiplied by the percentage of the cross-sectional area attributable to the wire and the Mg content in the baseplate multiplied by the percentage of the cross-sectional area attributable to the baseplate (from Table 10.2, "% wire" and "% plate"). This is the theoretical Mg content if there was zero vaporization loss and all the Mg from both the wire and the baseplate were thoroughly mixed in the fusion zone. The "Mg Deposit %" is the actual measured composition of the deposited bead. The difference between the theoretical nominal Mg content and the actual measured Mg content can be used to calculate a percentage loss of Mg. This value is approximately between 30% and 60%, depending on the Mg concentration and thermal conditions. This is quite a bit lower than the approximately 80% Mg loss in the alloy 5356 deposit analysed in Chapter 8. However, the deposited bead in the 5356 trial had an expected nominal Mg concentration of 1.5 wt%. The higher Mg concentration is responsible for the higher vaporization loss.

The experimentally determined Mg vaporization loss in the deposited bead can be used to calculate the mass flux during the deposition process. Section 7.7 discussed the additive manufacturing specific equation previously developed by Mukherjee et al.[11] (Eq. 7.5) that can be used to predict vaporization flux. This equation calculates the vapour flux using mass loss, process travel speed, bead length, and molten pool surface area. The mass loss (ΔM_{Mg}) was determined by taking the volume of the bead (cross-sectional area [*CA*] multiplied by the total bead length [L]) and multiplying that by the change in Mg concentration (Δm_{Mg}) as determined by plasma spectroscopy. This yields the mass of Mg lost in the deposited bead in grams.

$$\Delta M_{Mg} = (CA)(L)\Delta m_{Mg} \tag{10.11}$$

Multiplying the mass loss by the travel speed (*TS*, in cm/s) and dividing by the bead length (in cm) and the surface area (*SA*, in cm^2) yields a vaporization flux in g/cm^2-s.

$$J_{Mg} = \frac{\Delta M_{Mg}(TS)}{L(SA)} \tag{10.12}$$

For this experiment the travel speed, TS, was 0.85 cm/s.

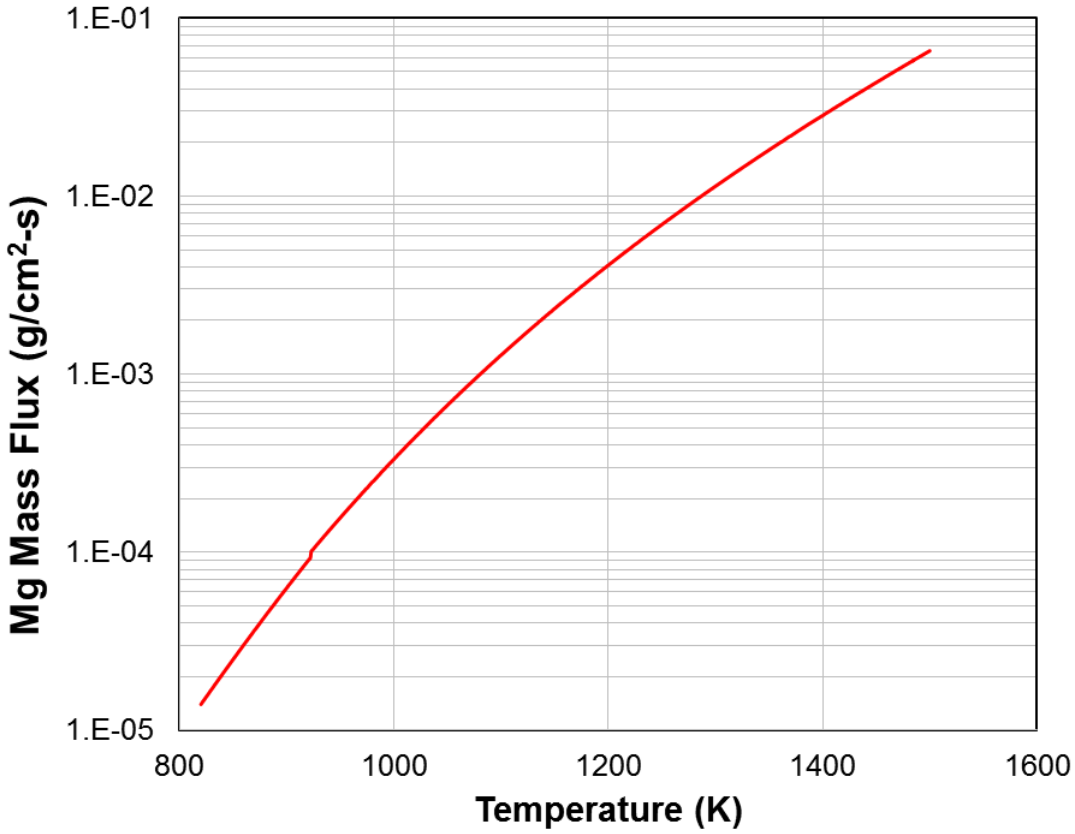

Figure 10.7: *Mass flux versus temperature for the average of data from Tiwari and Moser et al.*

The experimentally determined mass vapour flux can then be used to estimate a molten pool temperature using the relationship in Eq. 10.2. This relationship is plotted in Figure 10.7 for flux in the temperature range of 800 K to 1500 K. The corresponding results for each of the nine experimental samples is shown in the "Est. Temp" column in Table 10.3. As the change in Mg content was measured from the entire bead, the estimated temperature is the average temperature of the molten pool. The temperature variations within the molten pool surface could not be predicted in this experiment. The nominal composition of the alloy has an effect on the vaporization flux at constant beam power and correspondingly, has an effect on the molten pool temperature. The temperature variation between the low Mg samples (2-series) and high Mg samples (8-series) was about 200 K, with the higher Mg concentration predicting a higher molten pool temperature.

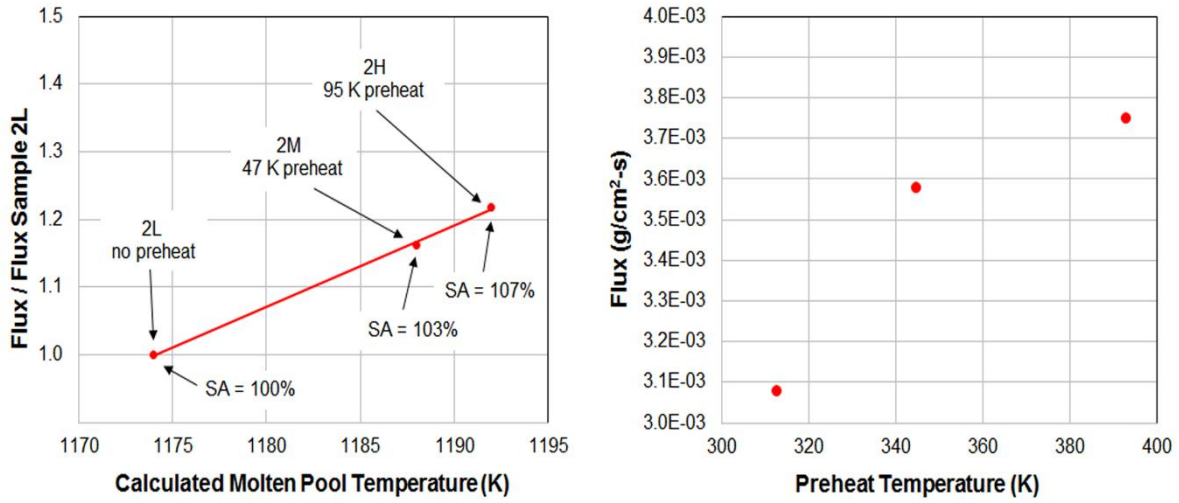

Figure 10.8: *Left: Flux increase as a function of temperature for the 2-series samples. 2L had no preheat, 2M had 47 K of preheat, and 2H had 95 K of preheat. Surface area of the molten pool is shown as "SA" with 2L being the baseline for comparison against 2M and 2H. Right: Effect of preheat temperature on the flux in sample series 2.*

10.5 Discussion

Analysis of the 2-series data showed an expected trend. The preheat added to the substrate plate resulted in slightly larger molten pool surface area along with a corresponding increase in Mg flux. This is shown in Figure 10.8. This behaviour is expected because the residual heat from the preheat passes lowers the amount of energy required to form a stable molten pool during the deposition pass. Since the input beam energy is constant between each of the samples, the extra energy for the preheated samples goes toward increasing the molten pool size and temperature. In Figure 10.8, the label "SA" represents the surface area as measured and calculated from the actual samples. Fluxes and surface area are normalized to the values for 2L (with no preheat). Sample 2M, with 47 K of preheat, had flux rate increase of 1.16 over 2L and a 103% larger surface area. Sample 2H, with 95 K of preheat, had a flux rate increase of 1.22 over 2L and a 107% larger surface area. The calculated molten pool temperature range over the three samples was only 18 K. This small of a temperature range would be very difficult to use as a process control feedback. The level of accuracy in the measurement would have to

be a few degrees Kelvin which might be achievable in a stationary configuration but would be very challenging for a dynamic process, such as additive manufacturing.

A study conducted by Schauer et al. used an infrared pyrometer to study the molten pool temperature in electron beam welded aluminium alloys.[12] The experiment was configured to probe various locations within the molten pool. The peak pool surface temperature was located the bottom of the weld pool cavity in a partial penetration keyhole mode weld while the perimeter of the pool was considerably cooler. The peak temperature in alloy 2024 (1.5 wt% Mg) was 1970 K ± 100 K and in alloy 5083 (4.5 wt% Mg) 1520 K ± 100 K. These temperatures are significantly higher than what was calculated for this experiment, however, they are peak and not average temperatures. The average will be significantly less assuming the molten pool temperature distribution is Gaussian. Schauer et al. did not calculate an average molten pool temperature; however, analysis of their plotted data approximates that for the alloy 7075, the average surface temperature is 1220 K ± 50 K. This is comparable to the calculated temperatures in these experiment. However, as stated above, a control strategy that uses molten pool temperature measurement as a reference would have to have a very stable signal. As Schauer et al. have shown, the variation in temperature across the molten pool is significantly greater than a few Kelvin. In fact, the measured peak temperature is almost 2000 K but varies out to the edge of the pool to the solidus temperature (about 800 K) right at the liquid/solid interface. Any temperature measurement made in real-time during the deposition process would have to be highly targeted in a specific location of the molten pool and the location could not vary as the process progresses. This seems like an extremely difficult challenge, but could be possible with the right configuration, such as where the sensor rides along with the heat source such that the probe is always pointed directly into the moving molten pool. A more reasonable approach would be to make a broad measurement over the entire molten pool and average the

temperature. This would likely be less susceptible to measurement noise induced by process variation.

A key conclusion from Schauer et al. was that volatile alloying elements significantly reduced the measured molten pool peak temperatures. They conducted an experiment where the peak temperature was measured while the beam was traversing across two different aluminium alloy plates. One plate was alloy 1100 with no volatile solutes and the other was alloy 7075 with two highly volatile solutes (2.5 wt% Mg and 5.5 wt% Zn). The peak molten pool temperature in the alloy 1100 section was about 2270 K. Crossing into the alloy 7075 area, the peak immediately drops to 1700 K, a change of over 500 K. The key conclusion is that the vaporization of volatile elements reduces the molten pool temperature through evaporative cooling. It is clear that changes in vaporization loss from volatile solutes can have an impact on measured molten pool temperature; however, the subtle differences that are of primary interest in this study (a few tenths of a percent change in Mg) would be more challenging to measure.

Similar conclusions were reached by Block-Bolten and Eager.[13] They studied evaporative loss in arc-based welding processes using a variety of aluminium alloys with volatile solute elements. Vaporization is greatly reduced in arc-based processes due to the atmospheric pressure environment (versus vacuum environment in the Schauer et al. study). They concluded that vaporization of volatile elements from the molten pool resulted in power loss due to evaporative cooling. This cooling process sets an upper limit on the surface temperature in welding/deposition processes. The power loss is small, however, which supports a conclusion that the evaporating species are re-condensed in the cooler regions (near the edges) of the molten pool. This justifies the use of the coefficient of evaporation (α_e) in Eq. 10.1 for the calculation of flux versus temperature in this experiment. However, it also reinforces the conclusion that there are large variations in the temperature of the molten pool surface and

repeatable measurements for use in a process control strategy would have to be extremely precise.

The other two series of samples (5 series and 8 series) did not follow the expected trend of increasing vaporization loss and increasing molten pool size with increasing levels of preheat into the plate. There were two significant anomalies within these two groups of material. First, sample 5H had a unique and unusual deposited bead appearance and behaved differently than all the other samples during deposition (see Figure 9.11 and 9.12 for optical images of 5H). The bead crown did not conform to the typical spherical cap shape seen in the other samples and the overall appearance was non-uniform over the bead length and very "lumpy". This sample also had different microstructural features. There was significant porosity in the cross section and the grain structure was much finer and less oriented. As discussed in Chapter 9, it is speculated that the baseplate material for this sample was non-uniform and had local segregation and significant solidification porosity (in the as-cast baseplate material). These defects caused the unstable molten pool and sparking seen during deposition and made it difficult to get accurate measurements of the bead surface area and cross section. The analysed Mg content was also higher in this sample which could be a result of the non-uniform composition in the baseplate casting.

Sample 8L also showed anomalous behaviour. The ambient temperature sample should have a smaller molten pool cross section due to the overall lower level of heat input. However, in this sample the dimensions (both cross section and bead cap) where nearly identical to sample 8H, which was deposited with 90 K of preheat supplied to the baseplate. These two samples were almost identical in their bead geometry and in the amount of Mg vaporized during deposition. The sample in the middle (8M) showed approximately 15% smaller overall cross-sectional area and approximately 9% reduction in surface area. Yet this sample showed about the same amount of Mg vaporization loss. The reason for the abnormally large molten pool in

8L can only be speculated upon. It is possible that there was unstable beam power during the deposition process. The exact cause is unimportant as it has no impact on the overall conclusion. The difference in Mg concentration within the three different series of samples is very small – on the order of 0.01%. The summary conclusion with regard to preheat in the baseplate is that it does not impact the overall vaporization rate of Mg, at least within the 90 K range investigated in this study.

The conclusion above is supported by the hardness data presented in Chapter 9. The changes in composition in the 2-series samples appears meaningful when plotted in Figure 10.8, however, the measured hardness of the three samples was identical. Ultimately this study seeks to understand the sensitivity of vaporization losses on the microstructure and mechanical properties of the deposited material. In this regard, a 20% increase in vapour flux between sample 2L and 2H is insubstantial with regard to the resulting material mechanical behaviour. In the 5 series and 8 series samples, the largest difference in hardness was 2 VHN. Using the approximated tensile strength calculation shown in Chapter 9, the difference in strength is about 6 MPa, or 1.4%. This level of sample-to-sample variation is not uncommon in conventionally processed materials such as castings and forgings.

From the welding literature there is a comprehensive study that closely matches the work performed here. Cieslak and Fuerschbach characterized Mg vaporization loss in Mg-bearing aluminium alloys processed via laser welding.[14] They studied three alloys with various Mg content: 5456 at 5.1 wt% Mg, 5086 at 4.0 wt% Mg and 6061 at 1.0 wt% Mg. Spot and linear bead welds were made using a pulsed and continuous Nd:YAG laser. Optical metallography was used to determine the fusion zone volume and the surface area of the molten pool was assumed to be circular. Electron microprobe analysis was used to characterize the Mg content in the weld fusion zone. In their analysis, Mg was the only alloying constituent to vaporize during welding and there were a number of process-related effects that determined how much

Table 10.5: *Comparison of magnesium composition and flux ratios between the three families of experimental material. The Average Nominal Composition is the expected Mg concentration in each deposited bead assuming no Mg vaporization loss.*

Target Composition (wt% Mg)	Average Nominal Composition (wt% Mg)	Composition Ratio	Average Flux (g/cm^2-s)	Flux Ratio
0.8	0.699	5.0	0.01680	6.1
0.5	0.310	2.2	0.00815	2.9
0.2	0.139	1.0	0.00278	1.0

Mg would vaporize. First, slower welding speeds increased the amount of vaporization. Since flux is a time dependent quantity, the dwell time for a given volume of material as the heat source moves determines how much Mg will vaporize. Similarly, the number of pulses in a spot weld affected the Mg vaporization. Increasing the number of pulses increased the Mg loss, but it was not linear. The rate of change decreased as the number of pulses increased. The concentration of Mg in the molten pool determines the flux rate and as the concentration decreases, so does the flux. This connection is through the partial vapour pressure of Mg over the alloy (p_{Mg}^0) which decreases with decreasing concentration (Eq. 10.4).

Cieslak and Fuerschbach used the simplified Hertz-Knudsen equation (Eq. 10.2) to estimate molten pool temperature in their weld beads. They assumed a regular solution model that obeyed Henry's Law and that the other alloying constituents had negligible effect on the activity coefficient of Mg. They estimated a molten pool surface temperature of about 1100 K to 1200 K depending on alloy Mg concentration (1.0 wt% for alloy 6061 up to 5.0% for alloy 5456), assuming vacuum conditions. Their results align very closely with the results documented in this experiment.

Cieslak and Fuerschbach draw a correlation between vapour loss and concentration using two different alloys welded at the same travel speed. The ratio of the Mg concentration between the alloys 6061 and 5456 is 1:5. The measured flux between these alloys welded using the same travel speed was 1:6. In the current study, a similar trend is seen. Averaging the nominal Mg

content (weighted average of wire and baseplate Mg content) for each series of samples and comparing the average flux within each series yields a very similar ratio. The average nominal Mg composition for the 8 series samples is five times greater than for the 2 series samples. The corresponding measured flux rate is 6.1 times greater in the 8 series than in the 2-series. The results for all three sets of compositions is shown in Table 10.5.

While the hardness difference between the samples in each individual series was insignificant, the hardness difference between each series was substantial. From the lowest Mg to the highest (as measured in the deposited bead) the hardness difference was about 13 VHN which corresponds to an approximate tensile strength difference of 40 MPa, or 10%. This difference in hardness is due to a 0.23 wt% difference in Mg content. Recall that the alloy specification allows the composition for vary between 0.2 wt% and 0.8 wt%, a 0.6 wt% range. While a deposited part with Mg that varies within that range would be acceptable according to the specification for the alloy, it would not be acceptable to have a part with such a large variation in chemistry. As shown here, even a change of around 0.2 wt% would result in 25-30 MPa variation in the part tensile strength. In this study it was shown that under varying thermal conditions there was little change in the overall amount of Mg vaporized for a given composition of wire. Significant differences were only seen for deposits made with different starting compositions. If it is assumed that a given feedstock wire is uniform in composition, under the conditions demonstrated here there would be no major difference in deposited chemistry in a given part.

Previous work by the author on electron beam directed energy deposition of aluminium 2139 was referenced in detail in Chapter 6.[15] This work used similar alloy composition wire and plate (uniform nominal Mg content of 0.52 wt%) and processed it using similar Sciaky electron beam deposition equipment. The deposited sample was multiple layers thick totalling about 1.5 cm in height. Slices taken at the bottom, middle and top of the deposit showed Mg

vaporization losses of 63%, 69%, and 79% respectively. These values are considerably higher than the single pass deposits studied in this experiment and the percentage loss increases with increasing layer height. Comparing these two experiments, it would appear that the analysis of single bead deposits does not fully represent the actual conditions during multi-layer deposition.

A comparison was performed on the Mg loss from the previous experiment using the hardness and strength relationships developed in this study. Table 10.6 shows the results where the "Top", "Middle", and "Bottom" corresponds to the locations in the multi-layer deposit. The "Hardness" value is calculated using the linear relationship between Mg content and hardness developed in Chapter 9. Likewise, the ultimate tensile strength ("UTS") was estimated using the linear relationship between hardness and strength developed in Chapter 9. As mentioned above, the variations in Mg were purely process induced and not due to variation in the feedstock wire Mg concentration. The variation is 0.08 wt % Mg, about eight time higher than the variation that was seen within the individual composition series in this experiment (0.01 wt% Mg). While the variation was significantly greater, the effect on the calculated hardness and estimated strength was small. The estimated variation between the top and bottom samples is 12 MPa or about 2.8%. Whether this is an acceptable level of variation within a part depends on the level of criticality for that particular part. However, this variation is quite low and shows that the sensitivity of the mechanical properties to the Mg concentration is not substantial, as long as the concentration is above the 0.2 wt% Mg critical limit.

Table 10.6: *Past Mg vaporization data from EBDED 2139 by Brice et al. compared using the linear fit for hardness and the calculated estimate of tensile strength developed in this study.*

	wt% Mg	**Hardness VHN**	**UTS MPa**
Top	0.11	132.7	422.8
Middle	0.16	135.2	430.3
Bottom	0.19	136.7	434.8

One final comment can be made on the sensitivity of strength to Mg content. The variation in Mg levels between the 2 series baseplate and the 8 series baseplate is about 0.53 wt%. This is baseplate material only – no re-melting or deposition occurred in these samples. The measured hardness in the 2-series and 8-series is 108.7 and 166.3 HVN, respectively. Applying the same calculated linear relationship between hardness and strength shows 350 MPa for the 2-series baseplate and 525 MPa for the 8-series, a 33% difference. This is very significant and this level of variation would likely be unacceptable in any single deposited part.

Other work by the author on EBDED of aluminium alloy 2319 showed that the baseplate can reach temperatures as high as 500 K during multi-pass deposition.[16] The preheat applied in this experiment did not exceed 400 K. So while this study was valuable in examining the vaporization effects in the process, it does not fully encompass the actual processing window. Further experiments at higher soak temperatures would be valuable.

10.6 Summary and Conclusions

The vapour pressure of magnesium was determined using empirical relationships established by two different sources. For this study, the results were averaged to give a temperature dependent vapour pressure of Mg over the pure substance. This relationship was used to calculate the partial pressure of Mg of the alloy. The Mg partial vapour pressure over the alloy was determined using two published studies that evaluated Al-Mg alloys of similar concentration to this work. The results from the two studies were in close agreement and were averaged for use in the present study. Both studies determined that Al-Mg alloys followed the regular solution model and at low Mg concentrations obeyed Henry's Law. It was assumed that the other alloying elements had a negligible effect on the activity of Mg in the alloy, an assumption supported by Cieslak and Fuerschbach.

The partial pressure of Mg over the alloy was then used in the Hertz-Knudsen equation to develop a relationship between the mass vapour flux and the temperature of the molten pool.

Vacuum conditions were assumed and the evaporation coefficient was chosen to be 0.85, indicating 85% of the vaporizing atoms escape to the gas phase while 15% re-condense elsewhere in the molten pool. The mass vaporization flux was calculated using the experimentally determined Mg loss in the deposited bead and the estimated molten pool surface area. For each sample, a molten pool temperature was calculated using the Hertz-Knudsen relationship and the calculated Mg mass flux rate. The predicted average temperature values agree well with prior work in the welding literature.

The flux and predicted temperatures within each individual series (no preheat, low preheat, and high preheat) did not vary significantly. While there was an expected trend in the 2-series samples (increasing preheat also increases the molten pool surface area and overall flux), the other two series of samples showed no definitive trend. The small change in predicted molten pool temperature of around 18 K would not be a useful control metric.

The flux and predicted temperatures did vary considerably across the three series of samples. From this result, it is clear that a large compositional variation on the order of 0.1% would lead to an easily measureable temperature difference in the molten pool and a large variation in mechanical strength.

In summary, this experiment showed that differences in the temperature of the underlying material (up to about 100 K) did not have a major effect on the vaporization loss or the hardness of the deposited material. Controlling the additive manufacturing process to maintain a certain temperature range should limit the amount of property variation seen within a given part. This experiment, however, did not explore the substrate temperature variations higher than 100 K and previous work in the literature has shown that substrate temperatures can vary by twice that for multi-bead, multi-layer deposition in aluminium. For conditions where the Mg content might vary by more than 0.1 wt%, the property variation would be unacceptable within a single part. In this situation, the average temperature of the molten pool could be monitored and used

to control the heat input into the process and minimize vaporization flux changes throughout the build.

References

1. Vapor Pressure Calculator. https://www.iap.tuwien.ac.at/www/surface/vapor_pressure (accessed July 17, 2017).

2. Vapour Pressures. http://www.kayelaby.npl.co.uk/chemistry/3_4/3_4_4.html (accessed July 17, 2017).

3. Lukashenko, E.; Pogodaev, A., Thermodynamics of melts with aluminum, magnesium, and zinc. *Russian Journal of Physical Chemistry* **1971,** *45* (8), 1182.

4. Tsyplakova, M.; Strelets, K. L., Study of the thermodynamic properties of the magnesium-aluminum system by the emf method. *Journal of Applied Chemistry, USSR* **1969,** *42* (11), 2354-2359.

5. Bhatt, Y.; Garg, S., Thermodynamic study of liquid aluminum-magnesium alloys by vapor pressure measurements. *Metallurgical Transactions B* **1976,** *7* (2), 271-275.

6. Porter, D. A.; Easterling, K. E.; Sherif, M., *Phase Transformations in Metals and Alloys, Third Edition (Revised Reprint)*. CRC Press: 2009.

7. Tiwari, B. L., Thermodynamic properties of liquid Al-Mg alloys measured by the Emf method. *Metallurgical Transactions A* **1987,** *18* (9), 1645-1651.

8. Moser, Z.; Zakulski, W.; Rzyman, K.; Gasior, W.; Panek, Z.; Katayama, I.; Matsuda, T.; Fukuda, Y.; Iida, T.; Zajaczkowski, Z., New thermodynamic data for liquid aluminum-magnesium alloys from emf, vapor pressures, and calorimetric studies. *Journal of phase equilibria* **1998,** *19* (1), 38-47.

9. Harris, J. W.; Stöcker, H., *Handbook of mathematics and computational science*. Springer Science & Business Media: 1998.

10. Garcia-Cordovilla, C.; Louis, E.; Pamies, A., The surface tension of liquid pure aluminium and aluminium-magnesium alloy. *Journal of Materials Science* **1986,** *21* (8), 2787-2792.

11. Mukherjee, T.; Zuback, J.; De, A.; DebRoy, T., Printability of alloys for additive manufacturing. *Scientific reports* **2016,** *6*.

12. Schauer, D.; Giedt, W.; Shintaku, S., Electron beam welding cavity temperature distributions in pure metals and alloys. *Welding Journal* **1978,** *57* (5), 127s-133s.

13. Block-Bolten, A.; Eagar, T., Metal vaporization from weld pools. *Metallurgical Transactions B* **1984,** *15* (3), 461-469.

14. Cieslak, M.; Fuerschbach, P., On the weldability, composition, and hardness of pulsed and continuous Nd: YAG laser welds in aluminum alloys 6061, 5456, and 5086. *Metallurgical Transactions B* **1988,** *19* (2), 319-329.

15. Brice, C.; Shenoy, R.; Kral, M.; Buchannan, K., Precipitation behavior of aluminum alloy 2139 fabricated using additive manufacturing. *Materials Science and Engineering: A* **2015,** *648*, 9-14.

16. Brice, C. A.; Hofmeister, W. H., Determination of bulk residual stresses in electron beam additive-manufactured aluminum. *Metallurgical and Materials Transactions A* **2013,** *44* (11), 5147-5153.

11.0 SUMMARY AND CONCLUSIONS

11.0 Project Summary

Additive manufacturing (AM) is an emerging fabrication method capable of producing high-performance components with reduced cost and lead time. Applications for aluminium alloy AM components has lagged other higher performance alloys (e.g., titanium and nickel) for two major reasons. First, the cost of AM-produced aluminium components is less competitive compared to traditional product forms (e.g., machined from plate), reducing the business case for adoption. Second, high-performance wrought aluminium alloy compositions are difficult to process using AM methods. Wrought alloys are often difficult to weld (and thus difficult to fabricate with fusion-based AM methods), and they often require mechanical work to achieve peak properties after heat treatment. These two factors limit the applicability of most wrought aluminium alloy compositions in AM processes. Most current work in aluminium AM has focused on casting compositions such as AlSi10Mg.

Aluminium alloy 2139 is a wrought alloy that is well suited for AM processing. It is a fusion-weldable composition and does not require mechanical work to achieve peak aged strength. The critical solute additions are Mg and Ag, which promote co-cluster formation on quenched-in vacancies. These clusters provide nucleation sites for Ω precipitates (Al_2Cu parallel to the $\{111\}_\alpha$ habit planes). Without Mg or Ag, mechanical work would be necessary to create the dislocation network necessary for nucleation of the θ phase (Al_2Cu parallel to the $\{100\}_\alpha$ habit planes). Because the Ω precipitates reside on the $\{111\}_\alpha$ habit planes and these planes are the preferred planes for dislocation slip, the strengthening increment for Ω is higher than for θ; thus, in alloy 2139, precipitate nucleation occurs on uniformly distributed co-

clusters, and the precipitates grow on the $\{111\}_\alpha$ habit plane. This results in high tensile strength in the solution heat treated and aged condition.

For 2139, the most significant AM processing challenge is maintaining a consistent level of Mg throughout the build. The Mg present in the alloy is critical for achieving the desired microstructure and properties through the early-stage formation of co-clusters. The vapour pressure of Mg can be four orders of magnitude greater than aluminium, resulting in a much higher vaporization rate of Mg from the molten pool during deposition. Additionally, as the thermal conditions change throughout the build, the vapour loss can vary within a given part as the underlying thermal conditions change and the molten pool gets larger and/or hotter. These process-induced variations in thermal conditions along with the very high vapour pressure of Mg create the possibility of a high degree of variability in Mg concentration within a given deposited component.

This project examined the Mg vaporization loss as a function of Mg concentration and the temperature of the substrate material. Nine experimental samples were analysed at three different Mg concentration levels and three different substrate temperatures. The microstructure was analysed using optical and electron microscopy, small-angle neutron scattering (SANS), differential scanning calorimetry (DSC), and microhardness. Comparisons were made between the nine experimental samples and a baseline cast sample that had the nominal 0.5 wt% concentration of Mg.

The Mg loss in the samples was calculated by measuring the Mg concentration before and after deposition using inductively coupled plasma mass spectrometry. The vaporization flux was then calculated based on measured dimensions of the deposited beads. This information was used to estimate the molten pool temperature using the Hertz–Knudsen equation and assuming regular solution thermodynamics. The vapour flux was related to Mg concentration in the deposited bead and the baseplate temperature during deposition.

11.2 Project Conclusions

The combined microstructural analysis showed that the character of the precipitate is dependent on the Mg concentration. For concentrations below 0.2 wt%, the microstructure was dominated by θ-type precipitates, while for concentrations above 0.2 wt%, the microstructure was dominated by Ω precipitates. In the solution treated and aged condition, the precipitates in the low-Mg deposits were identified as predominantly θ″ using DSC. These precipitates were characterized as disc-shaped using transmission electron microscopy (TEM) and were measured using SANS. The measured diameter was between 10 and 15 nm, while the thickness was 1–3 nm. The high-Mg samples also had disc-shaped precipitates, but they measured between 20 and 40 nm in diameter, depending on the Mg concentration, and were determined to be the Ω phase. The Ω precipitates were also 1–3 nm in thickness. For the same heat treatment, the Ω particles grow larger than the θ″ particles. For the samples deposited with the same composition at different baseplate temperatures, there was little difference in the measured microstructural features; however, comparison of the samples with different composition showed significant differences in the microstructural features. While the baseplate temperature has little effect on the precipitate character, the Mg concentration has a significant effect.

Microhardness measurements showed that there was little difference between the samples within the same composition series deposited at different temperatures. There were, however, large differences in microhardness (up to 13 VHN) in samples with varying amounts of Mg. An estimate of the ultimate tensile strength was calculated using a linear relationship between hardness and strength in wrought, solution treated and aged aluminium alloys. This calculation showed that the estimated strength difference between the low- and high-Mg deposits was about 40 MPa, a 10% deviation.

An experiment was conducted using aluminium alloy 5356 with high Mg content (5 wt%) deposited onto a baseplate with zero Mg (aluminium alloy 1100). The single-bead deposits were cross-sectioned and analysed for Mg content using electron microprobe analysis. The results showed that the Mg was fully mixed in the deposited bead and no compositional gradients were present. This provided conclusive evidence that the convective flow in the molten pool is high enough to not limit the ability of Mg to be transported to the surface for evaporation.

The mass flux rate of Mg from the molten pool was calculated using the measured Mg loss, the measured geometry of the deposited bead, and the deposition conditions. The total Mg loss was between 30 and 50%; however, the flux rate was much higher in the samples with higher Mg concentration. The highest Mg samples had 6 times more Mg mass flux than the lowest Mg samples. The flux rate was used to calculate and estimated molten pool temperature using the Hertz–Knudsen equation. For a constant heat input, the high-Mg content samples had an estimated temperature 200 K higher than the low-Mg samples.

The Mg mass flux from the molten pool is directly related to the estimated temperature within the molten pool. There was a factor of six difference between the low and high Mg flux rates in this experiment with the high flux rate at the high Mg concentration. There was a 200 K estimated difference in molten pool temperature between the low and high Mg samples, with the higher temperature at the higher Mg concentration. With the appropriate thermal sensors, this knowledge can be used to develop a feedback control strategy. Monitoring the molten pool temperature should provide a reasonably accurate prediction of the Mg flux from the molten pool. This information could be used to ensure that the Mg evaporative loss does not exceed a set value that would reduce the Mg concentration in the deposited material below the critical threshold amount of 0.2 wt%. Under this scenario, the consistency in the deposited material should be acceptable in terms of microstructure and properties.

12.0 ASSESSMENT, CONTRIBUTION, AND FUTURE WORK

12.1 Assessment

Overall, this project was successful in correlating vaporization loss in additively manufactured aluminium 2139 to microstructural changes. The relationship between Mg concentration and precipitate character was established and found to be similar to previous experimental work in this alloy published in the scientific literature. This study is the first to apply the mass flux/temperature relationship derived from the Hertz−Knudsen equation to predict molten pool temperature. While not experimentally validated, this relationship could provide a useful process control methodology for ensuring chemical homogeneity in deposited aluminium 2139.

As with any experimental study, there are changes that, in hindsight, could have improved the outcome. The chemistry of the alloy castings should have been checked prior to any further post-processing. The fact that two of the wire compositions were identical with very little Mg content meant that this study did not truly evaluate the minimum, mean, and maximum allowable Mg concentrations in alloy 2139. Since the baseplate castings did have the appropriate Mg levels, there was variation in the three combined compositions (wire plus baseplate); it was just lower in Mg content than anticipated. While not the intent of the experiment initially, this turned out to be somewhat beneficial, as it allowed more focus on the low end of the Mg concentration limit (around 0.2 wt%) where the transition from Ω to θ′ occurs in alloy 2139.

The inability to experimentally quantify the volume fraction of precipitates was an unfortunate outcome. Two methods were examined but ultimately proved unsuccessful. The TEM method was a limitation of the sample orientation and to a lesser degree the camera configuration in the TEM used in the study. The TEM method for quantification requires

reliable determination of the foil thickness. To image the precipitates edge-on, the sample must be tilted to a particular zone axis. To determine thickness of the foil, the sample must be tilted into a two-beam condition. These two tilt conditions means that the sample is in two different orientations, which could result in the thickness measurement occurring in a different location compared to the zone axis location where the precipitates where imaged. Aside from the orientation effects, the TEM itself proved to be a limiting factor, as it was unable to record two-beam images without risking damage to the camera itself.

It was hoped that the SANS experiment would also provide a means for measuring the volume fraction of precipitates. While such measurements have been documented in the scientific literature, it was not recognized in advance that the validity of the volume fraction measurement is dependent on the aspect ratio of the particles. In particular, high-aspect-ratio particles such as Ω and θ′ in this experiment are not amenable to volume fraction determination using small-angle scattering techniques.

12.2 Contribution

Ensuring consistency and repeatability in additively manufactured materials is critical to gaining wide acceptance of AM as a legitimate fabrication method for production hardware. This is particularly important for alloys like aluminium 2139 that are very sensitive to small compositional changes in highly volatile solute additions. Local variations in chemistry and microstructure can create uncertainty in the overall performance of AM structures. This project makes a significant contribution to the understanding of vaporization loss in AM alloys. It also provides a predictive tool for minimizing vaporization loss, which ensures chemical consistency throughout a deposited structure. The methodology for correlating compositional control with molten pool temperature will be applicable to a wide range of AM processes and alloys that have wide variations in constituent vapour pressures.

12.3 Future Work

This project correlated Mg flux to molten pool temperature using the Hertz–Knudsen equation. The molten pool temperatures that were calculated using experimentally determined flux values were reasonable when compared to prior studies in the scientific literature. The logical next step is to actually measure the molten pool temperature during the deposition process using an in-process, real-time infrared pyrometer. This experiment is not trivial, as it requires expensive hardware installed in a challenging environment (vacuum chamber in a deposition process with a high vapour load) and careful measurement to ensure that the average temperature is captured. Nonetheless, this experiment is possible and would be extremely valuable to verify that the predicted temperatures are correct.

Another aspect of this experiment that needs additional work is re-validation of the optimized heat treatment. This study used a heat treatment optimized in a previous experiment using similar material deposited in a similar process. However, the precipitate sizes measured using SANS and imaged using TEM where generally smaller in diameter than comparable material processed in other studies in the literature (albeit studies in which the material was not made via additive manufacturing). It would be worthwhile to re-investigate the heat treatment of this deposited alloy in a more rigorous manner to ensure that the true peak strength condition can be obtained. This would likely involve not just microhardness measurements (standard practice for heat treatment optimization) but also parallel correlation of precipitate diameter using SANS.

Finally, a further investigation into multi-layer effects would be valuable. Previous work documented variations in the Mg concentration as a function of vertical distance in a multi-layer deposit. This was attributed to the residual heat in previous layers, which limited the thermal conduction and caused the molten pool to either grow in size, increase in peak temperature, or both. Further experimentation using a pyrometer to measure the molten pool

would allow a control strategy that could possibly limit changes in chemistry over build layer vertical distance. Ultimately, this would provide comprehensive validation of the present study. If the molten pool temperature was monitored continuously, the power level could be reduced such that the molten pool temperature remains constant, which should provide a consistent level of Mg over all the build layers in a given part.